LUMEN SEGMENTATION IN INTRAVASCULAR ULTRASOUND DATA

A Dissertation

Presented to

the Faculty of the Department of Computer Science

University of Houston

In Partial Fulfillment

of the Requirements for the Degree

Doctor of Philosophy

By

Eduardo Gerardo Mendizabal Ruiz

December 2012

LUMEN SEGMENTATION IN

INTRAVASCULAR ULTRASOUND DATA

Eduardo Gerardo Mendizabal Ruiz

APPROVED:

Dr. Ioannis A. Kakadiaris, Chairman
Department of Computer Science

Dr. Shishir Shah
Department of Computer Science

Dr. Ricardo Vilalta
Department of Computer Science

Dr. Emanuel I. Papadakis
Department of Mathematics

Dr. George Biros
Institute for Computational Engineering and Sciences
University of Texas at Austin

Dr. Mark A. Smith
Dean, College of Natural Sciences and Mathematics

Acknowledgements

Foremost, I would like to express my sincere gratitude to my advisor Prof. Ioannis A. Kakadiaris for the continuous support of my Ph.D. study and research, for his patience, motivation, enthusiasm, and immense knowledge. His guidance helped me during this research and the writing of this thesis.

Besides my advisor, I would like to thank the rest of my thesis committee: Prof. George Biros, Prof. Manos Papadakis, Prof. Shishir Shah, and Prof. Ricardo Vilalta, for their encouragement, insightful comments, and valuable advise during all this years.

I want to thank the NSF for the grant that supported part of this research and to CONACYT for the scholarship I received to complete my studies.

Last but not the least, I would like to thank my parents Patricia Ruiz and Eduardo Mendizabal for being with me and supporting me with love and patience during all my life.

LUMEN SEGMENTATION IN INTRAVASCULAR ULTRASOUND DATA

An Abstract of a Dissertation

Presented to

the Faculty of the Department of Computer Science

University of Houston

In Partial Fulfillment

of the Requirements for the Degree

Doctor of Philosophy

By

Eduardo Gerardo Mendizabal Ruiz

December 2012

Abstract

Intravascular ultrasound (IVUS) is a catheter-based medical imaging technique that is capable of producing high resolution cross-sectional images of interior of blood vessels and it is currently the gold standard technique for the study of the characteristics of the atherosclerotic plaques. Segmentation of IVUS images refers to the delineation of the lumen/intima and media/adventitia interfaces of the vessel. This process is necessary for assessing morphological characteristics of the vessel such as lumen diameter, minimum lumen cross-section area, and total atheroma volume. This information is crucial for making decisions such as whether a stent is needed to restore blood flow in an artery and to determine the characteristics of the stent. Other applications of IVUS include the study of mechanical properties of the vessel wall, characteristics of the plaque, and 3D reconstruction of the vessel. Segmentation of IVUS images may be performed manually by an observer. However, depending on the type of analysis, the number of frames to be segmented can range from a few frames to hundreds of frames.

In this dissertation, we present a unified computational method for the semi-automatic segmentation of the luminal/wall interface in IVUS data. The method can be used with either B-mode or RF-data and it is based on the deformation of a curve by optimizing a probabilistic cost function. The main contribution is the development of a physics-based inverse method for the segmentation of the lumen employing the IVUS RF data as compared with previous method which employs the B-mode reconstruction. Experimental results demonstrate the robustness and accuracy of the method. These results pave the way for the automation of the analysis of contrast-enhanced IVUS images to assess extra-luminal perfusion.

Contents

Chapter 1

Introduction

1.1 Motivation

Cardiovascular disease (CVD) refers to those disorders that affect the heart and/or the vascular system. The most common form of CVD is atherosclerosis, a condition characterized by the formation and accumulation of plaque in the walls of the arteries which results on the narrowing and hardening of the arteries [38, 63]. Cardiovascular disease (CVD) refers to those disorders that affect the heart and/or the vascular system. According to the American Heart Association, CVD accounted for 32.8% (811,940) of all 2, 471,984 deaths in the United States in 2008, or one of every three deaths in the United States [61]. The most common form of CVD is atherosclerosis, a condition in which the arterial wall hardens and thickens due to the build up and accumulation of plaque [38]. Coronary artery disease (CAD) is usually caused by atherosclerosis in the arteries that supply blood to the heart (i.e., coronary arteries). The inflammation and disruption of coronary atherosclerotic

plaques (i.e., thrombotic-related complications) is the primary cause of acute coronary events such as heart attacks.

Modern medical imaging techniques have the potential of providing structural and functional imaging of the human body through a number of invasive, and non-invasive methods. In particular, contrast angiography is the standard technique for detecting and evaluating coronary artery disease. However, the two-dimensional nature of the images, the absence of information about the blood vessel wall, the insensitivity to substantial plaque burden in outwardly remodeled vessels and the inability to detect vessel wall disruption during angioplasty are important limitations that reduce the chance of obtaining crucial information necessary for an accurate diagnosis and effective treatment of CVD.

To overcome these limitations, intravascular ultrasound (IVUS) was developed towards the end of the 1980's and has rapidly become the gold-standard technique for assessing the morphology of blood vessels and atherosclerotic plaques *in vivo* [64] (Fig. 2.3).

Intravascular ultrasound (IVUS) is an invasive catheter-based medical image technique that is capable of providing high resolution cross-sectional images of the interior of blood vessels in-vivo. Segmentation of IVUS images refers to the delineation of the lumen/intima and media/adventita borders (Fig. 1.2). This process is necessary for assessing morphological characteristics of the vessel and plaque such as lumen diameter, minimum lumen cross-section area, and total atheroma volume. This information is crucial for making decisions such as whether a stent is needed to restore blood flow in an artery and to determine the characteristics of the stent. Other applications of IVUS includes the study of mechanical properties of the vessel wall and th characteristics of the plaque.

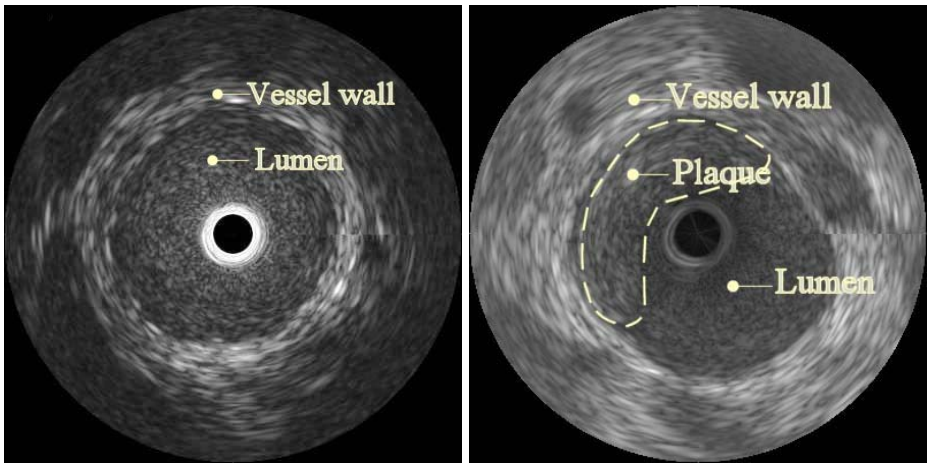

(a) (b)

Figure 1.1: Examples of a typical IVUS B-mode image of (a) normal and (b) atherosclerotic vessel.

In practice, manual segmentation of IVUS images may be performed by an expert observer. However, depending on the type of analysis, the number of frames to be segmented can range from a few frames to hundreds or even thousands of frames. Therefore, the manual segmentation of those images may be excessively time-consuming. Moreover, the manual segmentation may suffer from inter- and intra-observer variability due to its high level of subjectivity. Studies have shown that there may exist large differences (up to 20%) in the cross-sectional area of luminal segmentations provided by the same observer ([39]). Thus, a robust automatic segmentation method for IVUS images is needed to overcome these limitations.

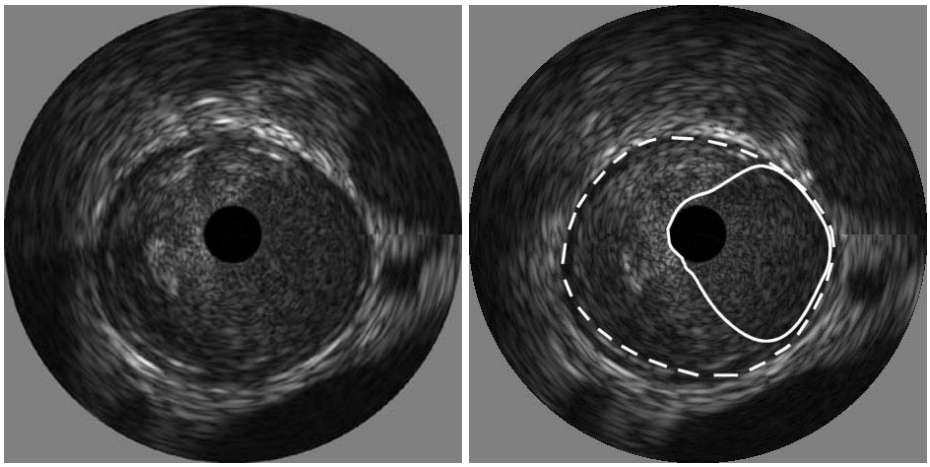

(a) (b)

Figure 1.2: Example of (a) an typical IVUS image with (b) its corresponding segmentation (the lumen/intima and the media/adventitia interfaces are depicted using a solid and dotted lines, respectively).

1.2 Previous work

Automated segmentation of IVUS sequences has been a topic of interest since the early 1990's. Early IVUS systems operated at frequencies in the range of 10 *MHz* to 20 *MHz*. At these frequencies, the blood presents a low acoustic impedance and speckle noise and therefore these systems produce IVUS images on which the lumen has low intensity, no texture, and a high contrast with respect to the vessel wall tissues. For this reason, many approaches for IVUS segmentation were based on the use of local properties of the image (e.g., pixel intensity and gradient information) combined with computational methods including graph search [67, 75, 78], active surfaces [30], active contours [32, 41], and neural networks [57]. Modern IVUS systems operate in higher frequencies (i.e., 30 to 40 *MHz*) and produce images with better resolution. However, the lumen on this images depicts more texture due to speckle, and lower contrast of the lumen with respect to the vessel

wall tissues. For these images, edge information may not be sufficient and therefore, segmentation approaches incorporated prior knowledge using region and global information such as texture [45], gray level variances [20, 37], statistical properties of the image [3], temporal information (3D segmentation) [6], and by mathematical morphology techniques [13].

Current approaches for the segmentation of IVUS images includes the shape-driven method for lumen and media-adventitia segmentation introduced by Unal *et al.* [71]. In this work, the lumen and media-adventitia contours were constrained to a smooth, closed geometry. Then, a shape space was built using training data and principal component analysis (PCA). Finally, segmentation was performed on this shape space by the minimization of an energy function using nonparametric probability densities with global measurements. Taki *et al.* [68] proposed a method for the delineation of the vessel borders. This method consisted of a preprocessing step for speckle removal followed by the deformation of parametric and geometric models using edge information. Downe *et al.* [14] introduced a method where active contour models were used to provide the segmentation using a 3D graph search method. Multilevel discrete wavelet frames decomposition was used by Papadogiorgaki *et al.* [56] to generate texture information that was used along with the intensity information for contour initialization. Then a post-processing is applied to refine the detected contour. Similarly, Katouzian *et al.* [25] presented a method where texture information was extracted using a discrete wavelet packet transform. Then, pixels were classified as lumen or non-lumen using k-means clustering. Finally, the contour was parameterized using a spline curve. Ciompi *et al.* [9] presented a method in which segmentation was

tackled as a classification problem and solved using an error correcting output code technique. In that work, contextual information was exploited by means of conditional random fields computed from training data. Wennogle *et. al* [76] proposed improvements over the method presented in [6] which include a preprocessing step to remove motion artifacts, a new directional gradient velocity term, and a post-processing level-set method. Cardinal *et al.* [7] presented a multiple interface 3D fast-marching method that was based on a combination of gray level probability density functions and the intensity gradient. The segmentation method included an interactive initialization procedure of the external vessel wall border. Zhua *et al.* [79] proposed a snake-based method for segmentation of IVUS images on which linear-filtered gradient vector flow which drives the deformation of a balloon snake. Moraes *et al.* [46] presented a method that relies on a binary morphological object reconstruction to segment the coronary wall in IVUS images. Balocco *et al.* ([1]) proposed a method based on the stabilization of the IVUS sequence and the subsequent registration of contiguous frames to generate an image with high contrast between the steady tissues from the blood. Finally segmentation was achieved by the classification of the pixels in the IVUS image using the growcut method. Katouzian *et al.* ([24]) presented a 3D method which employ frequency-based harmonic information extracted by brushlet expansion. Then, the blood and non-blood regions of the IVUS image are detected by clustering of the resulting brushlet coefficients. Finally, the detection of the lumen border is performed using a surface function active framework.

A common characteristic of these methods is that the segmentation is performed using the reconstructed B-mode reconstruction images either in polar, Cartesian or L-mode representations (Table 1.2). This poses a limitation considering that, apart from the frequency of

operation of the transducer, the gray level distributions of the different regions of the vessel in the B-mode images depends on the reconstruction settings of the IVUS systems such as TGC, dynamic range compression and rejection, persistence, and gamma curves which are subjectively selected by the interventionist [21, 43] (Fig. 1.3) and may change from one intervention to the next [42]. Thus, a segmentation method designed using B-mode images generated using a specific set of parameters may not work or may require parameter tuning or re-computation of gray-level intensity statistics in order to work appropriately on sequences containing IVUS images that are have different gray level distributions to those images used for the computation of the original gray-level intensity statistics.

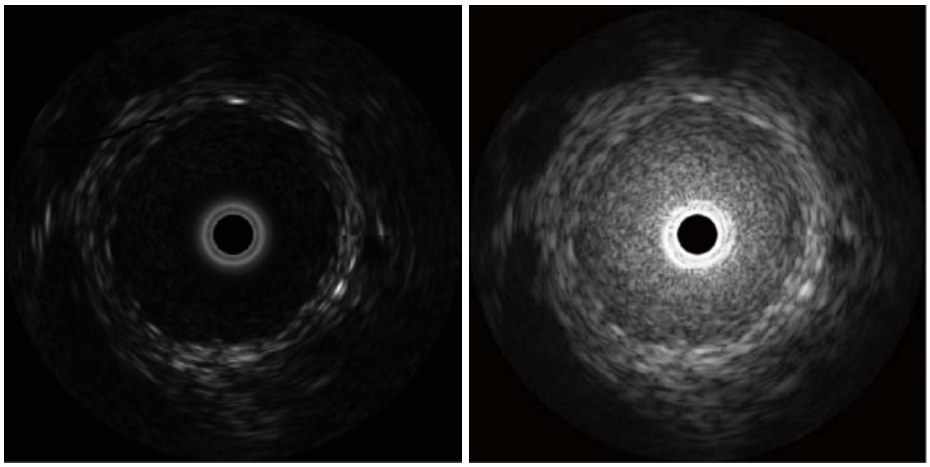

(a) (b)

Figure 1.3: Example depicting a 40 *MHz* IVUS frame in Cartesian B-mode representation using logarithmic dynamic range compression, (b) the same frame using linear dynamic range compression with a compression factor of 0.4.

Table 1.1: Overview of the main characteristics of some of the existing IVUS segmentation methods. EI stands for edge information and GS stands for gray level pixel intensities image statistics.

		IVUS data employed			**Descriptors employed**		**Requirements**	
Method	**Year**	**Polar mode**	**Cartesian mode**	**L-mode (3D)**	**EI**	**GS**	**Initialization**	**Prior comp of models**
Sonka *et al.* [67]	1995		X		X		X	
vonBirgelen *et al.* [75]	1996			X	X		X	
Zhang *et al.*[78]	1998		X				X	
Klingensmith *et al.*[30]	2000			X	X		X	
Kovalski *et al.*[32]	2000	X		X				
Mendizabal-Ruiz *et al.*[41]	2008	X				X	X	
Plissiti *et al.*[57]	2004		X		X		X	
Mojsilovic *et al.*[45]	1997		X			X		
Haas *et al.*[20]	2000	X				X		X
Luo *et al.*[37]	2003	X			X	X	X	
Brusseau *et al.*[3]	2004	X						X
Cardinal *et al.*[6]	2006			X		X	X	X
dos Santos *et al.*[13]	2006		X			X		
Unal *et al.*[71]	2008	X				X	X	X
Taki *et al.*[68]	2008	X			X			
Downe *et al.*[14]	2008			X		X	X	X
Papadogiorgaki *et al.*[56]	2008	X				X		
Katouzian *et al.*[25]	2008	X				X		
Ciompi *et al.*[9]	2009			X		X		X
Wennogle *et al.*[76]	2009			X	X		X	
Cardinal *et al.*[7]	2010			X	X	X		
Zhua *et al.*[79]	2011		X		X			
Moraes *et al.*[46]	2011	X				X		
Balocco *et al.*[1]	2011			X		X		X
Katouzian *et al.*[24]	2012			X		X		

1.3 Objectives

The goal of this research is to develop a computational method for the segmentation of the lumen/wall interface which performance is comparable with the performance of an expert observer and that is robust with respect to the variability in the gray-level distribution due to different IVUS systems and the subjectively adjusted B-mode reconstruction settings.

The objective of this dissertation is to development of a probabilistic method for the segmentation of the lumen/wall interface that is capable of working with either the B-mode reconstruction images and the raw radio frequency (RF) signal data with minimal user intervention.

1.4 Contributions

This dissertation presents a probabilistic segmentation framework for the identification of the lumen/wall interface consisting of two approaches: (i) segmentation of the lumen based on the analysis of the B-mode gray level images employing texture descriptors (IB method), and (ii) segmentation based on the analysis of the IVUS RF signal data employing a physics-based model of the interaction of the ultrasound signal with the structures of the vessel (RFB method).

IB method incorporates texture information by using the prediction of an machine learning classifier model. This step enable the segmentation of IVUS images from different frequencies (i.e., 20 and 40 MHz) without the need of adjusting any parameter, and it makes the proposed method robust to the problem of variability on the gray level distribution of

the IVUS images due the B-mode image-generation parameters.

The RFB method is robust with respect to the problem of variability on the gray level distribution of the IVUS images since the RF data are not affected by any of the B-mode transformation parameters. Moreover, this method presents a new paradigm for the IVUS segmentation problem on which the physics of the ultrasound transducer and the interaction of the ultrasound beam with the structures of the vessel are considered, as opposed to the traditional image-analysis based approach.

1.5 Document outline

Chapter 1 introduces this dissertation. Chapter 2 provides background to this work. Chapter 3 presents the proposed work, and the implementation details of these algorithms. The results of this work are presented and discussed in Chapter 4. Finally, we conclude this dissertation in Chapter 5.

Chapter 2

Background

2.1 Cardiovascular system

The cardiovascular system is in charge of transporting nutrients, hormones, metabolic wastes, and gases (oxygen, carbon dioxide) to and from the cells of the body. The cardiovascular system is composed by the blood which consist of liquid plasma and cells, the blood vessels which are the channels which carry the blood to and from all the tissues, and the heart which is a muscular pump to move the blood through the vessels. As any other organ or tissue in the body, the heart requires the supply of nutrients from the blood to survive. The vessels that deliver blood rich in oxygen to the heart are know as coronary arteries. The aorta, which is the main blood supplier to the body, branches off into two main coronary arteries: right and left coronary arteries. The right coronary artery (RCA) supplies blood mainly to the right side of the heart, while the left coronary (LCA), which branches into left anterior descending artery (LAD) and circumflex artery (LCX) supplies

blood to the left side of the heart.

2.1.1 Anatomy of blood vessels

The blood vessels are the part of the circulatory system in charge of transporting blood throughout the body. In the mammals, there are exist major types of blood vessels: (i) the arteries which carry the blood rich in oxygen and nutrients away from the heart, (ii) the capillaries which enable the exchange of water and chemicals between the blood and the tissues, and (iii) the veins which carry blood from the capillaries back toward the heart. Arteries can be divided into two main regions: lumen (i.e., the region where the blood flows) and wall. The wall of a blood vessel consist of three layers.

1. The tunica intima is the thinnest layer and consist of in its majority of endothelial cells (i.e., endothelium) that act as a semipermeable barrier between the wall interior and the lumen. The remainder of the intima consists of a small layer of subendothelial connective tissue interlaced with a number of circularly arranged elastic bands called the internal elastic lamina.

2. The tunica media, which is the thickest layer and consist primarily smooth muscle cells , and elastic tissue in large arteries. Its homogeneous nature implies that, internally, it is fairly echo free (i.e. dark) under ultrasound. Hence, if the media is of sufficient scale to be resolved, it will appear as a dark band near the luminal border.

3. The tunica adventitia is the outermost and thickest layer in the vessels and consists of irregularly-arranged connective tissue (i.e., collagen) and elastin. Since the adventitia is the vessel's interface to the surrounding structures, it is common to observe

various features adjacent to it such as nerves that supply the vessel as well as nutrient capillaries (i.e,., smaller vessels) apparently embedded within it. Therefore, the adventitia could be considered not as a vessel layer in itself, but as a region of connective tissue which merges the vessel into surrounding structures. The adventitia often has no well-defined outer boundary.

2.2 Atherosclerosis and vulnerable plaque

Atherosclerotic processes mainly involve the thickening of the intima, and other process such as fibrosis, necrosis, calcification, and hemorrhage [19]. The process of atherosclerotic plaque formation is considered to be an inflammatory, response-to-injury phenomenon that it is initiated by injury to the endothelium or smooth muscle cells of the artery wall [63]. Although atherosclerosis is a multi focal disease, it is well known that atherosclerotic plaques are not similar to one another in composition, progression rate, stability, and thrombogenicity.

In the past, it was believed that the increase of plaque and the consequent narrowing of the coronary arteries was the cause of fatal coronary events. Currently, it is known that the inflammation and disruption of coronary plaques with superimposed thrombosis is the primary cause of acute coronary events. It has been shown that for up to 75% of the acute ischemic coronary syndromes, atherosclerotic plaque rupture is the underlying pathological mechanism [5, 10]. Pathology studies indicate that certain plaques are more prone to develop acute coronary events than others. In this context, the field of cardiology has introduced the term “vulnerable plaque” (VP) which refers to those plaques with a high

likelihood of rupture, thrombotic complications, and the consequent rapid progression to stenosis [44, 49, 50, 48].

Although there is no broad consensus on what characteristics define a VP, autopsy studies have provided useful indicators of the features exhibited by certain plaques immediately before rupture. The histopathologic characteristics of ruptured plaques have been well defined [73]. The most consistent findings include: (i) a large lipid (necrotic) core composed of free cholesterol crystals, (ii) cholesterol esters and oxidized lipids impregnated with tissue factor, (iii) a thin fibrous cap depleted of smooth muscle cells and collagen, (iv) an outward (positive) remodeling, (v) inflammatory cell infiltration of the fibrous cap and adventitia (mostly monocyte/macrophages, some activated T cells and mast cells), (vi) intra-plaque hemorrhage, and (vii) the formation of new microvessels (neoangiogenesis or neovascularization) at the arterial wall adventitia, and within the atherosclerotic plaque (i.e., vasa vasorum) [74].

2.3 Medical ultrasound

Ultrasound refers to the use of sound with frequencies higher than the upper limit of human audible range (i.e., above 20 kHz). Ultrasound has widely been used as a diagnostic tool in medicine for the visualizing muscles, tendons, and internal organs. The applications of ultrasound in medicine include (but are not limited to) the visualization and study of morphological and structural information of heart and blood vessels, liver, spleen, pancreas, kidneys, bladder, uterus, unborn child in pregnant patients, etc.

Medical ultrasound is based on the transmission of sound waves to the interior of the body,

and the reception of the acoustic echoes generated by the structures contained on it (Fig. 2.1).

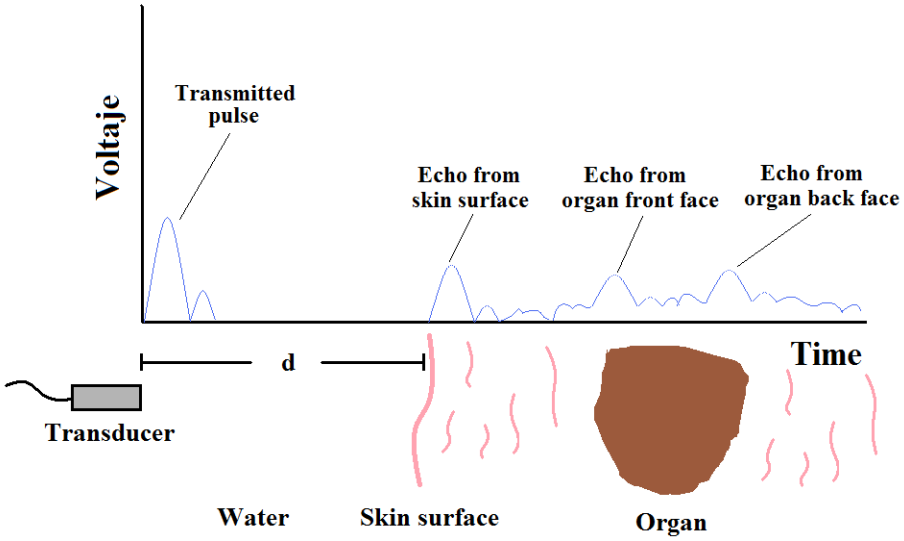

Figure 2.1: Depiction of medical ultrasound principle.

The sound waves are produced by the electric excitation of a piezoelectric (i.e., pressure-electric) material which expands and contracts producing pressure waves (i.e., ultrasound transducer). As the waves travel inside the body, they interacts with the different organs and tissues which reflects and scatter part of the waves. The intensity of the reflected waves depend on the characteristics of the tissue such as compressibility and density which defines its acoustic impedance. According on its acoustic impedance, homogeneous objects are said to be echo-free, hypoechoic, or echolucent. Acoustically heterogeneous objects are said to be echogenic or hyperechoic and generate stronger acoustic reflections.

The reflected waves are detected by the piezoelectric material which contracts and expands producing an electrical signal. The signals are then processed to generate an gray scale

image that represents the intensity of the reflections with respect to the distance from the piezoelectric to the tissues that generated the reflections. The distribution of the gray intensity values of the reflected signal is often referred to as dynamic range. As the wave propagates trough the body, some of its energy is lost due to reflection absorption. This attenuation may be compensated by the amplification of the returned signal according to a monotonically increasing function which is essentially the inverse of the expected attenuation (i.e., time-gain compensation (TGC)). Applying TGC the received signals increases signal to noise ratio (SNR) of the signal as attenuation increases. However, the use of this techniques allows a better visualization of the structures farther from the transducer. Other techniques for improving the visualization of the ultrasound data include: (i) compression and rejection of the dynamic range in order to allow the visualization of structures with certain acoustic characteristics, (ii) time averaging of the signals to improve the SNR, and (iii) adjustment of gamma curves which control the relationship between the actual and the displayed gray scale. However, it is important to note that there are no standard values for this parameters and therefore they must be adjusted by the operator according his judgment.

2.4 Intravascular ultrasound

The IVUS imaging intervention consists of steering a guidewire with a small diameter (about 0.84 *mm*) into the blood vessel branch to be imaged. The IVUS catheter is then percutaneously slid-in over the guidewire and positioned within a target segment of interest. For coronary imaging in humans, the entry point is typically located at the femoral artery.

The IVUS system acquires and displays the acquired images usually at 30 *frames/second*. For some procedures, the ultrasound catheter may be pulled back in order to identify and analyze the different vessel regions. The pullback can be performed either manually or by using a motorized device which moves the transducer at a constant determined speed (usually 0.5 *mm/s*). In human coronary arteries, the target segments generally include at least 10 *mm* of the distal vessel, the lesion site(s), and the entire proximal vessel back to the aorta [42]. If additional information about a lesion is needed, an acquisition may be performed by maintaining the IVUS catheter stationary over the region of interest. The analysis of the acquired data may be performed in real-time during the intervention or off-line after the acquisition.

The IVUS system consists of a catheter with miniaturized ultrasound transducer which transmits ultrasound pulses and receives an acoustic radio frequency (RF) echo signal (i.e., A-line, Fig. 2.2(a)) at a discrete set of angles (commonly 240 to 360). These signals are then processed to reconstruct an image that is meaningful to the physicians (i.e., B-mode image). The B-mode reconstruction process consists of the detection of the positive envelopes of each A-line, application of a TGC, stacking of the signals along the angular direction, quantization of the signal, compression of the dynamic range, and 8-bit gray scale mapping. The result of this process is an image known as B-Mode polar representation (Fig. 2.2(b)). For easier visualization the image is converted from polar to Cartesian coordinates in order to obtain a disk-shaped image that resembles the interior of the vessel (Fig. 2.2(c)).

There exist two types of IVUS transducers: the mechanically-rotated transducer and the electronically switched multi-element array system. The first type consist of a single

piezoelectric element which is driven by a flexible wire that rotates about 1,800 *rpm* to sweep a beam almost perpendicular to the catheter. The sensor/wire bundle resides in a sheath in which the sensor may be moved back and forth. The electronically switched multi-element array system consist of an annular array of small piezoelectric elements rather than a single rotating element. When using this type of transducer, the ultrasound beam can be manipulated to focus optimally at a broad range of depths.

2.4.1 IVUS image properties

2.4.1.1 Image resolution

The ability of the IVUS technique to provide details of the structures being imaged depends on the spatial resolution and the contrast resolution of the employed system. Spatial resolution refers to the ability of the system to discriminate small objects within the generated image and has three principal directions. The axial resolution (i.e., parallel to the beam) depends on the frequency and duration of the impulse wave employed, the size of the transducer, and the radial sampling rate. The lateral resolution (i.e., perpendicular to the beam and the catheter) depends on the wavelength of the signal, the size of the transducer employed. The out-of-plane direction (i.e., perpendicular the axial and lateral resolution) primarily decides the slice thickness of the IVUS image and depends on the beam width. Lateral resolution degrades linearly with distance from the catheter, while axial resolution remains constant. Out-of-plane resolution improves as the distance of the beam from the catheter increases. Spatial resolution increases with transducer frequency,

however, attenuation also increases with frequency. Due to the rotational tomographic nature of IVUS images, their spatial resolution is highly variable within a single image. For a 20 to 40 MHz IVUS transducer, the typical resolution is considered to be 80 μm axially and 200 to 250 μm laterally [43]. However, there is some variation in the reported values regarding the spatial resolution. For example, Elliott *et al.* [16] reported for a 20 MHz transducer an axial resolution of 0.19 mm, lateral resolutions of 0.5 mm and 0.83 mm at 1 mm and 5 mm from the transducer, respectively. Nissen *et al.* [53] reported an axial resolution of 0.15 mm and lateral resolution of 0.25 mm at typical coronary diameters for a 30 MHz transducer. Finally, Lin *et al.* [36] reported an axial resolution of 0.150 mm is reported for a 40 MHz transducer.

Contrast resolution referees to the dynamic range of the generated images. An image with low dynamic range depicts as black and white regions with a few intermediate gray-level values (i.e., granular), while images at high dynamic range are often softer. Contrast resolution depends directly on the B-mode reconstruction parameters selected by the interventionist.

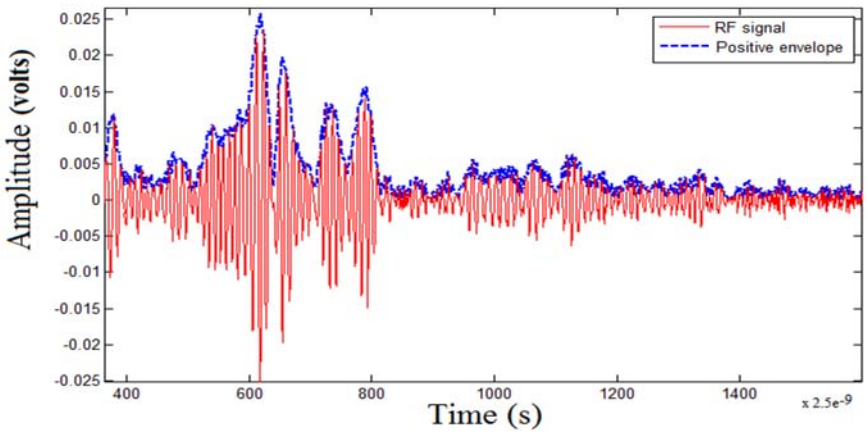

(a)

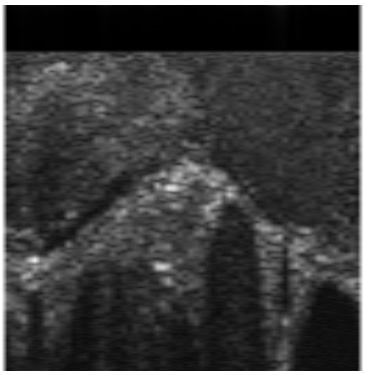

(b)

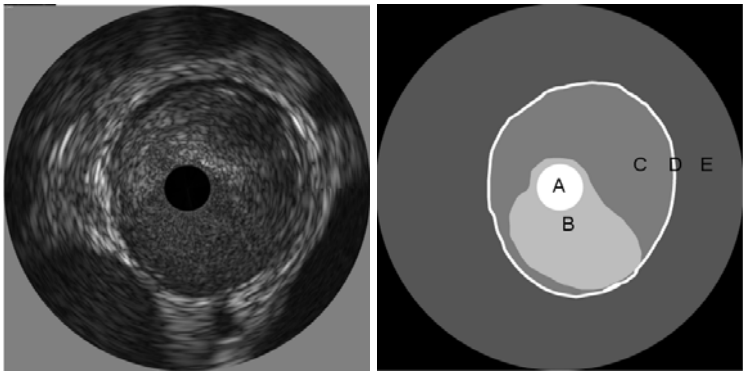

(c) (d)

Figure 2.2: Depiction of (a) an A-line signal and its envelope, and the B-Mode IVUS representations; (b) IVUS image in polar representation; (c) IVUS image in Cartesian representation, and (d) Depiction of the regions in this image: **(A)** the area occupied by the IVUS catheter; **(B)** The lumen; **(C)** the intima; **(D)** the media; **(E)** the adventitia and surrounding tissues.

2.4.1.2 IVUS artifacts

A series of non-desired artifact may be presented in the IVUS images limitation the ability of its analysis. The most common types of artifacts are listed next:

- **Speckle noise.** This term refers to random point-like artifacts visible in the lumen and to the more organized interference patterns apparent even in relatively homogeneous tissues. The intensity of the blood speckle increases exponentially as transducer frequency increase and as blood flow velocity decreases. This phenomenon can limit the ability to differentiate lumen from tissue (especially soft plaque, neointima, and thrombus). This problem is exacerbated by flow stagnation or rouleaux formation, often most evident when the catheter is across a tight stenosis or within certain dissections (e.g., intramural hematomas) [43].

- **Non-uniform rotational distortion (NURD).** This artifact is related exclusively to mechanical catheter systems. NURD artifacts are the result of mechanical binding of the drive cable that rotates the transducer. In an extreme situation, fracture of the drive cable can occur.

- **Motion artifacts.** Motion artifact are the result of nonstable catheter position due to cardiac and respiratory motions. Occasionally, the vessel moves before a complete circumferential image can be created. This results in cyclic deformation of the IVUS image.

- **Ringdown artifacts.** After the piezoelectric transducer is excited to generate the initial ultrasound wavelet, it takes some time for it to cease vibrating. This causes the appearance of bright concentric halos of variable thickness surrounding the catheter

that obscure the area immediately adjacent to the catheter. Since this artifact does not present large variations in its location, it is usually replaced by a constant intensity value in the image. However, this may create a lower limit on the distance a tissue must be from the catheter for it to be imageable.

- **Guidewire artifact.** This artifact is produced by the reverberation of the guidewire and is depicted in the IVUS images as a series of partial rings followed by more distant shadowing behind the wire.

- **Shadows.** Shadow artifacts are depicted as dark regions in the IVUS image for which no information is available. Shadow artifacts are typically produced by calcification in the wall of the vessel or by the presence of stents.

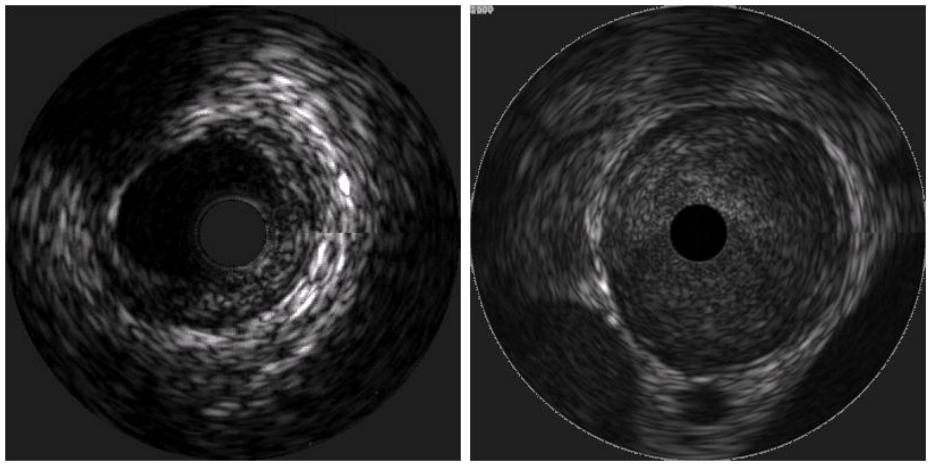

(a) (b)

Figure 2.3: Examples of typical (a) 20 MHz and (b) 40 MHz IVUS images.

Chapter 3

Methods

This chapter presents a developed probabilistic method for the segmentation of the lumen/wall interface in IVUS data, that is robust with respect to the variability in the gray-level distribution due to different IVUS systems and B-mode reconstruction settings. The proposed method consist of the deformation of a curve that represent the lumen/wall interface that is parameterized using Fourier series in the polar space. The segmentation of the lumen/wall interface is achieved by the minimization of a probabilistic cost function that deforms the parametric curve which define a probability field that is regularized with respect to the given likelihoods of the pixels to belong to blood and non-blood. The likelihoods of each pixel to belong to lumen and non-lumen are assigned using the posterior probability of a support vector machine (SVM) classifier trained using features extracted from user-provided samples from blood and non-blood regions corresponding to frames of the sequence to segment. The method for the extraction of these features is divided into two approaches depending the data employed. The first approach consist of the extraction

of texture features from the B-mode reconstruction images (i.e., B-mode-based approach) while the second approach (RF-based approach) consist of extracting texture features from a reconstruction computed from the RF signal based on a physics-based scattering model of the ultrasound signal (i.e., DBC reconstruction). The details of the probabilistic segmentation method and its formulation for both approaches are provided next.

3.1 Lumen parameterization

Similarly to the work of Unal *et al.* ([71]), we employ the B-mode polar IVUS image representation since this coordinate space makes the problem friendlier due to the 1D appearance of the lumen contour. In this representation, the horizontal axis corresponds to the angular position of the transducer, while the vertical axis corresponds to the radial penetration by the ultrasound beam. Therefore, the intensity value of a pixel $x = (r, \theta)$ can be defined as $I(x)$ where r and θ correspond to the radius and angle, respectively. We define the function F that represents the interface between the lumen and the vessel wall (Fig. 3.1). This curve F is parameterized by θ and $\mathbf{C}$ (i.e., $F(\theta, \mathbf{C})$).

Manual annotations from observers define the lumen contour as a smooth curve. Moreover, we know that a polar B-mode IVUS image is periodic with respect to the horizontal axis. Therefore, the smoothness and the periodicity of the contour are requirement for the parametric curve that defines the lumen/wall interface. In this work, we have chosen to parameterize this curve using Fourier series since it provides a periodic curve in which smoothness can be controlled by the number of coefficients N_k. The lumen contour is

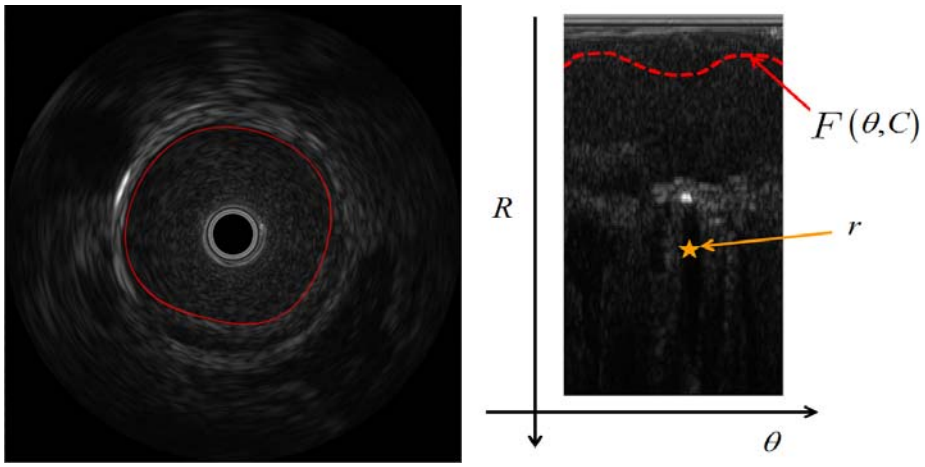

(a) (b)

Figure 3.1: Depiction of the lumen contour in (a) Cartesian representation and (b) the polar B-mode representation.

given by:

$$F(\theta, \mathbf{C}) = \frac{a_0}{2} + \sum_{k=1}^{N_k} \left[a_k \cos\left(\frac{k2\pi\theta}{N}\right) + b_k \sin\left(\frac{k2\pi\theta}{N}\right) \right] , \tag{3.1}$$

where N corresponds to the number of sampled angles (i.e., width of the polar image), and

$$\mathbf{C} = [a_0, a_1, ..., a_{N_k}, b_1, ..., b_{N_k}]^\intercal$$

are the Fourier coefficients that control the shape of the curve.

3.2 Probabilistic segmentation cost function

In our method, the lumen segmentation problem consists of finding the optimum parameters $\mathbf{C}^*$ such that the curve $F(\theta, \mathbf{C}^*)$ corresponds to the interface between the lumen and

the vessel wall. The formulation we introduce to solve this problem is inspired by the variational segmentation theory presented by Rivera *et al.* ([60]). This work pose the k classes segmentation problem as the computation of a probability field $P \in R^k$ with three main characteristics: (i) P should be similar to a given likelihood field $\hat{V} \in R^k$, (ii) P should be spatially smooth, and (iii) the entropy of P should be controllable. Then, P is computed by solving a problem of the form:

$$\min_{p} \quad U(P) = D(P, \hat{V}) + \mu_1 R_1(P) + \mu_2 R_2(P) \,, \tag{3.2}$$

where D is a term that promotes P to be similar to $\hat{V}$. The regularization term R_1 controls the entropy of P while the regularization term R_2 promotes P to be spatially smooth. The relative contribution of the regularization terms to the total cost function $U(P)$ is controlled by the parameters μ_1 and μ_2.

The segmentation of the lumen region corresponds to a binary segmentation task (i.e., $P \in R^2$) on which the two possible classes for each pixel are lumen ($k = l$) and non-lumen ($k = n$). By construction, in the IVUS polar B-mode representation, the class of each pixel can be determined by evaluating the sign of the distance from the pixel to the curve that defines the lumen/wall interface $d(x, \mathbf{C}) = F(\theta, \mathbf{C}) - r$. If $d(x) \geq 0$ the pixel is considered to belong to lumen, otherwise the pixel is considered to belong to non-lumen. We define a parametric probability field P for a polar B-mode image by using a sigmoid function which determine the probability of each pixel in the image to belong to the lumen $P_l(x, \mathbf{C})$ depending on its distance to the curve:

$$P_l(x, \mathbf{C}) = \frac{1}{1 + e^{-\lambda d(x, \mathbf{C})}} \,, \tag{3.3}$$

where λ is a parameter that controls the rate of the transition from 0 to 1 defined by the

sigmoid function (Fig 3.2).

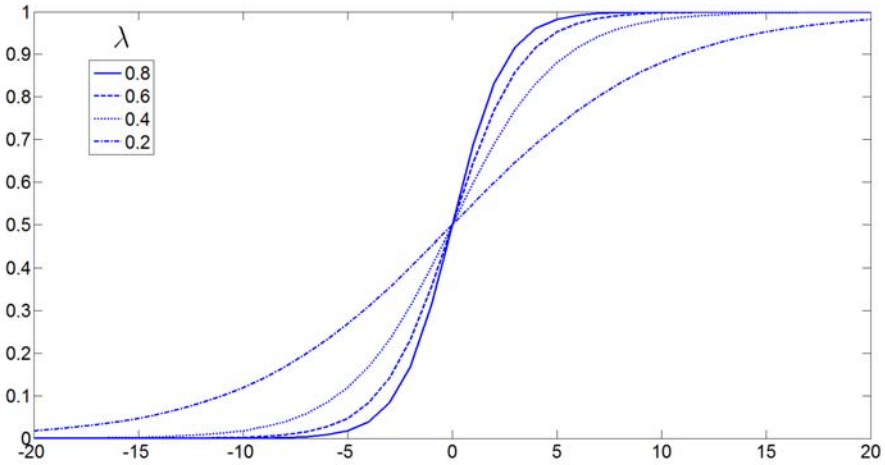

Figure 3.2: Examples of a sigmoid function with different values of λ.

Using this formulation, pixels far above the contour will have a higher probability of belonging to the lumen, while the pixels far below the contour will have probability close to zero. For the pixels near the contour, depending on the value of λ, the probability of belonging to lumen will be close to 0.5 (Fig. 3.3). The probability of a pixel to belong to non-lumen is given by: $(1 - P_l(x))$.

In our problem, the entropy is related to the sharpness of the transition between the two classes (from $P \approx 1$ to $P \approx 0$). This transition is controlled by the parameter of the sigmoid λ resulting in a similar effect that the entropy control term R_1 of Eq. (3.2).

Similarly, in our case the effect of the regularization term R_2 of Eq. (3.2) which promotes the spatial smoothness of P, is controlled by the number of Fourier coefficients N_k corresponding to the parametric curve $F(\theta, \mathbf{C})$.

In ([60]) several choices for the term D are discussed. In this work, we chose to use the

Kerridge's inaccuracy measure:

$$D(P,V) = -\sum_{k}\sum_{x} P_k(x)\log \hat{V}_k(x). \tag{3.4}$$

which is a generalization of the Shannons entropy used to measure the inaccuracy of the assertion of a probability estimation ([29]).

Let $\hat{v}_l(x)$ and $\hat{v}_n(x)$ be the likelihoods of the pixel $x = (r,\theta)$ to belong to the lumen and non-lumen, respectively. Then the lumen segmentation problem is posed as the minimization of the cost function:

$$U(\mathbf{C}) = -\sum_{x} P_l(x,\mathbf{C})[log(\hat{v}_l(x))] + [1 - P_l(x,\mathbf{C})][log(\hat{v}_n(x))]. \tag{3.5}$$

where $\hat{v}_l(x)$ and $\hat{v}_n(x)$ represent the given likelihoods of the pixel $x = (r,\theta)$ to belong to the lumen and non-lumen, respectively. The existence of a minimum of the cost function depends on the characteristics of the given likelihoods. The details regarding the computation of these likelihoods are provided in Sec. 3.3.

It is important to remark that the proposed cost function (3.5) is consistent with the spirit of the probabilistic framework proposed by Rivera *et al.*, since (i) the probabilistic segmentation P is attached by the Kerridge information measure to the likelihood measure field V, (ii) the smoothness of P is controlled by the number of coefficients that define the parametric boundary curve, and (iii) the slope of P at the class boundary (i.e., entropy) is controlled by the parameter λ of the sigmoid (Eq. (3.3)).

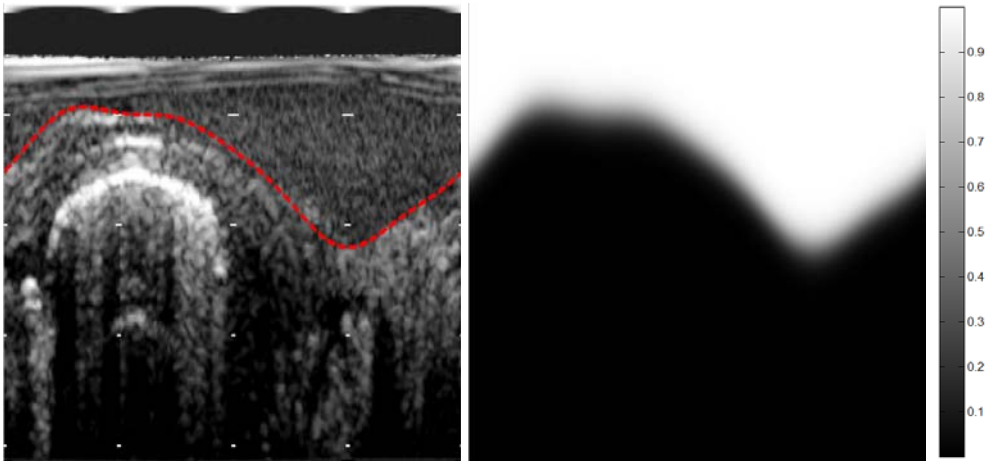

(a) (b)

Figure 3.3: (a) Example depicting the curve corresponding to the lumen/wall interface, and (b) the parametric probability field defined by the curve using $\lambda = 0.8$.

3.3 Computation of likelihoods

For the computation of the likelihoods of each pixel to belong to lumen or non-lumen classes, it is necessary to generate features that characterize each class. In this work, we propose two approaches for the characterization of each classes by the generation of features extracted from (i) the standard B-mode reconstruction: IB method and (ii) a reconstruction based on the analysis of the RF IVUS data: RFB method. While the extracted features can be used for estimating a probability density function by the use of histograms, Parsen windows or clustering techniques, in this work we propose to determine the likelihood of each pixel to belong to lumen or non-lumen classes by the use of the probability estimates of the prediction of a support vector machine (SVM) classifier. The reason for choosing SVM instead other techniques is that the SVM method achieve a good balance between variance and bias. Alternative methods with different learning strategies exist

(e.g., divide and conquer by decision trees, or probabilistic methods like Bayes classifiers) and they remain as potential candidates for future work.

3.3.1 Support vector machines classifier

SVM is a class of binary supervised learning methods that are commonly used for classification and regression. SVMs process the data by mapping all samples features into a high dimensional space defined by a kernel. In this high dimensional space, the data may be linearly separated by a single boundary defined by a hyperplane where support is given by selected samples in the data (support vectors). To increase the probability of a correct classification it is desirable to have the decision boundary at a maximum possible distance from the samples. The distance between the support vectors and the decision boundary is called the margin. The goal of SVM, is to find a separating hyperplane that would result in the largest margin. Once the optimal hyperplane function is computed, any new sample can be classified by mapping its features into the same space defined by the kernel and then evaluating in the discriminant function[1]. In this work, we chose to employ the radial basis function (RBF) kernel (i.e., $k(\mathbf{E}_i, \mathbf{E}_j) = \exp(-\gamma||\mathbf{E}_i - \mathbf{E}_j||^2)$,$\gamma > 0$, for a pair of feature vectors $\mathbf{E}_i$ and $\mathbf{E}_j$). One of the motivations to use the RBF kernel, is that it requires only two parameters to be tuned (c which corresponds to the penalty for errors in the classification, and γ corresponds to the width of the RBF kernel) as compared with other kernels (e.g., polynomial) ([22]). A common strategy for finding the values for these hyper parameters is by using cross-validation and grid-search ([22]). In addition to the class of a given sample, it is possible to compute the posterior probability estimate of the

[1]For more information regarding the theory of SVM we refer the reader to ([4]).

SVM prediction $P(k|\mathbf{E}_x)$ ([77]). In this work, we propose to use $P(k|\mathbf{E}_x)$ as the learned likelihoods for lumen and non-lumen $\hat{v}_l(x)$ and $\hat{v}_n(x)$, respectively.

3.3.2 Image-based approach

The intensity of the blood speckle increases exponentially with the increase of the frequency of the transducer ([42]). For example, in 20 *MHz* images the gray level distribution of the pixels in the lumen region appears relatively dark when compared to 40 *MHz* images which depict some texture due to the speckle. Therefore, in this work, we propose to incorporate texture information into the terms corresponding to the likelihoods of the pixels to belong to lumen and non-lumen.

3.3.2.1 Generation of features from the B-mode reconstruction

Laws' texture measures are a well known, widely used class of textural image descriptors and enjoy continued use today mostly due to their relatively simple implementation, and the fact that they mimic the behavior of more advanced methods ([34]). Laws' texture features are generated from an image by first convolving the image with a number of specialized kernels. These kernels are in the majority of cases 5×5 (level 5), though others were proposed which do not currently find widespread use. The level 5 kernels are produced by taking the outer product of all the combinations of the basis one-dimensional level 5 convolution kernels (Table 3.1) ([33]). The 2D kernels are assigned a string mnemonic $k_L k_E$ (e.g., Kernel L5E5 is generated by convolving vertical kernel L5 by horizontal kernel E5). A total of 25 images are formed by convolving the original 2D images with the

Table 3.1: One-dimensional convolution kernels for level 5.

Name	Kernel
Levels (L5)	[1 4 6 4 1]
Edges (E5)	[-1 -2 0 2 1]
Spots (S5)	[-1 0 2 0 -1]
Waves (W5)	[-1 2 0 -2 1]
Ripples (R5)	[1 -4 6 -4 1]

convolution kernels.

After convolving the polar B-mode image with these kernels, it is necessary to convert each of the resulting 25 images L_l into a measure of texture energy E_l. This is accomplished by a windowing operation in which the value of every pixel x is replaced by the absolute value of the sum of the pixel values in a 5×5 window W_x centered in the pixel x

$$E_l(x) = \sum_{y \in W_x} |L_l(y)|.$$

These texture energies are used to form a 25-dimensional feature vector $\mathbf{E}_x = [E_1, E_2, ..., E_{25}]$ that will characterize the class of each pixel x.

3.3.3 Generation of likelihoods based on texture analysis

In general, we can assume that the gray level distributions and texture of the lumen and non-lumen regions remain similar within the frames belonging to the same sequence. We part from this assumption to compute the likelihoods based on the use of a SVM classifier that is trained using texture features of a number of samples from the lumen and non-lumen regions given by the user in the first frame of the sequence to be segmented. However, although the assumption of similarity of gray level distributions within the frames of

the same sequence is valid most of the time, minor differences in the gray level distribution of the lumen region on the frames can be expected since the gray level distribution of speckle is also related to blood velocity, where low-velocity blood produces coarser, brighter speckle and higher velocities produce finer, lower-intensity speckle ([53]). Although it is not very common, it is possible that the interventionist perform changes in the B-mode reconstruction parameters during an acquisition which may result in large differences between the gray level distributions of frames within the same sequence. If any of these cases occur, it may be possible that the original SVM model that was generated using the samples from the first frame is not reliable for the computation the likelihoods for the pixels of the subsequent frames in the sequence. One option to overcome this limitation is to train the SVM using samples from all the frames in the sequence which depict significant changes in the gray level intensities of the regions of interest. However, it is the intention of this work to require the less user intervention as possible. Therefore, we propose to detect the possible changes on the gray level intensities during the sequence and then adjusting the SVM model to account for this possible changes. Then, the process of estimating the likelihoods can be divided into three phases: training, deployment, and model adjustment.

Training: In the training step, we require the user to select samples of lumen and non-lumen regions (R_l and R_n, respectively) from the first frame f_1 of the sequence to be segmented (Fig. 3.4). We compute the texture energies $L(x) \, \forall \, x \, \in \, \{R_l, R_n\}$ in the IVUS polar B-mode image using the Law's filters as described previously. A feature vector $\mathbf{E}_x \, \in \, R^{25}$ containing the computed texture energies for each pixel corresponding to R_l and R_n is associated to its corresponding class $k(x) \, = \, \{l, n\}$. A training set T_1 is then

generated using the feature vectors and the classes of each pixel. Next, a SVM model Π_1 is computed using the training set T_1 and the optimal c and γ.

Deployment: For each of the frames to be segmented, we compute a vector $\mathbf{E}_x$ for every pixel in the frame f_i and we obtain its class $k(x)$ using Π_1. The posterior probabilities of the classification result for each pixel are then used as the learned likelihoods $\hat{v}_l(x) = P(l|\mathbf{E}_x)$ and $\hat{v}_n(x) = P(n|\mathbf{E}_x)$.

Cartesian B-mode frames depict a dark circle in the middle of the image. This circles are generated by the IVUS system and corresponds to the IVUS catheter for which there is no available information. Ring-down artifacts are produced by acoustic oscillations in the transducer which are usually observed as bright halos of variable thickness surrounding the catheter creating a zone of uncertainty adjacent to the transducer surface ([42]). These artifacts are commonly present in the region corresponding to the lumen and may interfere with the computation of the likelihoods for the lumen. However, our observations in numerous IVUS sequences indicate that the width of this halo remains relatively constant within a sequence. Therefore, since the region occupied by the ring down artifact correspond to lumen we set the likelihoods of those pixels to belong to lumen to one. We require the user intervention to provide the radial location χ of the outer-most trace of the ringdown artifact in the first polar B-mode frame of the sequence to be segmented. Then, we set the likelihoods for the region corresponding to the catheter and the ring down artifact as $\hat{v}_l(x) = 1 \forall x | r \leq \chi$ and $\hat{v}_n(x) = 0 \forall x | r > \chi$. Figure 3.4 depicts examples of the likelihood computed for a frame as computed with the SVM model.

Model adjustment: Considering the speed of the IVUS images acquisition (30 *frames/s*) and the typical pullback speed using motorized device (0.5 *mm/s*), we can assume that the

distance between the cross sections of the vessel depicted by two consecutive frames is approximately 16 μm. Then, in general we assume the shape of the lumen contour of two consecutive frames i and $i+1$ is very similar and therefore the maximum distance between the lumen contour of these consecutive frames is constrained to w_b (an experiment for validating this assumption is presented in Section 4.1.1). We propose to use this information to assess the reliability of the SVM model trained with the samples acquired from the first frame of the sequence to detect the possible changes in the gray level intensities of the lumen and non-lumen regions by assessing its accuracy on the classification of the regions defined by the curve $F_i(r, \theta, \mathbf{C}_i)$ on the next consecutive frame f_{i+1} in the following way.

Consider the segmentation result F_i for a frame i. If we place the curve F_i on the next consecutive frame $i+1$, we can assume that most of the pixels above and below the curve will effectively belong to the corresponding classes with exception of those pixels that are closer to the curve. We define a distance w_b around this curve and we assume that the pixels with $d(x, \mathbf{C}_i) \geq w_b$ correspond to lumen while those pixels with $-w_n \leq d(x, \mathbf{C}_i) \leq -w_b$ correspond to non-lumen. We introduce w_n as a limit below the curve is because we are only interested in the non-lumen regions more proximal to the lumen in order to discard other outer regions such as adventitia or outer adventitia. This information is used to create a class mask (Fig. 3.5), and we use the classes of these pixels as ground truth for assessing the classification result of the texture features of frame $i+1$ for the pixels on the mask. If the accuracy A_1 of the classification is above a given threshold (i.e., $A_1 \geq \tau_1$), we assume that we can rely on the classification result and therefore we use the classes and probabilities of the prediction given by Π_1 as the likelihoods for the segmentation of this frame. However, if the $A_1 < \tau_1$ this may be an indication of a change on the gray level

distributions of the regions of interest or a large change on the shape of the lumen contours from frame i to frame $i+1$. Then, we perform the following steps: first we assume that the reason for the low accuracy obtained is due to a change in the gray level distribution. Then, we build a new training set T_2 consisting of randomly selected samples from the original training set T_1 and from the blood and non blood regions on the frame $i+1$ defined by the class mask. Then, we train a new SVM model Π_2 in using T_2. The accuracy A_2 of Π_2 is evaluated by classifying all the pixels within the class mask. If A_2 improves with respect to A_1 (i.e., $A_2 \geq A_1$), we consider that the new model is more reliable and therefore it is used to estimate the likelihoods of the subsequent frames. However, if $A_2 < A_1$, we assume that the low accuracy is the result of a large change on the shape of the lumen occurred and therefore the previous SVM model Π_1 is maintained to compute the likelihoods of the pixels of that frame and the subsequent frames. This process is repeated for each frame in the sequence leading to a progressively adapting blood and non-blood model.

After the likelihoods for each pixel in the image are defined. The segmentation of the frame is performed by the minimization of Eq.(3.5). Algorithm 1 presents the steps of the proposed B-mode approach.

Algorithm 1: Image-based segmentation method.

Input : B-mode frames, and total number of frames on the sequence N_f

Output: Curve corresponding to the lumen/wall interface $F_i(\mathbf{C}_i^*)\ \forall\ i$

Training phase:
begin
- Obtain R_l, R_n and χ from user annotations on f_1
- Generate $\mathbf{E}_x\ \forall\ x\ \in\ \{R_l, R_n\}$
- Generate a training set T_1
- Compute c and γ
- Train Π_1 with T_1 using c and γ
- $j = 1$

Deployment phase:
begin
- **for** $i = 1$ *to* N_f **do**
  - Generate $\mathbf{E}_x\ \forall\ x\ \in\ f_i$
  - Obtain $k(x)\ \forall x \in f_i$, $P(l|\mathbf{E}_x)$, and $P(n|\mathbf{E}_x)$ using Π_j
  - Compute A_j
  - **if** $A_j \geq \tau_1 \mid i = 1$ **then**
    - Set $\hat{v}_l(x) = P(l|\mathbf{E}_x)$ and $\hat{v}_n(x) = P(n|\mathbf{E}_x)$.
    - Set $\hat{v}_l(x) = 1 \forall x | r \leq \chi$ and $\hat{v}_n(x) = 0 \forall x | r > \chi$
    - Find $\mathbf{C}_i^*$ by the minimization of Eq. (3.5)
    - Return the segmentation result $F_i(\mathbf{C}_i^*)$
  - **Model adjustment phase:**
  - **else**
    - Generate a class mask M using $F_{i-1}(\mathbf{C}_i^*)$
    - Generate T_{j+1} using randomly selected entries from T_j, and samples corresponding to R_l and R_n in M
    - Train Π_{j+1} with T_{j+1}
    - Obtain $k(x)\ \forall\ x \mid d(x, \mathbf{C}_i) \geq w_b$ and $k(x)\ \forall\ x \mid -w_n \geq d(x, \mathbf{C}_i) \geq -w_b$using Π_{j+1}
    - Compute A_{j+1}
    - **if** $A_{j+1} \geq A_j$ **then**
      - j=j+1
      - Obtain $k(x)\ \forall x \in f_i$, $P(l|\mathbf{E}_x)$, and $P(n|\mathbf{E}_x)$ using Π_j
      - Go to 16
    - **else**
      - Go to 16

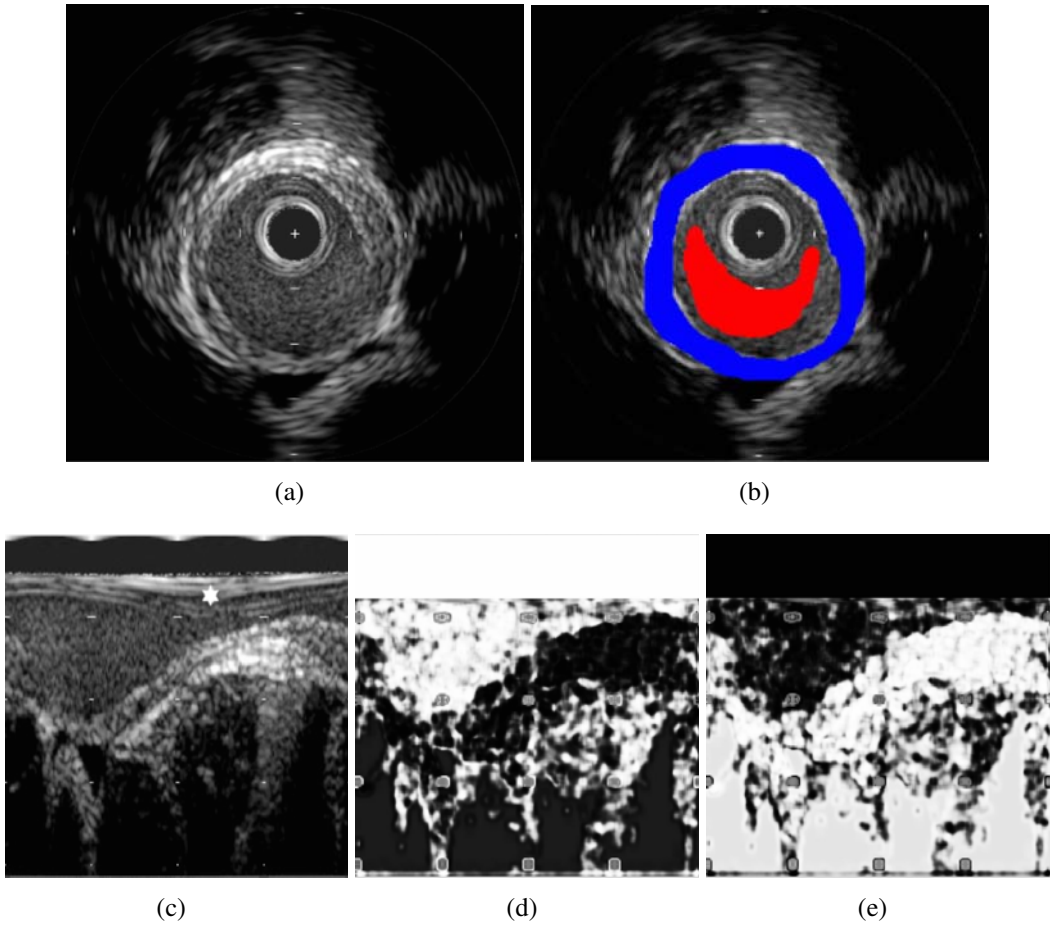

(a) (b)

(c) (d) (e)

Figure 3.4: Examples depicting (a) the first frame of a sequence, (b) the corresponding user annotation for blood and non-blood (red and blue, respectively), (c) the corresponding polar B-mode representation, and the likelihood estimates for (d) lumen and (e) non-lumen. The star in (c) indicates the radial location χ of the outer-most trace of the ringdown artifact selected by the user.

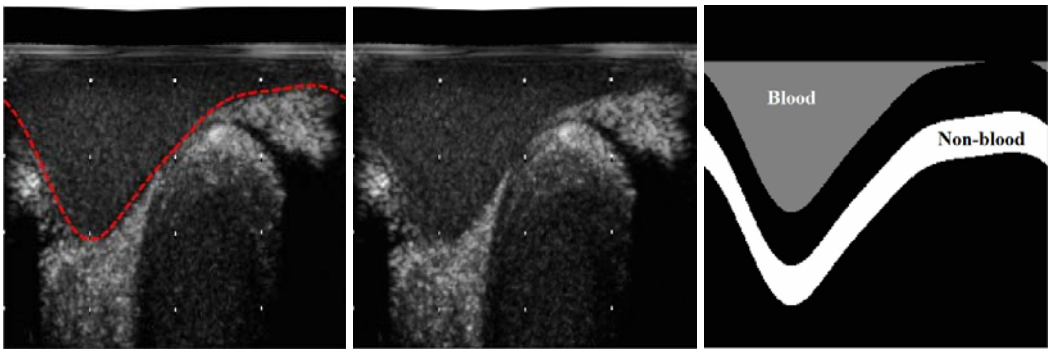

(a) (b) (c)

Figure 3.5: Examples depicting (a) the lumen segmentation result of a frame, (b) the next consecutive frame, and (c) the class mask which defines the regions considered as blood and non-blood.

3.3.4 RF-based approach

One approach to overcome the limitation regarding the variability on the IVUS system and B-mode reconstruction settings is to perform the segmentation employing the raw IVUS RF signal since it is not affected by transformation parameters or visualization settings (i.e., RF-based segmentation). While there exist several methods that make use of the RF signal for IVUS data analysis, the majority of these methods are focused on the characterization of atherosclerotic plaque composition. Nair *et al.* [51, 52] proposed a method known as "virtual histology" (IVUS-VH) that is based on the analysis of some features extracted from the signal's power spectrum combined with classification trees. Kawasaki *et al.* [27, 28] proposed another method of tissue classification using the integrated backscatter that is a parameter derived from the RF signal. Our group has presented studies of the feasibility of blood [55] and contrast agent [40] characterization on IVUS data using one-class support vector machines employing features intended to quantify speckle and features based on frequency-domain measures computed from the RF raw signal, the signal envelope, and the log-compressed signal envelope. Most recently, the feasibility of using wavelet analysis for plaque characterization using the RF amplitude has been studied by Katouzian *et al.* [26] and Roodaki *et al.* [62].

The proposed segmentation method is based on the analysis of the physics involved in the interaction of the ultrasound impulse signal with the elements of the vessel. Specifically, we employ a scattering model of the RF signal corresponding to the intensity of the echoes received by the ultrasound transducer generated by different elements of the vessel which are modeled as a collection of point scatterers. The scattering model is used to compute features which permit the classification of the RF signal into two categories:

luminal blood and non-luminal-blood. Similar to the IB method, the confidence of the resulting classification is employed as the likelihood for each pixel to each class.

In summary, the proposed RF-based segmentation approach consist of the following steps:

1. The RF signal corresponding to the A-lines of an IVUS frame is divided into a number of overlapping partitions. Then, we employ the scattering model and an inverse problem approach to compute a differential backscatter cross section (DBC) value of the scatterers that generate the RF signal contained in a partition of an A-lines. The result of this computation is a matrix containing the computed DBC values for all A-line partitions (i.e., DBC reconstruction).

2. We perform texture analysis on the DBC image to generate a set of features that characterize each region of the IVUS RF data.

3. A luminal-blood detection model is generated by training a SVM classifier using the RF signal corresponding to user-provided annotations from the luminal-blood and non-blood regions (R_l and R_n, respectively) on a set of randomly chosen frames from the sequences to segment.

4. For each frame to be segmented, we compute the DBC reconstruction, we compute texture features from the RF data corresponding to that frame and we perform the classification of each pixel of the DBC image employing the luminal-blood detection model.

5. The posterior probability of the classification result is used as the likelihoods for each pixel.

6. The lumen contour is obtained by the minimization of the probabilistic cost function Eq(3.5).

The details of each step are provided next:

3.3.5 Generation of features from the RF signal

In order to understand the generation of features from the RF signal, it is necessary to introduce further details regarding the principles of the generation of the received RF signal by the interaction of the ultrasound wave with the elements in the vessel.

3.3.6 Intravascular ultrasound principles:

Sound waves are mechanical disturbance that moves as a pressure wave through a medium. The intensity I of the sound wave is defined as the average power carried by a wave per unit area normal to the direction of propagation of the wave over time [66]. The velocity of an ultrasound wave through a medium c varies with the physical properties of the medium. This speed c is determined by the density ρ of the medium, while the distance covered by one cycle of the wave is the wavelength $\lambda = \frac{c}{f}$. As a sound wave passes from one medium into another, a part of the incident wave is reflected at the boundary and a part spreads in the second medium (Fig. 3.6(a)). The acoustic impedance Z refers to the physical property of a medium which determines the reflection of the sound waves and it is computed as the product of the propagation velocity and the density of the medium:

$$Z = c\dot{\rho} \tag{3.6}$$

A discontinuity on a medium refers to local changes in compressibility, density, or both. If in a medium the sound wave interacts with a discontinuity of dimensions comparable or smaller than the wavelength of the incident sound wave (i.e., scatterer), part of the intensity of the wave is scattered in all directions [31] (Fig. 3.6(b)). The ultrasound signal scatterer by a single scatterer is defined by the differential scattering cross section σ which is the power scattered per solid angle per unit incident intensity (*W/sr*) [65].

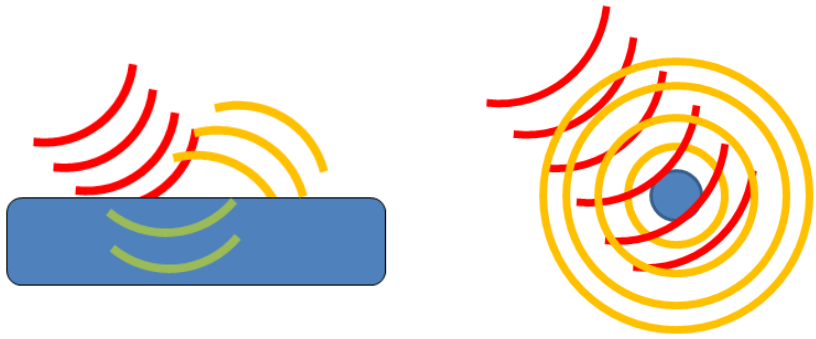

(a) (b)

Figure 3.6: (a) Ultrasound reflection when objects are larger in comparison with the wavelength of the incident wave, and (b) ultrasound scattering when objects are smaller in comparison with the wavelength of the incident wave.

The Rayleigh scattering theory implies that the scattering cross section is proportional to the fourth power of the incident wave frequency and to the square of the scatterer volume, a behavior independently of the geometry of the scatterer [59, 47]. For weak scatterers, (i.e., with density and compressibility that only differ slightly from the surrounding medium), and for arbitrary shape, the differential scattering cross section at an angle θ is given by:

$$\sigma(\theta) = \frac{k^4 V_s^2}{16\pi^2} \left| \left(1 - \frac{\kappa_0}{\kappa_e}\right) - \left(1 - \frac{\rho_0}{\rho_e}\right) \cos(\theta) \right|^2 , \tag{3.7}$$

where $k = \frac{2\pi}{\lambda}$ is the wave number, V_s is the volume of the scatterer, ρ_0 and ρ_e are the densities (g/cm^3) of the surrounding medium and of the scatterer, respectively, and κ_0 and

κ_e are their respective compressibility ($cm^2/dyne$). The ultrasound signal scattered in the direction opposite to the direction of the incident wave (i.e, $\theta = 180°$) is referred to as the differential backscattering cross section (DBC) [65].

As an ultrasound beam propagates through a heterogeneous medium, part of its energy is removed from the beam as a function of distance by reflection, scattering, geometric attenuation, and absorption. The attenuation of an ultrasound wave in a medium depends on the frequency of the wave and is described by the attenuation coefficient μ which is the sum of the individual coefficients for scatter and absorption in units of decibels per centimeter. A simple phenomenological model used in practice to write the intensity $I(r)$ at a distance r from the transduce as

$$I(r) = I(0)e^{-\mu r}.$$

An ultrasound transducer is a device that converts electrical energy into mechanical energy and vice versa, and it consists of one or more piezoelectric crystals or elements. For a standard disc shaped transducer initially the beam is of comparable diameter to the transducer D as the series of ultrasound waves that make up the beam travel parallel to each other. This is known as the near-field or Fresnel zone F_z and can be computed as:

$$F_z = \frac{D^2}{4\lambda}. \tag{3.8}$$

Beyond the Fresnel zone, some of the energy escapes along the periphery of the beam to produce a gradual divergence of the ultrasound beam (Fig. 3.7). In this region, called the far-field zone, the axial pressure decrease approximately according to $1/r$ [66]. The angle of divergence $\Delta\Theta$ (in degrees) of the beam can be computed as:

$$\sin(\Delta\Theta) = 1.22\frac{\lambda}{D} \tag{3.9}$$

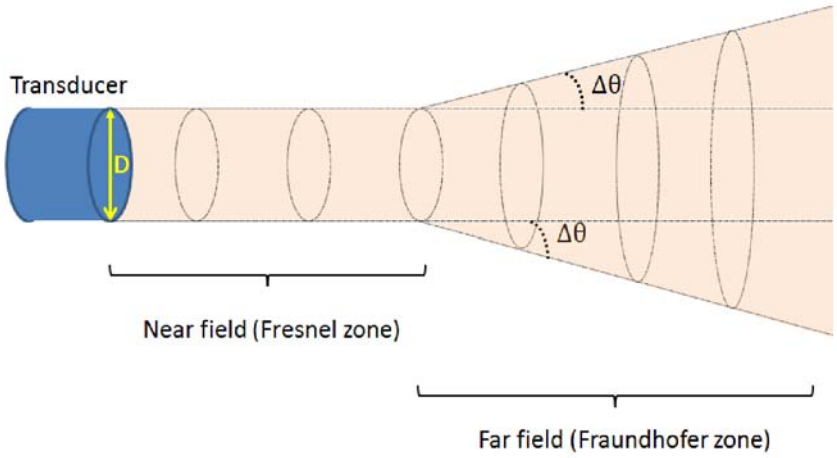

Figure 3.7: Characteristics of the ultrasound beam for a standard disc shaped transducer.

Scattering model: The structures in the vessel imaged by IVUS such as collagen fibers or red blood cells (RBC) are smaller than the wavelength of ultrasound wave. Such small structures provide scatter that returns to the transducer through multiple pathways. The sound that returns to the transducer from such nonspecular reflectors is no longer a coherent beam. It is instead the sum of a number of component waves that produces a complex pattern of constructive and destructive interference back at the source. This interference pattern is known as speckle. The reflected echo signal in the direction of the incident wave by each scatterer is an attenuated replica of the incident wave which signal intensity depends on the DBC of the scatterer [72].

For the case of multiple point scatterers, it is possible to model the collective interaction of all the scatterers using the Born approximation [18] which assumes that it is possible to use the principle of superposition to represent the total scattered wave as a sum of the individual reflections of each point scatterer. Based on this principle, Fontaine *et al.* [18] presented a model to describe and simulate the ultrasound signal backscattered by red

blood cells. In that work, the generation of the ultrasound signal is described by a convolution integral involving a transducer transfer function, a scatterer prototype function, and a function representing the spatial arrangement of the scatterers. Later, Rosales *et al.* [58] presented a similar formulation of the scattering model for the simulation of IVUS images. That model assumed that the IVUS signal can be approximated with a physical model based on the transmission and reception of ultrasound waves that radially penetrate the arterial structures.

Similarly with Rosales' work [58], in this work we employ a scattering model to simulate the received IVUS RF signal by representing the structures in the vessel as a finite arrangement of point scatterers with an associated DBC. The main difference from this work, is that in we employ the simulated RF signals to extract information to characterize the IVUS RF signal using an inverse problem approach instead of using the scattering model for the forward problem consisting in the generation of synthetic IVUS images.

For our formulation, we employ polar coordinates with the origin located in the center of the IVUS catheter. Consider a 3D distribution of N scatterers that interact with the ultrasound beam. Let $(r_i)\ \forall i \in \{1, 2, ..., N_s\}$ be the distance of one scatterer from the ultrasound transducer, and σ_i be its corresponding DBC. The proposed scattering model, compute the total scattered wave in the direction of the transducer as a sum of the individual reflections of each point scatterer determined by its DBC value σ_i and the intensity of the incident wave Ω at a distance r_i from the transducer, that is attenuated by the medium

and the divergence of the beam. Using this model, the received ultrasound signal corresponding to the A-line j of the frame RF signal at time t is given by:

$$\hat{S}_j(t) = \sum_{i=1}^{N} \sigma_i \Psi(r_i) e^{-\mu r_i} \Omega\left(t, \frac{r_i}{c}\right), \tag{3.10}$$

where $\Psi(r_i)$ defines the decrease on the intensity of the beam when the scatterer is in the far-field given by:

$$\Psi(r_i) = \begin{cases} 1, & \text{if } r_i <= F_z \\ \frac{F_z}{r_i}, & \text{if } ri > Fz \end{cases} \tag{3.11}$$

and $\Omega\left(t, \frac{r_i}{c}\right)$ is the ultrasound wave intensity at the distance of the scatterer r_i from the transducer.

Since IVUS uses the pulse echo method which consists of short ultrasound pulses, the wave intensity is approximated by a Gaussian which envelopes the intensity distribution [69]:

$$\Omega(t, r_i) = I(0) \exp\left[\frac{-(t - \frac{r_i}{c})^2}{2\varsigma^2}\right] \sin\left(\omega\left(t - \frac{r_i}{c}\right)\right), \tag{3.12}$$

where $\omega = 2\pi f$ is the angular velocity, and ς is the standard deviation of the Gaussian envelope of the pulse signal which is determined by the ultrasound pulse duration Δt.

Computation of DBC: Our hypothesis is that the scattering model can be used to determine the DBC of the scatterers σ_i that generate a selected section of the RF signal by minimizing the difference between the real IVUS RF signal $S(t)$ and the signal generated by the scattering model $\hat{S}(t)$. The scattering model employed in this work, is a phenomenological approximation of the ultrasound interaction with the scatterers of the vessel that has been previously used for the simulation of IVUS data [58].

In order to use this model, the main challenge is that the characteristics of the RF signals depend on the spatial arrangement of the scatterers which is unknown. To overcome this challenge, we propose to use a model for the position of the scatterers and obtain the modeled RF signal produced with the scattering model which is then compared with the true RF signal.

Specifically we perform an stochastic minimization process on which we generate N_s random samples of 3D scatterers' spatial distributions for the dimensions of the vessel. Then, we divide the real and modeled RF signals corresponding to each angular position of the ultrasound transducer θ (i.e., A-line) of an IVUS frame into N_p 50%-overlapping partitions of the same size p_s. We assume that all the scatterers that generates the section of the signal contained in each partition are of the same type with the same DBC value $\sigma_{\theta,p}$.

In this work, we propose compute the DBC value for the scatterers corresponding to each partition by the minimization of the differences between the root mean square (RMS) power of the real RF signal contained in the partition $R_{\theta,p}$ computed with

$$R_p = \sqrt{\frac{1}{t_f - t_o} \sum_{t_o}^{t_f} S(t)^2 dt}, \tag{3.13}$$

were $t_o = r_o/c$ and $t_f = r_f/c$ correspond to the distance r_o and r_f which defines the partition, and the average of the RMS power of the N_s signals of the corresponding partition in the modeled signal $\hat{R}^s_{\theta,p}(\sigma_{\theta,p})$. Additionally, we introduce a regularization term which promotes the similarity of the computed DBC values across the neighboring G_δ A-lines. Here, δ refers to the cardinality of the neighbors and $N_n = 2\delta$ is the number of neighbors. Then, for recovering the DBC values corresponding to the scatterers that generate

the signal in each partition we solve:

$$\arg\min_{\sigma_{\theta,p}} \alpha \left(\frac{1}{N_s} \sum_{s=1}^{Ns} \hat{R}^s_{\theta,p}(\sigma_{\theta,p}) - R_{\theta,p} \right)^2 + (1-\alpha) \sum_{j \in G_\delta} \left(\sigma_{\theta,p} - \sigma_{j,p}\right)^2 . \tag{3.14}$$

This formulation yields to a sparse linear system of coupled equations which we solve using LU decomposition.

Note that given the small size of RBC, the number of scatterers required for the simulation may be extremely large (order of 1.37×10^7 [58]). To overcome this limitation we employ the voxel approach [35] in which we define groups of scatterers (i.e., voxels) which allow us to generate quantities of scatterer that are possible to emulate. In this approach, the approximate number of scatterers that would exist within the volume corresponding to the region of the vessel that is swept by the ultrasound beam is computed by considering the average volume of a single scatterer (e.g., RBC). Then, the volume contained in a voxel V_v and the number of scatterers that this voxel can contain is determined using the obtained quantities. Finally, the number of voxels required to emulate the total number of scatterers required in the volume is computed.

Feature extraction: The result of employing the proposed DBC computation approach is a matrix (i.e., DBC reconstruction) which contains the DBC values for each partition as computed by the scattering model on the RF signal corresponding to a frame of the IVUS sequence (Fig. 3.8). Note that, as compared with the B-mode reconstruction, the DBC reconstruction provide relatively more homogeneous values for the regions corresponding to lumen, specially in the distal lumen areas.

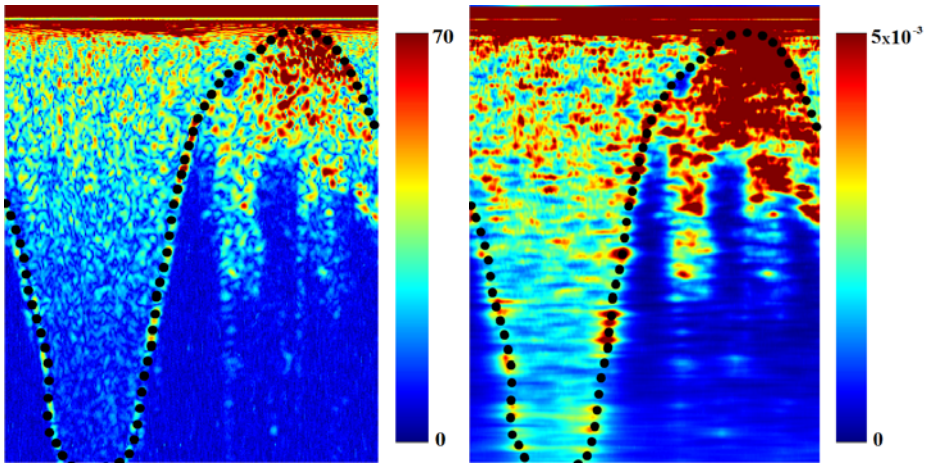

(a) (b)

Figure 3.8: Examples of (a) an IVUS B-mode reconstruction in polar representation using a color palette and (b) its corresponding DBC reconstruction. The dotted line indicates the region corresponding to lumen.

3.3.7 Generation of likelihoods based on RF signal analysis

Since the spatial distribution of blood scatterers is extremely complicated to emulate considering the large variability of scatterers positions due to the continuous blood flow and other phenomena (e.g., aggregation of RBC), and the fact that the employed model is a simple approximation of the real scattering phenomenon, the sole computation of DBC values may not be sufficient for determining the region corresponding to lumen. However, after the examination of the DBC reconstructions, it can be noted that the regions corresponding to blood in lumen depict a different pattern from the other regions. Therefore, we propose to employ texture features similarly with the proposed approach for the computation of the likelihoods from the B-mode images. However, in this case, the texture descriptors are computed from the DBC reconstruction image instead of the B-mode reconstruction. The generation of the likelihoods is also divided into two phases: training

and deployment.

1. Training: We require the user to select samples of lumen and non-lumen regions (R_l and R_n, respectively) on N_T randomly selected B-mode IVUS frames of the sequence to be segmented. We generate the DBC reconstruction H_i for each frame using the RF signals corresponding to the selected B-mode frames. We compute the texture energies $L(x) \forall\, x \in \{R_l, R_n\}$ in H_i. A feature vector $\mathbf{E}_x \in R^{25}$ containing the computed texture energies for each pixel corresponding to R_l and R_n is associated to its corresponding class $k(x) = \{l, n\}$. A training set T is then generated using the feature vectors and the classes of each pixel. Next, a SVM model Π is computed using the training set T_1 and the optimal c and γ.

Deployment: For each of the frames f_i to be segmented, H_i is computed by solving the inverse scattering problem described in Eq (3.14). Then, we compute $L(x) \forall\, x \in H_i$ we compute a vector $\mathbf{E}_x$ for every pixel in the frame H_i. We employ the luminal-blood detection model Π. Finally, the posterior probabilities of the classification result $P(k|\mathbf{E}_x)$ for each pixel are then used as the learned likelihoods $\hat{v}_l(x)$ and $\hat{v}_n(x)$. The result is an image where the pixels with high probability of being blood have a value near to one (Fig. 3.9).

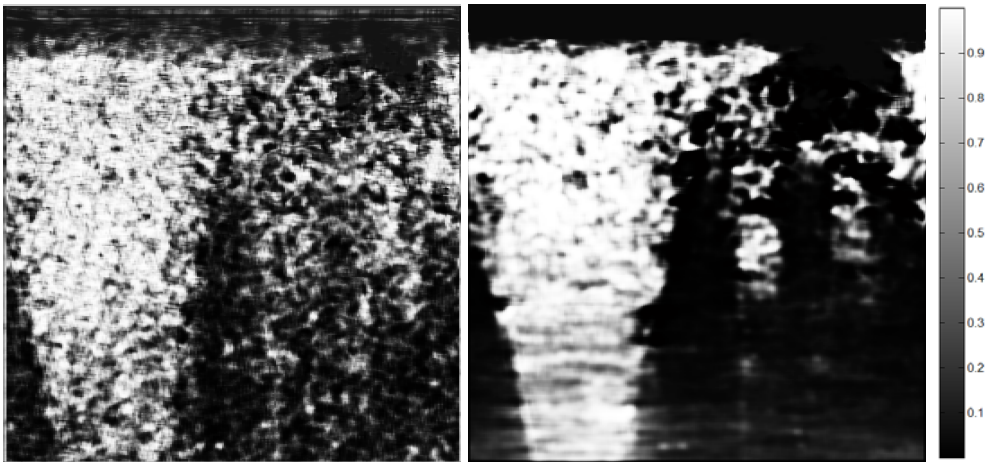

(a) (b)

Figure 3.9: Examples of the likelihood of each pixel to belong to luminal blood computed with (a) the B-mode and (b) the DBC reconstructions.

Algorithm 2 presents an overview the steps of the proposed B-mode approach.

3.4 Cost function minimization

To deform the lumen contour until it reaches the best segmentation, it is necessary to find the values of $\mathbf{C}^*$ that minimize the cost function of Eq. (3.5). In this work, we propose to use a line search method for this minimization. In a line search method, the optimal value $\mathbf{C}^*$ is computed iteratively. At every iteration k, the new value for $\mathbf{C}_{k+1}$ is computed by:

$$\mathbf{C}_{k+1} = \mathbf{C}_k + \alpha_k \mathbf{P}_k \ , \tag{3.15}$$

where α_k is the step length at the iteration k and $\mathbf{P}_k$ is a descent or search direction. A popular way to find an adequate value of α_k is by searching the one that satisfies the Wolfe

Algorithm 2: RF-based segmentation method.

Input : RF-data corresponding to the frames of the sequence to segment, and total number of frames on the sequence N_f

Output: Curve corresponding to the lumen/wall interface $F_i(\mathbf{C}_i^*)$.

Training phase:
begin
    Randomly select N_t frames from the sequence
    for *f=1 to* N_t **do**
        Obtain R_l, R_n and χ from user annotations on the B-mode reconstruction of f_1
        Generate H_i from the RF-data corresponding to f_i
        Generate $\mathbf{E}_x$ for all pixels x in H_i
    Generate a training set T
    Compute c and γ
    Train Π with T using c and γ
Deployment phase:
begin
    for *f=1 to* N_f **do**
        Generate H_i from the RF-data corresponding to f_i
        Generate $\mathbf{E}_x$ for all pixels x in H_i
        Obtain $P(l|\mathbf{E}_x)$, and $P(n|\mathbf{E}_x)$ using Π
        Set $\hat{v}_l(x) = P(l|\mathbf{E}_x)$ and $\hat{v}_n(x) = P(n|\mathbf{E}_x)$.
        Set $\hat{v}_l(x) = 1 \forall x | r \leq \chi$ and $\hat{v}_n(x) = 0 \forall x | r > \chi$
        Find $\mathbf{C}_i^*$ by the minimization of Eq. (3.5)
        Return the segmentation result $F_i(\mathbf{C}_i^*)$

conditions ([54], Chapter 3):

$$U(\mathbf{C}_k + \alpha_k \mathbf{P}_k) \leq U(\mathbf{C}_k) + u_1 \alpha_k \nabla U(\mathbf{C}_k)^\intercal \mathbf{P}_k \tag{3.16}$$

$$\nabla U(\mathbf{C}_k + \alpha_k \mathbf{P}_k)^\intercal \mathbf{P}_k \geq u_2 \nabla U(\mathbf{C}_k)^\intercal \mathbf{P}_k \ . \tag{3.17}$$

In this work, we employ $u_1 = 10^{-4}$ and $u_2 = 0.9$ as recommended in [54].

For selecting the descent direction $\mathbf{P}_k$ at each iteration k we have several options. We will discuss two options below.

The steepest descent method: One of the simplest ways to approximate the solution of optimization problems is by using the steepest descent method ([54]). For an objective function $U(\mathbf{C})$, the steepest descent method is a line search method that iteratively moves along a search direction given by:

$$\mathbf{P_k^G} = -\frac{\nabla U(\mathbf{C}_k)}{|\nabla U(\mathbf{C}_k)|} \ . \tag{3.18}$$

Although this method is robust and guarantees convergence to a local minimal, the main disadvantage is that this method may take a large number of iterations (i.e., time) to converge to the solution.

Broyden-Fletcher-Goldfarb-Shanno (BFGS) method: The BFGS method ([54]) converges to a solution faster when compared to the steepest descent method since it incorporates first and second order derivatives to find the point at which the gradient of the function is equal to zero. The BFGS algorithm is efficient since, instead of computing the inverse of the Hessian from scratch at every iteration, it is updated in a simple manner by taking into account the curvature measured in the most recent step. In this method, the search

direction at each iteration k is given by:

$$\mathbf{P}_k^B = -H_k \nabla U(\mathbf{C}_k) \, , \tag{3.19}$$

where the matrix H_k is the inverse of a positive definite approximation of the Hessian of the cost function at each iteration computed as:

$$H_{k+1} = (I - \rho_k \mathbf{s}_k \mathbf{y}_k^{\mathsf{T}}) H_k (I - \rho_k \mathbf{y}_k \mathbf{s}_k^{\mathsf{T}}) + \rho_k \mathbf{s_k} \mathbf{s}_k^{\mathsf{T}} \tag{3.20}$$

with

$$\rho_k = \frac{1}{\mathbf{y}_k^{\mathsf{T}} \mathbf{s_k}} \tag{3.21}$$

were $\mathbf{s_k} = \mathbf{C}_{k+1} - \mathbf{C}_k$ and $\mathbf{y}_k = \nabla U(\mathbf{C}_{k+1}) - \nabla U(\mathbf{C}_k)$ which must satisfy the curvature condition

$$\mathbf{s}_k^{\mathsf{T}} \mathbf{y}_k > 0 \, . \tag{3.22}$$

In our problem, depending on the IVUS image to segment, the cost functions $U(\mathbf{C})$ may have many local minima mostly due to the similarity between the gray levels distributions of lumen and other regions of the vessel. Therefore, solving the cost function with the BFGS method could lead us to an incorrect segmentation if the descent step is too large in a given iteration. Note that the steepest descent method is robust but slow, while BFGS is fast but may converge into an incorrect solution (Fig. 3.10). Therefore, we propose a strategy for combining the strengths of the two methods which uses a linear combination of the descent directions from steepest descent ($\mathbf{P}^G$) and BFGS ($\mathbf{P}^G$) methods to compute a new descent direction. The linear combination of these methods is denoted as ($\mathbf{P}^{GB}$) and therefore, we refer to this strategy as GB optimization .

GB optimization: An advantage of the BFGS algorithm over other Newton-based methods such as Levenberg-Marquart (LM) is the direct computation of the inverse of the Quasi-Hessian H. However, the reason we chose BFGS over LM is because the information obtained from the curvature condition Eq. (3.22).

When this condition is satisfied, the curvature of the function becomes more positive as the descent approaches to a minimum. However, if the curvature condition is not satisfied, a better descent direction is the negative gradient (i.e., steepest descent direction). Additionally, note that for small values of the product $\mathbf{s}_k^\intercal \mathbf{y}_k$, the computation of the update formula for the Hessian, or its inverse, is non-defined (the function is not locally convex). Then, by design there is more confidence in the BFGS descent direction if the value of ρ (Eq. (3.21)) is large and positive. On the other hand, for $\rho \approx 0$, the confidence in $\mathbf{P}_k^B$ is smaller and we prefer the steepest descent direction $\mathbf{P}_k^G$. Based on this analysis, we propose to compute the descent direction as a convex linear combination of both descent directions ([41]):

$$\mathbf{P}_{k+1}^{GB} = [\psi(\rho_k)\mathbf{P}_k^B + (1 - \psi(\rho_k))\mathbf{P}_k^G]. \tag{3.23}$$

where the function that controls the contribution of each descent direction $\psi(\rho)$ is defined as:

$$\psi(\rho) = \begin{cases} 0 & \text{if } \rho < 0 \\ \frac{\rho^2}{K+\rho^2} & \text{otherwise .} \end{cases} \tag{3.24}$$

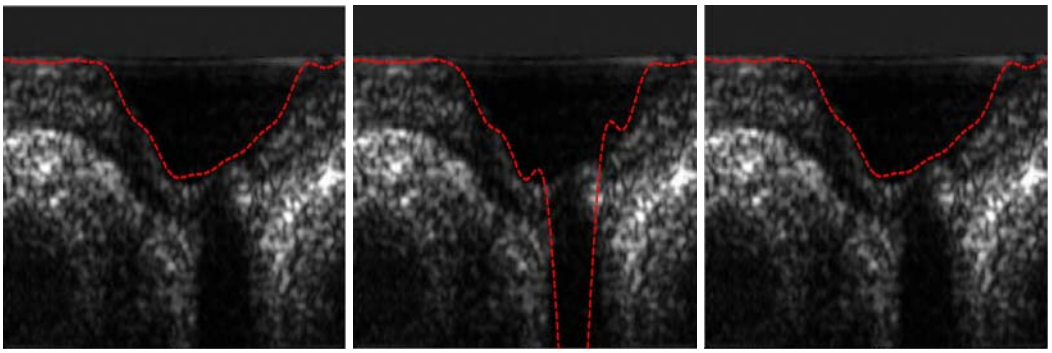

(a) (b) (c)

Figure 3.10: Examples of a segmentation result on a 20 *MHz* IVUS frame using (a) steepest descent optimization (72 iterations), (b) BFGS optimization (38 iterations), and (c) GB optimization (26 iterations).

3.4.0.1 Starting point

We define the starting point for the first frame to be segmented by setting the offset coefficient a_0 to be equal to the mean of the radial coordinates of the blood samples given by the user. The values for the rest of the coefficients were experimentally found and set to $\{a_i, b_i\} = 0.1 \; \forall \; i > 0$.

Chapter 4

Results and discussion

In this section, we provide an analysis of the sensitivity of the probabilistic segmentation method with respect to its parameters. In addition, a comparison between the results employing the B-mode-based approach with state of the art segmentation methods existing in the literature, and a comparison between the segmentation results employing the B-mode and RF-based approaches. The methods proposed in this dissertation were implemented using MATLAB. For the SVM classifier, we employed the implementation provided in the libSVM library ([8]).

4.1 Sensitivity analysis

4.1.1 Similarity between lumen shape of consecutive frames

The robustness of the proposed IB method with respect to changes in appearance within an IVUS sequence is based on the assumption that the shape of the lumen of two consecutive frames is very similar. In order to quantitatively verify this observation we computed the Dice similarity coefficient [12] between the region defined as lumen by an observer for each pair of consecutive frames corresponding to the validation sequences described in Table 4.1. Figure 4.1(a) depicts the histogram of the obtained Dice similarities coefficients for the comparison of all the consecutive frames. Note that the similarity between consecutive frames is most of the time above 97% which supports our assumption. Similarly, we computed the maximum difference between the radial coordinate r in of the pixels corresponding to the same angle θ belonging to the lumen contour on each pair of consecutive frames $\max(F_i(r, \theta_j, \mathbf{C}_i) - F_{i+1}(r, \theta_j, \mathbf{C}_{i+1}))\ \forall j$. Figure 4.1(b) depicts the empirical distribution function of the maximum differences for all the frames of the validation set described in Table 4.1. Note that, for more than 90% of the frames the largest radial difference is less than 20 pixels and therefore, we set $w_b = 20$.

4.1.2 Probabilistic segmentation sensitivity analysis

The sharpness of the transition between classes is controlled by the parameter λ while the smoothness of the curve is determined by the number of Fourier coefficients N_k. The value of these parameters may have an impact in the accuracy of the segmentation curve.

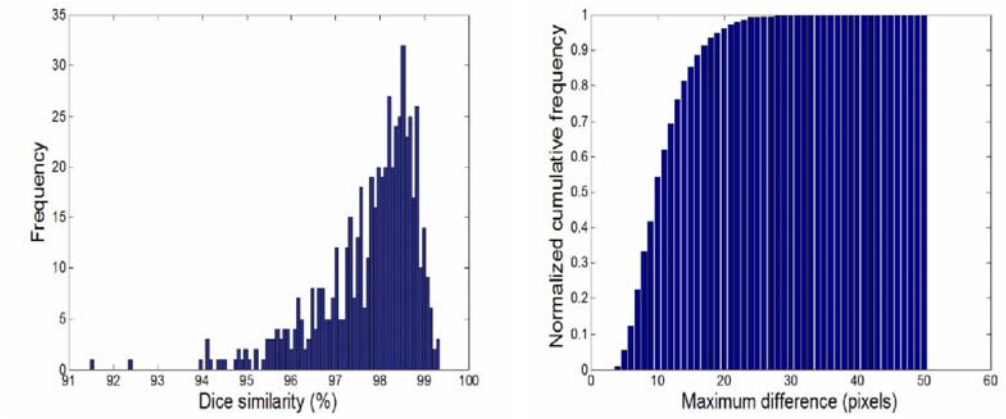

(a) (b)

Figure 4.1: (a) Histogram of the Dice similarities, and (b) normalized cumulative histogram of the maximal radial lumen contour differences for consecutive frames.

To evaluate the sensitivity of our method with respect to these parameters, we performed segmentation of ten randomly selected frames from the available IVUS sequences (120 frames in total) using different values for λ and N_k, and computed the similarity of the results with the manual segmentation by an observer using the Dice coefficient. Figure 4.2(a) depicts the result of the sensitivity analysis with respect to λ using $N_k = 5$ while Fig. 4.2(b) depicts the results of the sensitivity analysis with respect to N_k using $\lambda = 0.5$. Note that our method is robust with respect to the value of λ, while the segmentation result remains approximately constant when $\lambda \geq 0.3$. Similarly, note that our method is also robust with respect to the number of Fourier coefficients.

4.1.3 DBC reconstruction sensitivity analysis

Two experiments were performed to analyze the impact of the techniques described in Sec. 3.3.5 for the computation of the DBC reconstruction, employing a synthetic IVUS

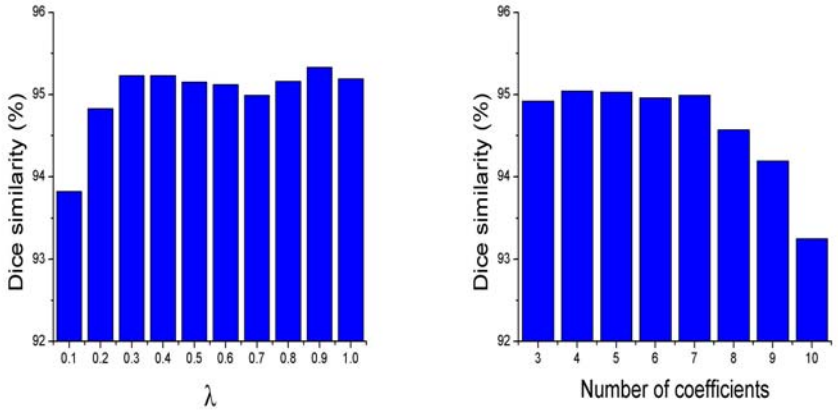

(a) (b)

Figure 4.2: Depiction of the sensitivity analysis for (a) λ and (b) N_k.

RF data generated with the scattering model. The experiments were designed to analyze the following aspects:

1. For the computation of the DBC reconstruction, we use a stochastic minimization process on which we generate random samples of three-dimensional spatial distributions of scatterers. Therefore, it is important to analyze the effect of the number of random samples N_s used for computing the DBC for each partition.

2. The volume of the voxels V_v determine the quantity of scatterers to simulate. However, when working with real data, the actual number, size, and location of the scatterers is unknown. Furthermore, the time-varying blood flow and the inhomogeneous distribution of RBCs make it even harder to determine the spatial distribution of scatterers. Therefore, it is important to evaluate the impact of using a scatterers' density that is different from the actual density.

A two-layer (i.e., luminal blood and wall) synthetic IVUS was generated using a random distribution of scatterers spatial positions with arbitrary DBC values of $\sigma_b = 1$ and $\sigma_w = 30$ for blood and wall, respectively (Fig. 4.3). The size of the voxels for the synthetic IVUS data (i.e., V_v =3.37$\times 10^{-3}$ *mm*^{3}) was determined by considering an axial resolution of 150 μm for a Boston Scientific Galaxy 2 IVUS system with a 40 *MHz* catheter [36]. The standard deviation of the Gaussian envelope of the pulse signal ς can be determined by taking into account that the axial resolution is equal to one half of the spatial pulse length (SPL) [70]. For an axial resolution of 150 μm the SPL is 300 μm which corresponds to $\Delta t = 0.194$ μs considering the average speed of sound in biological tissues $c = 1,540$ *m/s*. Since in a Gaussian function, at six times the standard deviation we have approximately 99% of the signal, we compute the value of $\varsigma = \Delta t/6$. The characteristics of the IVUS beam were determined considering an ultrasound transducer of diameter $D = 0.6$ *mm* [58]. The RBC voxel density (number of RBC voxels per *mm*^{3}) was determined according to the volume of a RBC modeled as a cylinder (i.e., 1.1945 $\times 10^{-7}$ *mm*^{3}) using the typical values of RBC diameter and thickness [17], and the typical hematocrit Concentration (i.e., 35%). The wall voxel density was determined by modeling the wall scatterers as cylindrical collagen fibers with a volume of 1.9792 $\times 10^{-15}$ *mm*^{3} according to the measurements reported by Elbischger *et al.* [15]. The values for the attenuation coefficient for lumen and wall were set to 0.2 and 0.52 *dB/cm* at 1 *MHz* as reported by Culjat *et al.* [11].

To analyze the sensitivity of our method with respect to the employment of the stochastic minimization process, the proposed method was employed to compute the DBC for each

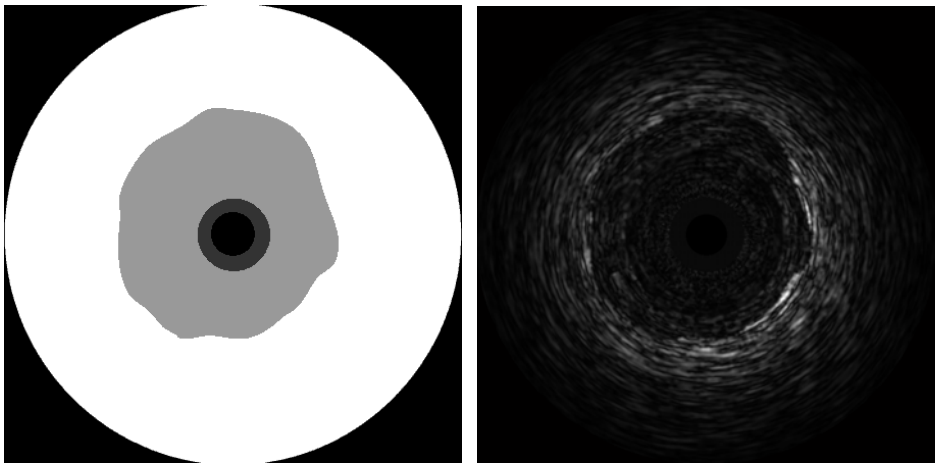

(a) (b)

Figure 4.3: (a) Mask employed to generate the synthetic IVUS RF data and (b) Cartesian B-mode reconstruction of the syntectic data.

partition of the RF signal of the syntectic IVUS data using different values for the number of samplings N_s. The mean and standard deviation of the recovered DBC values for each blood and non-blood partition were computed. For this experiment we employed the original voxel volume, the cardinality of the neighbors was set to $\delta = 2$, and the regularization term was set to $\alpha = 0.5$. Figure 4.4 depicts the mean and standard deviations of the computed DBC value for blood with respect to the number of samplings. Note that, as the number of samples increase the computed DBC values approximate to the value employed for generating the synthetic RF signal. Moreover, the variability on the resulting DBC values decreases as we employ larger number of samplings.

In a second experiment, the impact of using characteristics of scatterers different from those used to create the synthetic RF data is evaluated. In this experiment the DBC for blood and wall was computed employing the characteristics of blood scatterers (i.e., volume and attenuation coefficient). Additionally we evaluated the sensitivity of our method

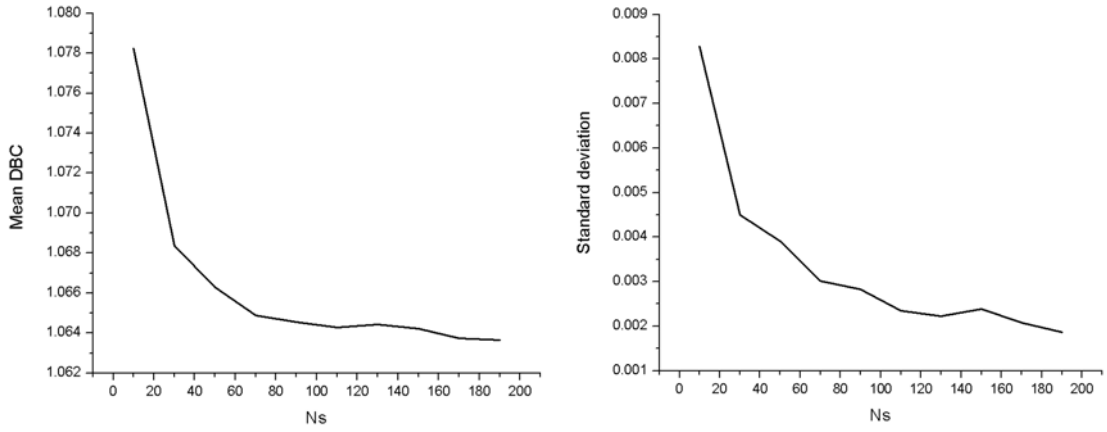

(a) (b)

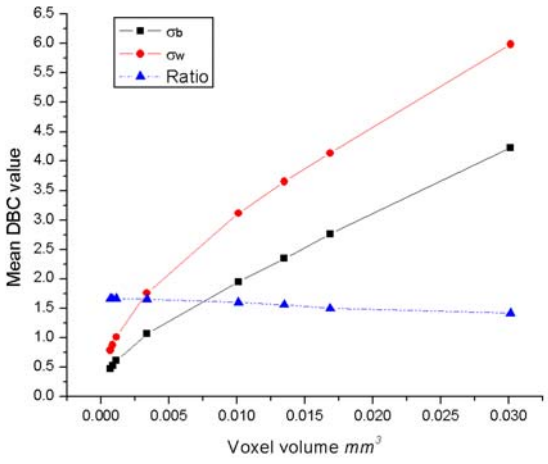

(c)

Figure 4.4: (a) Mean and (b) standard deviation of the computed DBC values for blood in the synthetic RF data with respect to the number of samplings employed.

with respect to different voxel volumes. Figure 4.4(c) depicts the result of this experiment. Note that the computed DBC value for blood approximates to the original DBC value when using the original voxel volume employed for generated the synthetic RF data. The computed DBC value for wall does not correspond with the original value for all the different voxel volumes employed. This is expected considering that we are employing the scatterers characteristics corresponding to blood. However, we can note that the ratio between the recovered values remains more less constant independently from the voxel volume employed. This experiment demonstrates the feasibility of the proposed DBC computation method for the detection of the luminal-blood even if the model is not using the exact parameters that generates real the RF signal.

4.2 Image-based approach results

The performance of the IB method in the segmentation of IVUS B-mode Cartesian images, was evaluated on twelve non-gated stationary IVUS sequences from two IVUS systems using different frequencies. Six sequences were acquired from human coronary arteries from different patients using a Volcano system with a 20 MHz Eagle Eye catheter, and the remaining six were acquired from Rabbit's aortas using a Boston Scientific Galaxy 2 system with a 40 MHz Atlantis SR Catheter. From each sequence a number of consecutive frames corresponding to regions of interest within the artery (different degrees of stenosis) were selected and manually segmented by human observers (585 frames in total). To compare the IB method with other existing segmentation methods, we asked three research groups to perform segmentation in the selected data sets using their segmentation methods. The

original IVUS data was provided to each author and they provide us with the segmentation results. The methods used for comparison correspond to the methods presented by Unal *et al.* (UNL) ([71]), Papadogiorgaki *et al.* (PAP) ([56]), and Katouzian *et al.* (KAT) ([25]). The details of each sequence and the number of segmented frames provided by each group are listed in Table 4.1 [1].

Table 4.1: Information about the IVUS sequences and the number of segmented frames using our method (IB), Unal's method (UNL), Papadogiorgaki's method (PAP), and Katouzian's method (KAT).

Sequence information				Number of segmented frames			
ID	IVUS system	Frequency	Subject	IB	UNL	PAP	KAT
1	Volcano	20 *MHz*	Human	50	50	50	48
2	Volcano	20 *MHz*	Human	50	50	50	0
3	Volcano	20 *MHz*	Human	50	50	50	0
4	Volcano	20 *MHz*	Human	50	50	50	0
5	Volcano	20 *MHz*	Human	50	50	50	0
6	Volcano	20 *MHz*	Human	50	50	50	0
7	Boston Scientific	40 *MHz*	Rabbit	50	50	50	48
8	Boston Scientific	40 *MHz*	Rabbit	50	50	50	48
9	Boston Scientific	40 *MHz*	Rabbit	50	50	50	48
10	Boston Scientific	40 *MHz*	Rabbit	50	50	50	48
11	Boston Scientific	40 *MHz*	Rabbit	50	50	50	48
12	Boston Scientific	40 *MHz*	Rabbit	35	35	35	32

We performed automatic segmentation of the sequences using $\lambda = 0.4$ and $N_k = 5$ as the use of these values reports the largest Dice similarity in the sensitivity analysis. The starting point for the first frame to be segmented is defined by setting the offset coefficient a_0 to be equal to the mean of the radial coordinates of the blood samples provided by the user. The values for the rest of the coefficients set to $\{a_i, b_i\} = 0.1 \; \forall \; i > 0$. The rest of the parameters were empirically set to $\tau_1 = 80$, and $w_n = 50$.

The performance of the methods was evaluated by comparing our segmentation results

[1] The missing segmentation results were not provided by the corresponding authors.

with the manual segmentation of the same frames by two observers. Specifically, we computed the Dice D coefficient and the Jaccard J index between the proposed method and the expert segmentation. In addition, we computed the Hausdorff distance [23] which measures the maximum difference between the corresponding lumen curves.

The agreement between the areas corresponding to lumen according to each segmentation was evaluated using linear regression, coefficient of determination and Bland-Altman analysis ([2]). The number of times the model was computed along with its total time, and the average time for segmenting each frame are listed in Table 4.2. The mean Dice similarity and standard deviation results for the comparison of both manual segmentation and each automatic segmentation method are depicted as a box plot in Fig 4.5. The segmentation results corresponding to each of the sequences for the comparison of both observers, and the IB, UNL, PAP, and KAT methods and both observers, are listed in Tables 4.3, 4.4, 4.5, 4.6, and 4.7, respectively.

Figure 4.6 depict the linear regression and Bland-Altman plots for the comparison of the lumen areas corresponding to the segmentations of Observer 1 and Observer 2. Figures 4.7 to 4.14, depict the linear regression and Bland-Altman plots for the comparison of the lumen areas corresponding to the segmentation of both observers segmentation with the segmentation obtained with the IB, UNL, PAP, and KAT methods respectively. Note that the linear regression results indicate a good agreement between the luminal area detected by the IB method with the luminal area defined by the observers and less dispersion as compared by the area detected by the other methods. Moreover, the IB method reports a higher coefficient of determination when compared with the other methods. From the Bland-Altman plots it can be observed that IB method perform with a low mean bias and

Table 4.2: Average segmentation time per frame (ST), number of times that the SVM model was trained (MT), and total SVM model training time (TT) for each sequence.

ID	ST (s)	MT	TT (s)
1	3.04	1	3.38
2	3.43	1	4.13
3	3.42	1	3.21
4	3.14	1	7.23
5	2.71	1	2.38
6	4.21	1	9.45
7	5.11	1	8.52
8	7.08	2	33.2
9	5.75	1	9.54
10	5.15	2	24.31
11	5.16	1	13.12
12	4.55	1	13.02

less dispersion when compared with the other methods. Figures 4.15 and 4.16 depict examples of the segmentation results for each method along with the segmentation by the Observer 1.

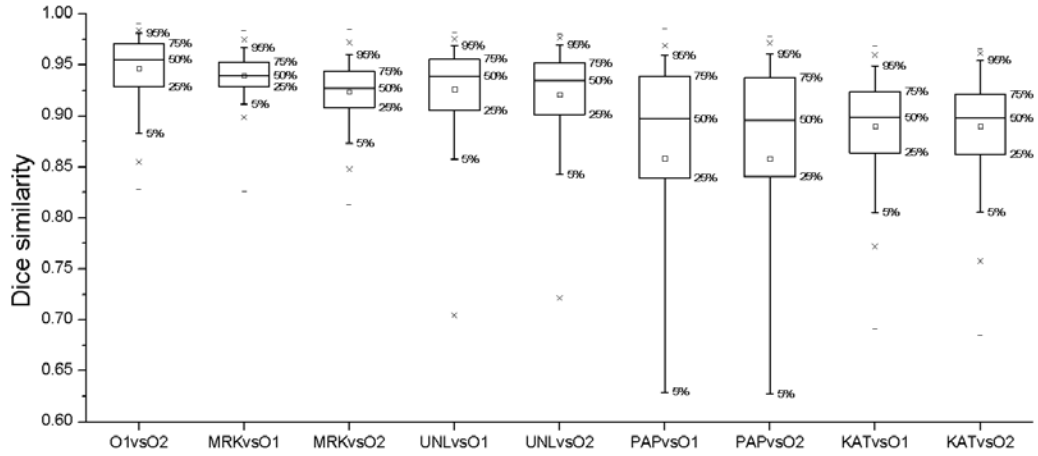

Figure 4.5: Box plot of the Dice similarity coefficient for the comparison of the segmentation results in all the sequences of the proposed method (IB), Unal's method (UNL), Papadogiorgaki's method (PAP), and Katouzian's method (KAT) with the manual segmentation of two observers.

Table 4.3: Mean Dice similarity, Jaccard index, and Hausdorff distance and standard deviations (std) for the comparison of the segmentation results of Observer 1 and Observer 2. The mean is denoted by μ and the for the standard deviation by σ.

	Dice		Jaccard		Hausdorff	
ID	μ (%)	σ(%)	μ (%)	σ(%)	μ (%)	σ(%)
1	94.17	2.42	89.07	4.24	8.51	3.43
2	92.92	1.86	86.84	3.23	12.88	4.11
3	90.10	3.11	82.13	5.15	15.69	4.59
4	92.73	2.96	86.58	5.04	14.35	4.24
5	92.53	3.06	86.24	5.23	14.05	5.73
6	92.53	1.79	86.15	3.06	25.09	6.51
7	96.58	1.11	93.40	2.06	7.05	2.23
8	97.67	0.51	95.45	0.98	7.56	2.12
9	96.45	1.04	93.16	1.92	12.97	4.94
10	96.35	0.96	92.97	1.78	10.54	3.68
11	97.84	0.52	95.77	1.00	5.57	1.34
12	96.46	1.03	93.18	1.92	11.99	3.59
Average	**94.69**	**1.70**	**90.08**	**2.97**	**12.19**	**3.88**

Table 4.4: Mean Dice similarity, Jaccard index, and Hausdorff distance and standard deviations (std) for the comparison of the segmentation results of Observer 1 and Observer 2 with IB. The mean is denoted by μ and the for the standard deviation by σ.

	IB vs O1						IB vs O2					
	Dice		Jaccard		Hausdorff		Dice		Jaccard		Hausdorff	
ID	μ (%)	σ(%)	μ (%)	σ(%)	μ (%)	σ(%)	μ (%)	σ(%)	μ (%)	σ(%)	μ (%)	σ(%)
1	92.70	1.19	86.41	2.06	10.43	2.43	92.40	1.80	85.92	3.09	9.35	2.63
2	92.19	1.48	85.55	2.53	12.02	2.78	89.64	1.93	81.27	3.15	16.05	3.27
3	92.44	2.82	86.07	4.54	12.64	4.39	90.92	3.57	83.53	5.72	13.65	4.51
4	93.21	1.98	87.35	3.44	13.93	3.34	92.55	2.14	86.21	3.64	14.24	2.87
5	93.08	3.38	87.23	5.59	13.49	5.68	92.17	2.90	85.61	4.91	14.11	4.92
6	94.65	1.32	89.88	2.35	13.98	3.26	89.83	1.48	81.57	2.44	26.61	4.39
7	92.81	3.18	86.75	5.34	11.42	4.64	92.19	3.35	85.68	5.57	11.30	3.95
8	93.85	1.48	88.45	2.60	15.49	3.87	93.58	1.50	87.97	2.62	14.84	3.80
9	93.57	1.20	87.94	2.12	13.69	3.56	93.78	1.19	88.31	2.09	12.96	3.59
10	93.16	1.81	87.25	3.18	16.37	4.27	93.10	2.00	87.15	3.49	16.02	4.17
11	92.30	1.50	85.73	2.58	12.99	3.11	92.93	1.10	86.81	1.92	11.72	2.85
12	95.50	1.96	91.45	3.45	13.74	4.58	95.22	1.87	90.93	3.32	14.32	5.28
Average	**93.29**	**1.94**	**87.50**	**3.31**	**13.35**	**3.83**	**92.36**	**2.07**	**85.91**	**3.50**	**14.60**	**3.85**

Table 4.5: Mean Dice similarity, Jaccard index, and Hausdorff distance and standard deviations (std) for the comparison of the segmentation results of Observer 1 and Observer 2 UNL. The mean is denoted by μ and the for the standard deviation by σ.

	UNL vs O1						UNL vs O2					
	Dice		Jaccard		Hausdorff		Dice		Jaccard		Hausdorff	
ID	μ (%)	σ(%)	μ (%)	σ(%)	μ (%)	σ(%)	μ (%)	σ(%)	μ (%)	σ(%)	μ (%)	σ(%)
1	90.24	1.80	82.26	3.02	13.94	2.86	89.78	1.42	81.49	2.34	15.53	2.65
2	90.18	1.90	82.17	3.12	20.14	5.86	90.39	2.81	82.59	4.60	20.74	6.98
3	93.26	2.75	87.50	4.73	12.11	4.56	88.31	3.40	79.23	5.48	16.94	4.18
4	96.25	1.02	92.79	1.88	9.42	2.30	93.42	2.96	87.79	5.02	13.04	4.58
5	94.79	4.30	90.36	6.73	11.14	6.01	93.00	3.89	87.15	6.40	12.23	5.70
6	92.50	2.31	86.12	4.01	24.00	6.24	95.51	1.74	91.46	3.13	13.87	5.42
7	95.59	1.17	91.57	2.15	8.34	2.13	95.65	1.19	91.69	2.17	8.03	2.09
8	91.16	9.56	84.88	13.15	21.43	23.21	90.43	9.53	83.63	12.94	22.59	22.95
9	91.22	2.42	83.94	4.07	20.98	7.59	91.25	2.57	84.01	4.33	20.77	8.38
10	88.33	8.31	80.01	12.57	32.14	23.46	88.49	7.83	80.16	11.90	31.45	22.05
11	93.52	1.10	87.84	1.93	9.73	1.29	94.07	0.57	88.82	1.02	8.68	1.18
12	95.32	1.08	91.07	1.96	13.52	3.16	96.23	1.24	92.77	2.27	11.78	3.57
Average	**92.69**	**3.14**	**86.71**	**4.94**	**16.41**	**7.39**	**92.21**	**3.26**	**85.90**	**5.13**	**16.31**	**7.48**

Table 4.6: Mean Dice similarity, Jaccard index, and Hausdorff distance and standard deviations (std) for the comparison of the segmentation results of Observer 1 and Observer 2 with PAP. The mean is denoted by μ and the for the standard deviation by σ.

	PAP vs O1						PAP vs O2					
	Dice		Jaccard		Hausdorff		Dice		Jaccard		Hausdorff	
ID	μ (%)	σ(%)	μ (%)	σ(%)	μ (%)	σ(%)	μ (%)	σ(%)	μ (%)	σ(%)	μ (%)	σ(%)
1	70.87	3.52	54.99	4.15	46.70	5.43	70.99	3.49	55.13	4.08	48.19	6.48
2	85.62	2.95	74.97	4.50	25.68	4.34	86.41	2.53	76.15	3.89	26.18	4.91
3	89.55	2.78	81.18	4.60	16.17	3.61	88.21	2.52	79.00	3.99	18.77	4.71
4	94.66	0.89	89.87	1.60	13.07	3.14	91.11	2.73	83.77	4.46	18.63	4.27
5	92.69	10.11	87.40	11.08	14.10	21.13	92.45	9.73	86.95	11.32	13.98	20.48
6	88.74	2.03	79.82	3.19	26.51	4.78	93.47	2.67	87.85	4.51	17.75	6.16
7	85.45	9.45	75.45	10.73	25.42	31.31	84.16	9.25	73.44	10.31	26.72	31.41
8	64.08	15.80	49.05	16.77	72.30	33.58	63.53	15.75	48.41	16.51	73.77	33.19
9	86.59	13.87	78.35	16.88	43.90	64.46	87.82	14.40	80.48	17.54	39.22	65.81
10	90.09	8.83	82.84	11.22	25.53	27.87	89.45	8.78	81.77	11.16	26.64	27.43
11	90.96	7.34	84.01	9.16	20.38	30.71	91.36	7.54	84.73	9.50	19.65	31.02
12	93.60	9.91	89.06	12.23	17.11	25.18	93.30	9.95	88.56	12.29	18.28	24.96
Average	**86.07**	**7.29**	**77.25**	**8.84**	**28.91**	**21.30**	**86.02**	**7.45**	**77.19**	**9.13**	**28.98**	**21.74**

Table 4.7: Mean Dice similarity, Jaccard index, and Hausdorff distance and standard deviations (std) for the comparison of the segmentation results of Observer 1 and Observer 2 with KAT. The mean is denoted by μ and the for the standard deviation by σ.

	KAT vs O1						PAP vs O2					
	Dice		Jaccard		Hausdorff		Dice		Jaccard		Hausdorff	
ID	μ (%)	σ(%)	μ (%)	σ(%)	μ (%)	σ(%)	μ (%)	σ(%)	μ (%)	σ(%)	μ (%)	σ(%)
1	82.73	4.19	70.75	5.82	25.36	4.11	82.87	4.64	71.00	6.50	22.32	3.39
2	N.A.	N.A.	N.A.	N.A.	N.A.	N.A.	N.A.	N.A.	N.A.	N.A.	N.A.	N.A.
3	N.A.	N.A.	N.A.	N.A.	N.A.	N.A.	N.A.	N.A.	N.A.	N.A.	N.A.	N.A.
4	N.A.	N.A.	N.A.	N.A.	N.A.	N.A.	N.A.	N.A.	N.A.	N.A.	N.A.	N.A.
5	N.A.	N.A.	N.A.	N.A.	N.A.	N.A.	N.A.	N.A.	N.A.	N.A.	N.A.	N.A.
6	N.A.	N.A.	N.A.	N.A.	N.A.	N.A.	N.A.	N.A.	N.A.	N.A.	N.A.	N.A.
7	90.21	3.38	82.33	5.53	14.75	4.23	89.49	3.50	81.15	5.69	15.43	4.69
8	89.32	4.07	80.93	6.54	23.83	9.42	88.99	4.01	80.39	6.49	25.35	9.10
9	89.62	1.67	81.23	2.74	25.59	3.59	90.73	1.94	83.08	3.26	23.53	4.69
10	88.69	3.94	79.88	6.15	22.67	9.24	88.68	3.80	79.87	5.96	24.11	9.12
11	93.32	2.17	87.54	3.77	11.77	2.50	93.93	1.78	88.60	3.13	11.22	2.04
12	89.49	2.50	81.06	4.08	23.47	5.81	88.68	2.81	79.77	4.55	24.62	6.06
Average	**89.05**	**3.13**	**80.53**	**4.95**	**21.06**	**5.56**	**89.05**	**3.21**	**80.55**	**5.08**	**20.94**	**5.58**

4.2.1 Results on a sequence with changes in appearance

To evaluate the robustness of the IB method respect to changes in the B-mode reconstruction parameters and large lumen shape changes, we performed an experiment using a modified version of Sequence 7 where we applied first a 90° rotation and then changes in the dynamic range compression every 10 frames. Figure 4.17 depicts the segmentation result on the first frame of each modified subsequence. In this case the average frame segmentation time was 4.51 *s*, the model was computed four times, and the total model computation time was 63.88 *s*. The mean Dice similarity of the comparison with the manual segmentation was 92.84% with a standard deviation of 2.19%. This results indicates the robustness of our method with respect to possible changes in appearance within an IVUS sequence due to changes in the B-mode reconstruction parameters, catheter rotations, or the natural changes on the physiology of the vessel.

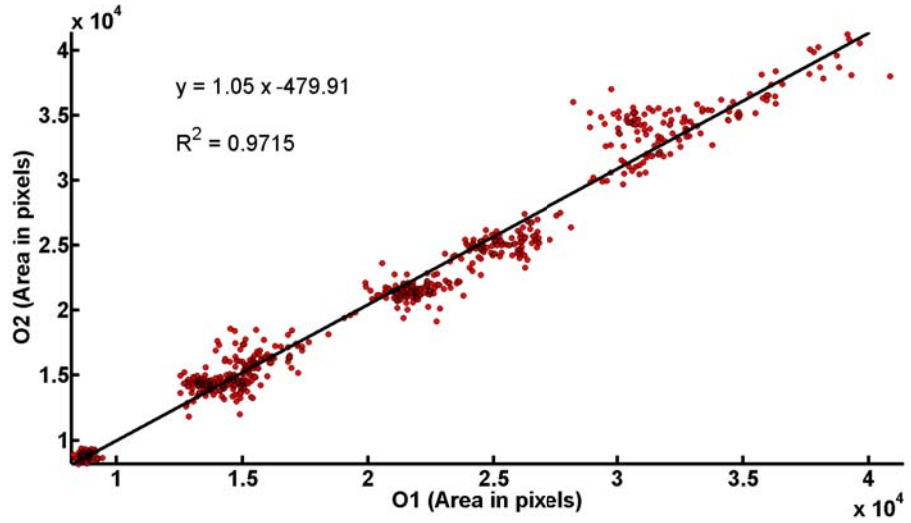

(a)

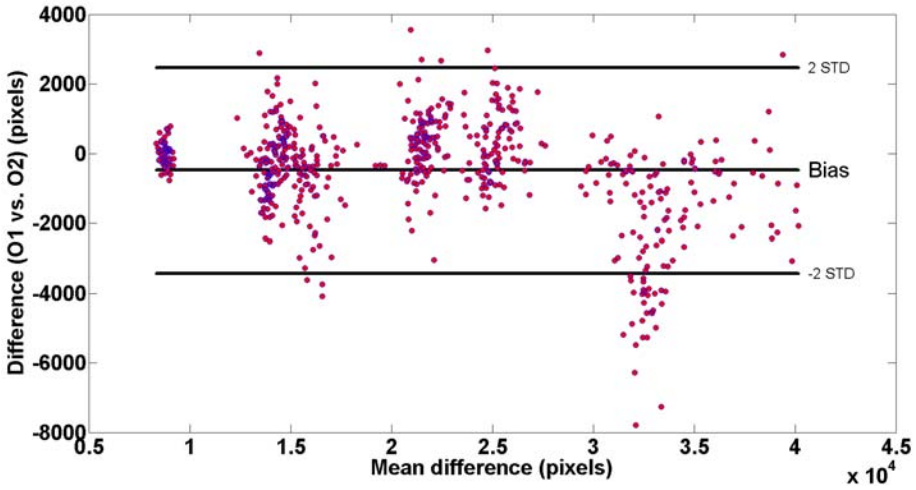

(b)

Figure 4.6: (a) Linear regression and (b) Bland-Altman plot for the comparison of the lumen areas segmented by Observer 1 (O1) with the areas segmented by Observer 2 (O2).

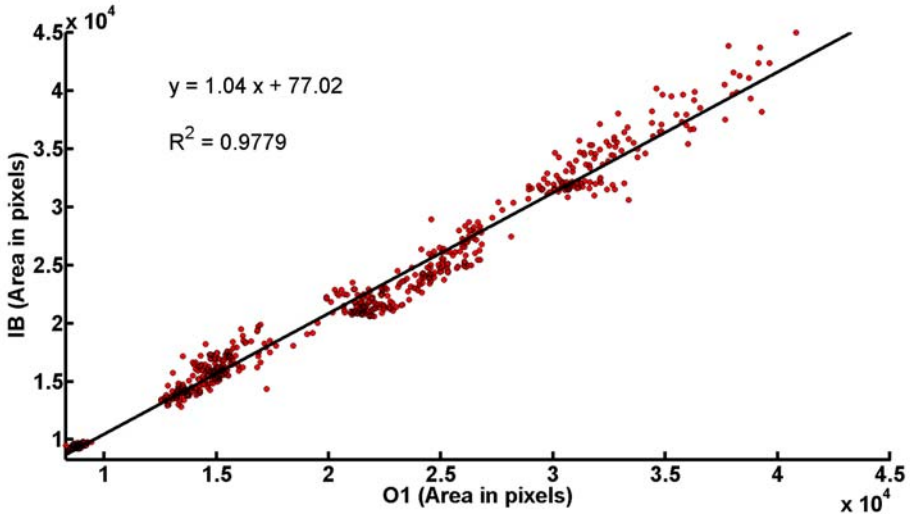

(a)

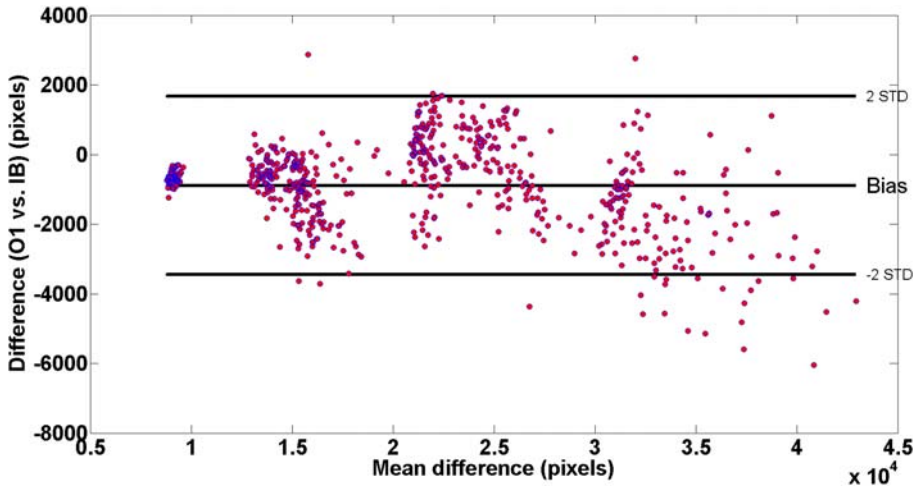

(b)

Figure 4.7: (a, b) Linear regression and (c,d) Bland-Altman plot for the comparison of the lumen areas segmented by Observer 1 (O1) with the areas segmented with the IB method.

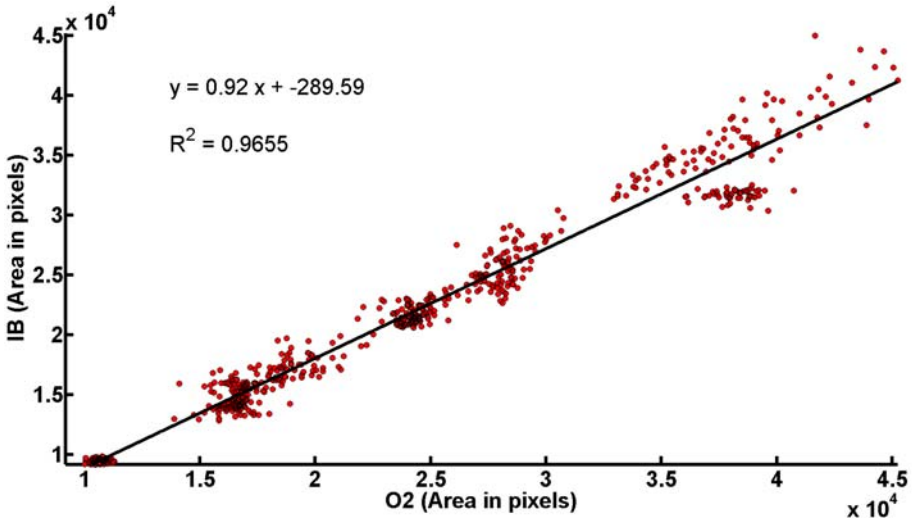

(a)

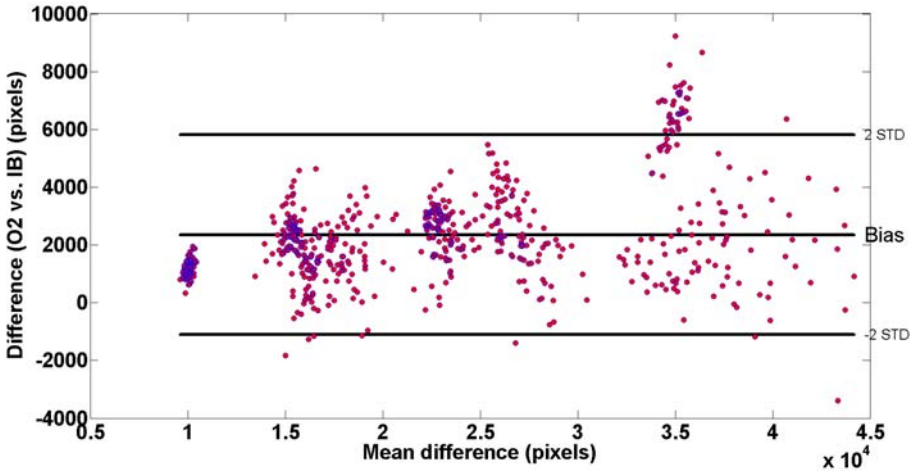

(b)

Figure 4.8: (a, b) Linear regression and (c,d) Bland-Altman plot for the comparison of the lumen areas segmented by Observer 2 (O2) with the areas segmented with the IB method.

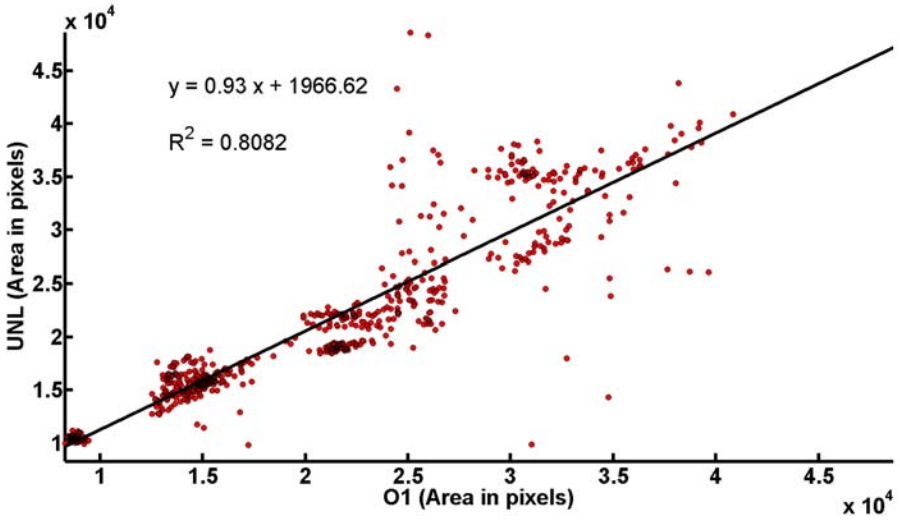

(a)

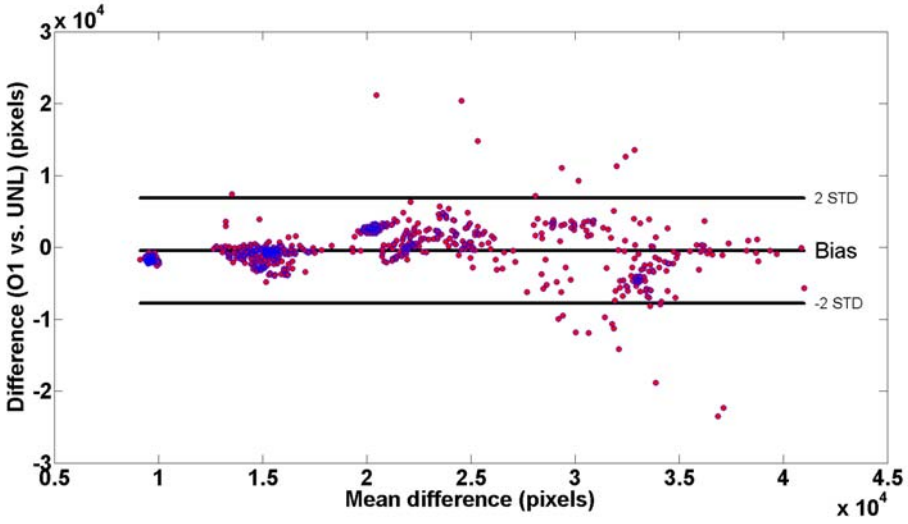

(b)

Figure 4.9: (a, b) Linear regression and (c,d) Bland-Altman plot for the comparison of the lumen areas segmented by Observer 1 (O1) with the areas segmented with the UNL method.

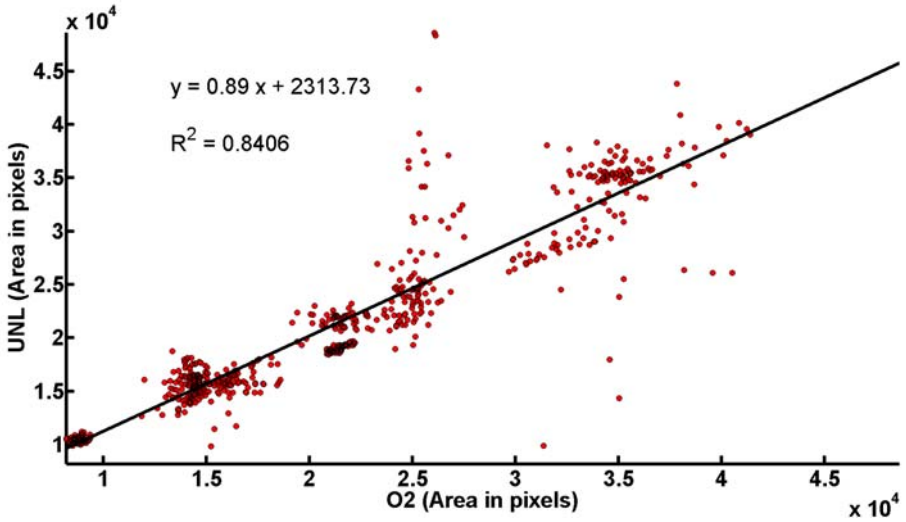

(a)

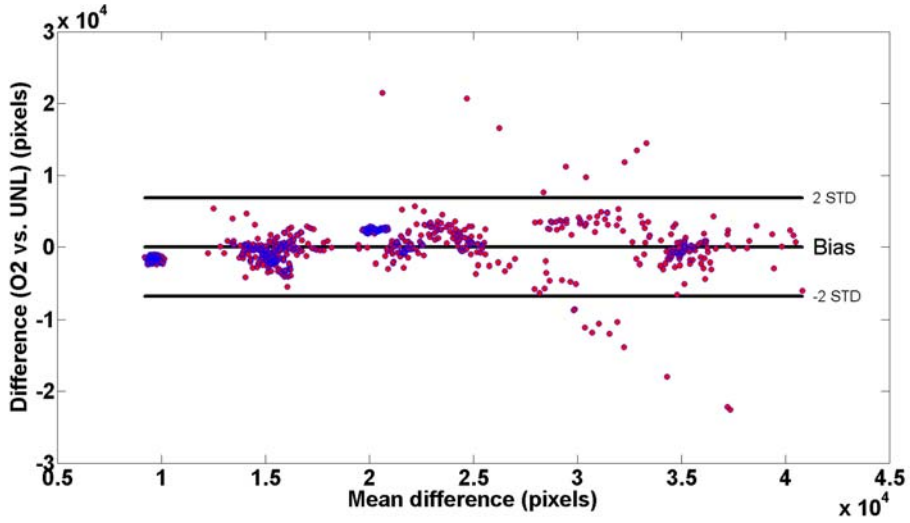

(b)

Figure 4.10: (a, b) Linear regression and (c,d) Bland-Altman plot for the comparison of the lumen areas segmented by Observer 2 (O2) with the areas segmented with the UNL method.

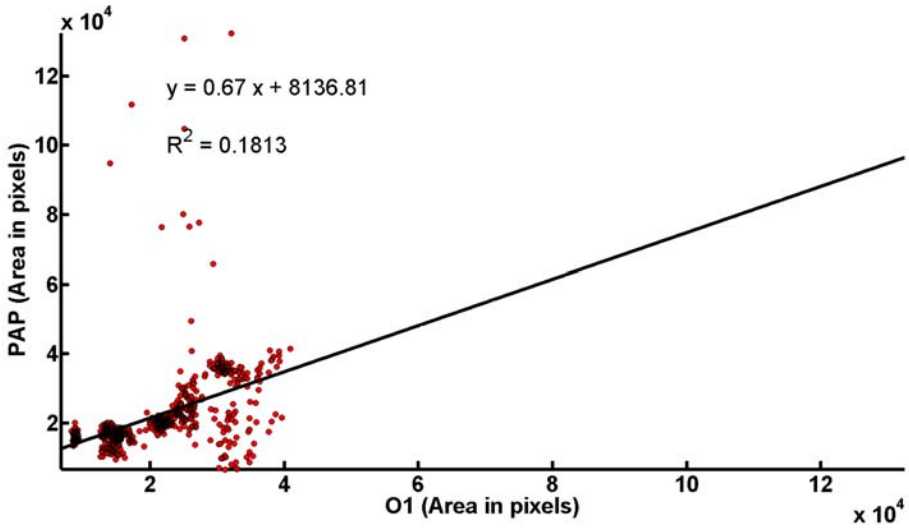

(a)

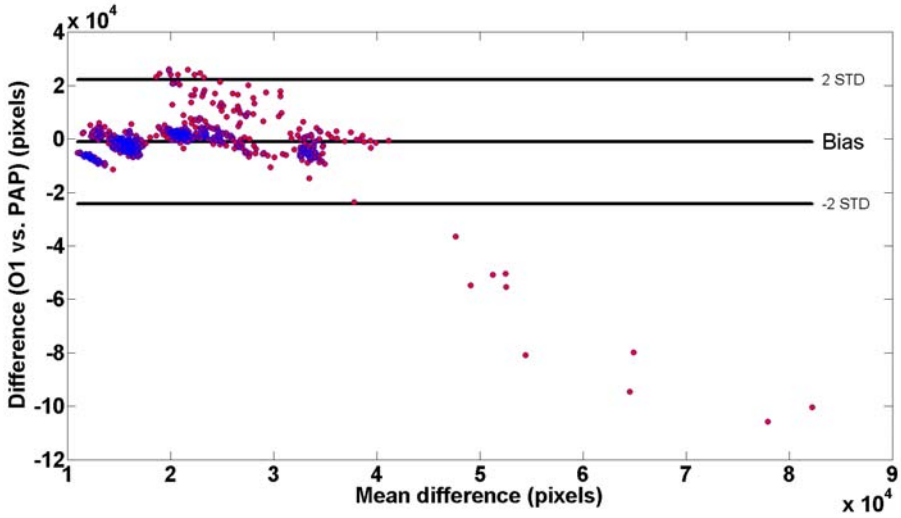

(b)

Figure 4.11: (a, b) Linear regression and (c,d) Bland-Altman plot for the comparison of the lumen areas segmented by Observer 1 (O1) with the areas segmented with the PAP method.

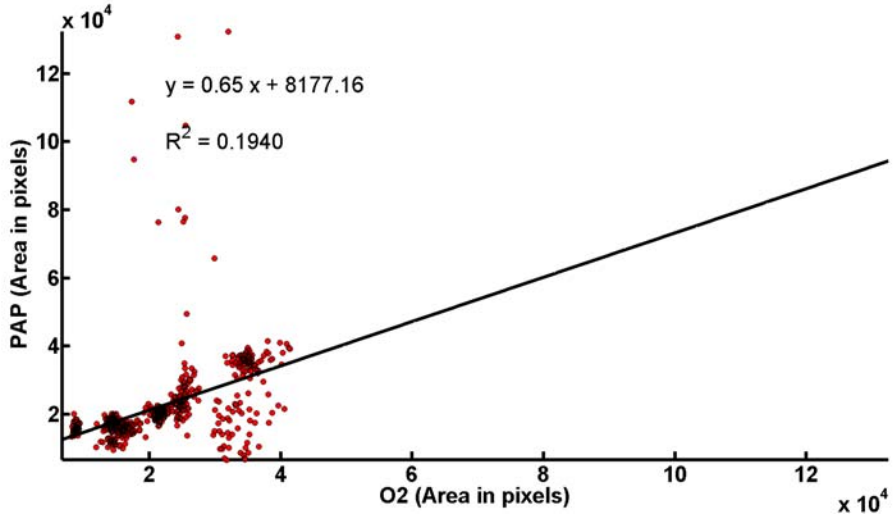

(a)

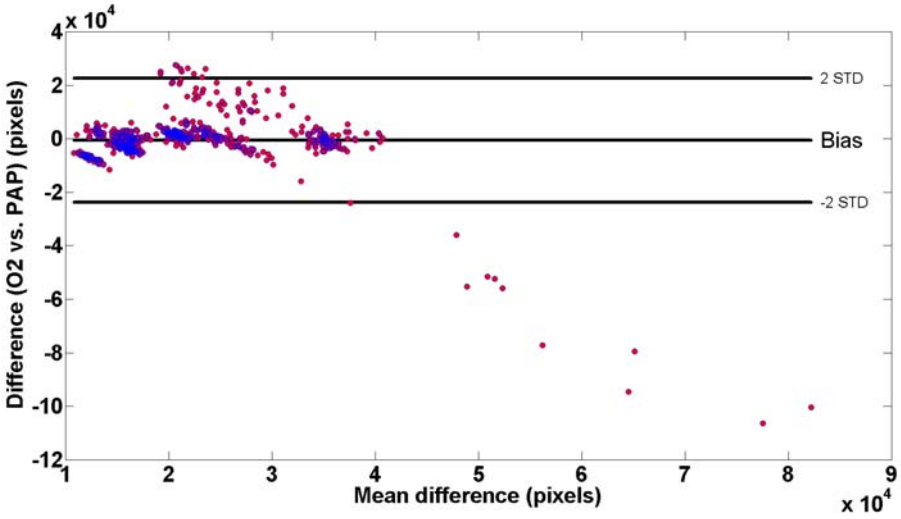

(b)

Figure 4.12: (a, b) Linear regression and (c,d) Bland-Altman plot for the comparison of the lumen areas segmented by Observer 2 (O2) with the areas segmented with the PAP method.

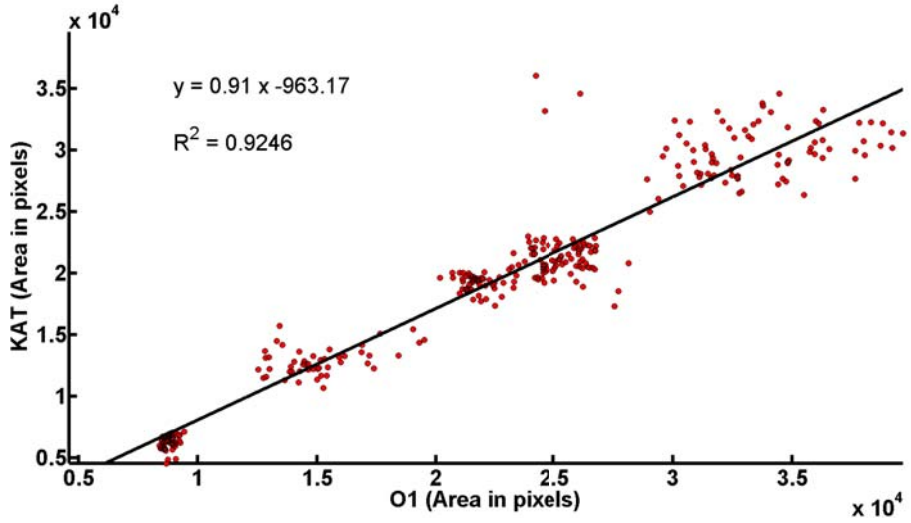

(a)

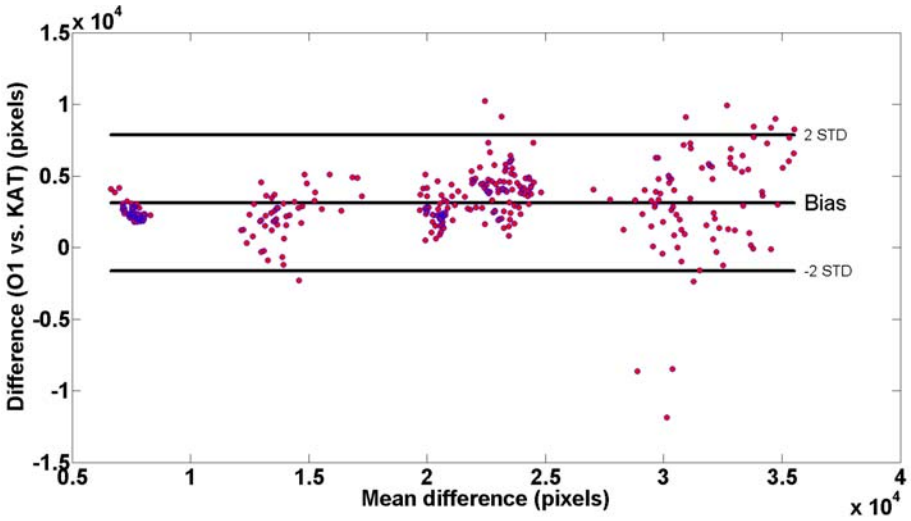

(b)

Figure 4.13: (a, b) Linear regression and (c,d) Bland-Altman plot for the comparison of the lumen areas segmented by Observer 1 (O1) with the areas segmented with the KAT method.

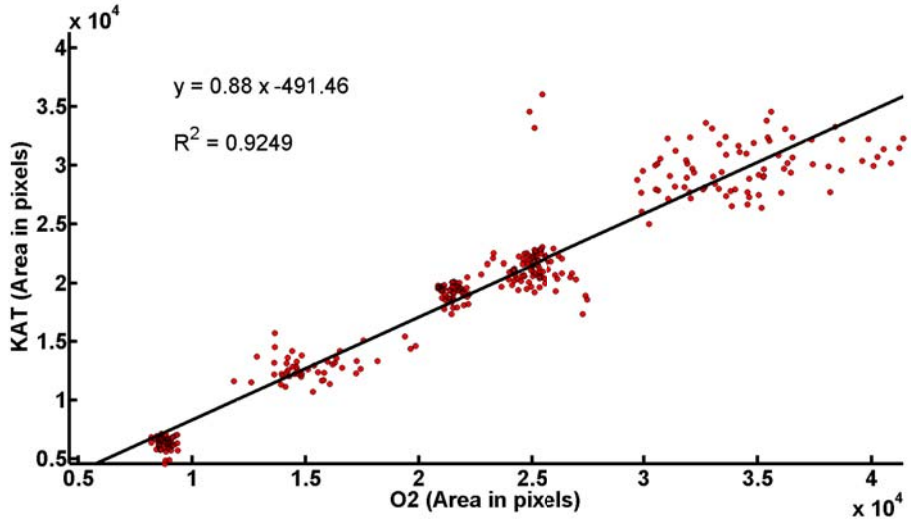

(a)

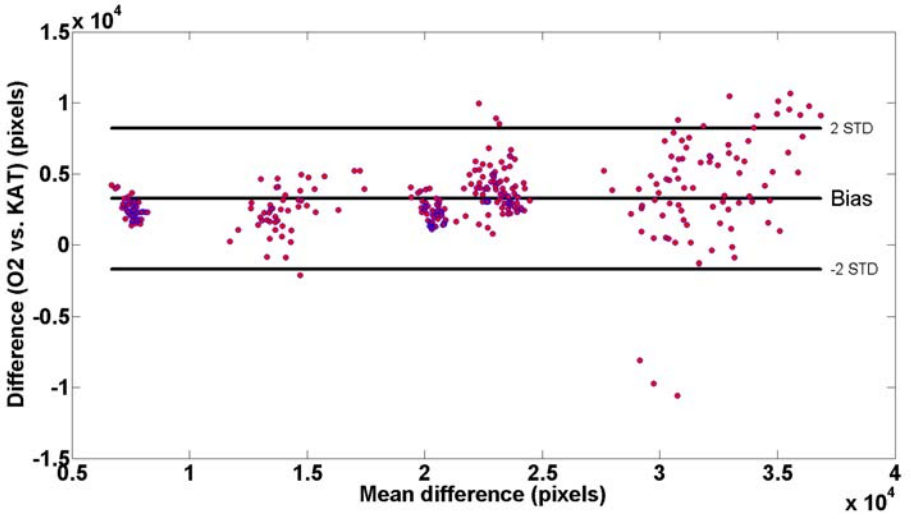

(b)

Figure 4.14: (a, b) Linear regression and (c,d) Bland-Altman plot for the comparison of the lumen areas segmented by Observer 2 (O2) with the areas segmented with the KAT method.

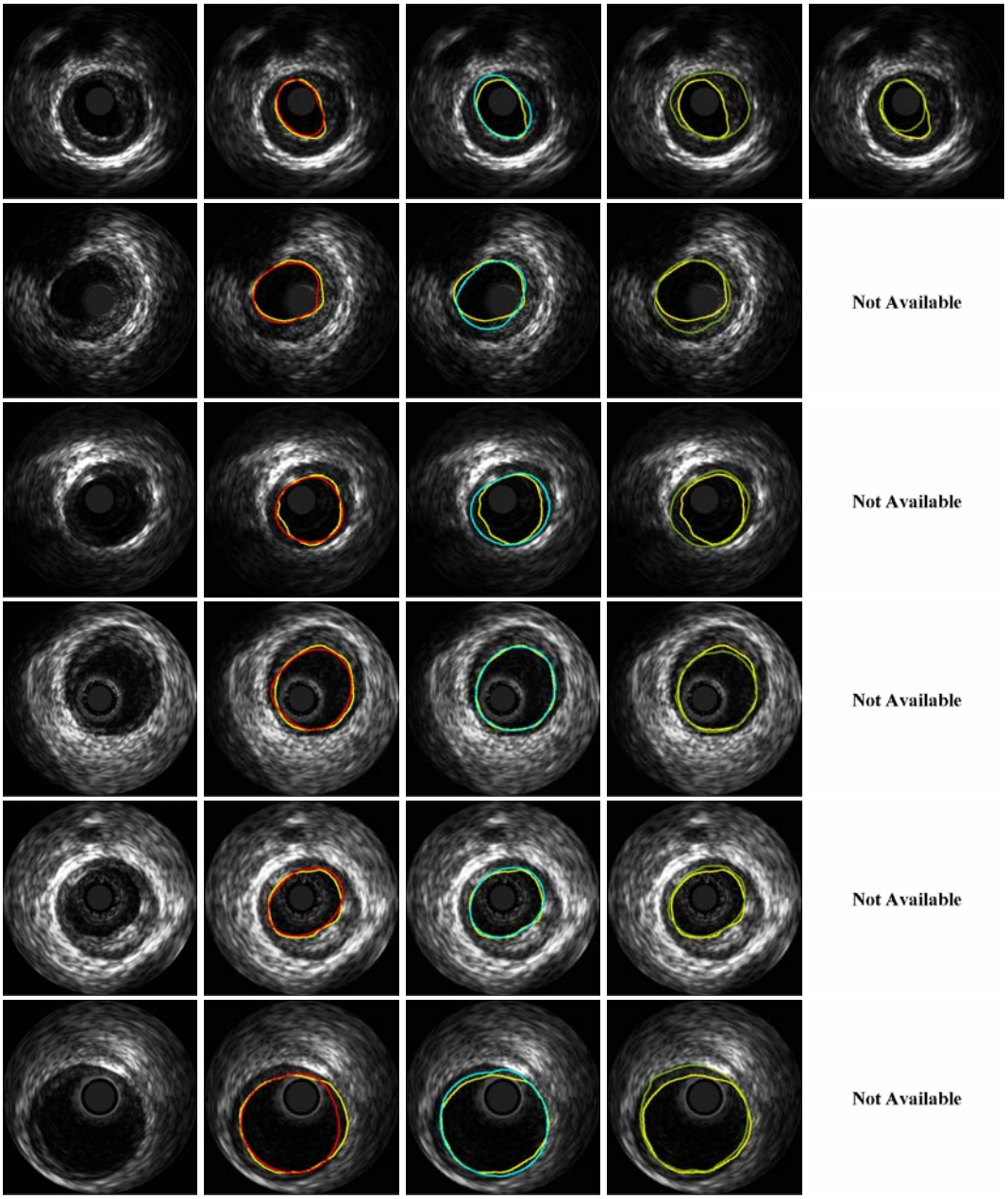

Figure 4.15: Examples of automatic segmentation results for 20 *MHz* sequences along with the segmentation of Observer 1 (yellow line). The images correspond to the original frame and the segmentation results with the IB, UNL, PAP, and KAT methods, from left to right, respectively.

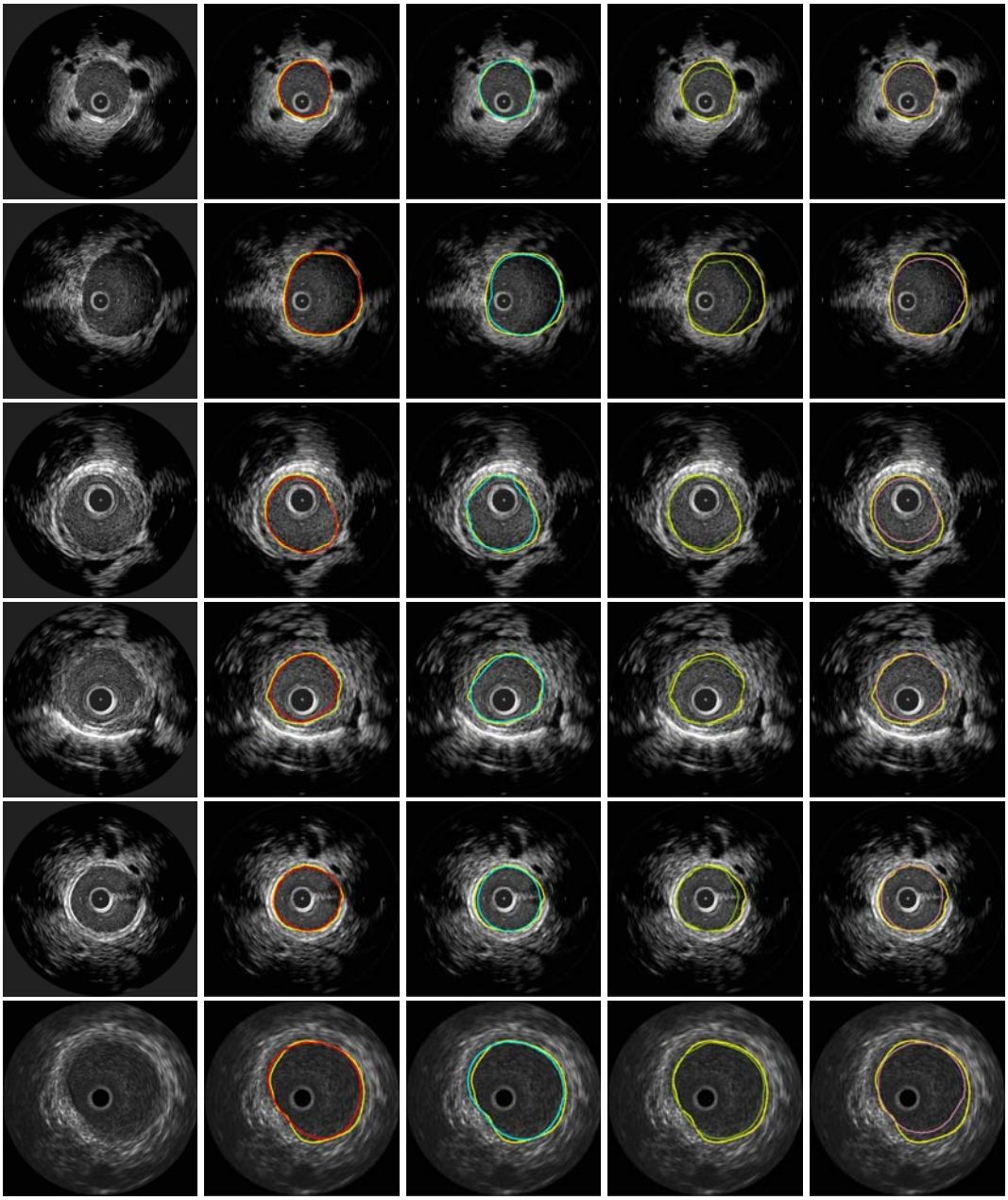

Figure 4.16: Examples of automatic segmentation results for 40 *MHz* sequences along with the segmentation by Observer 1 (yellow line). The images correspond to the original frame and the segmentation results with the IB, UNL, PAP, and KAT methods, from left to right, respectively.

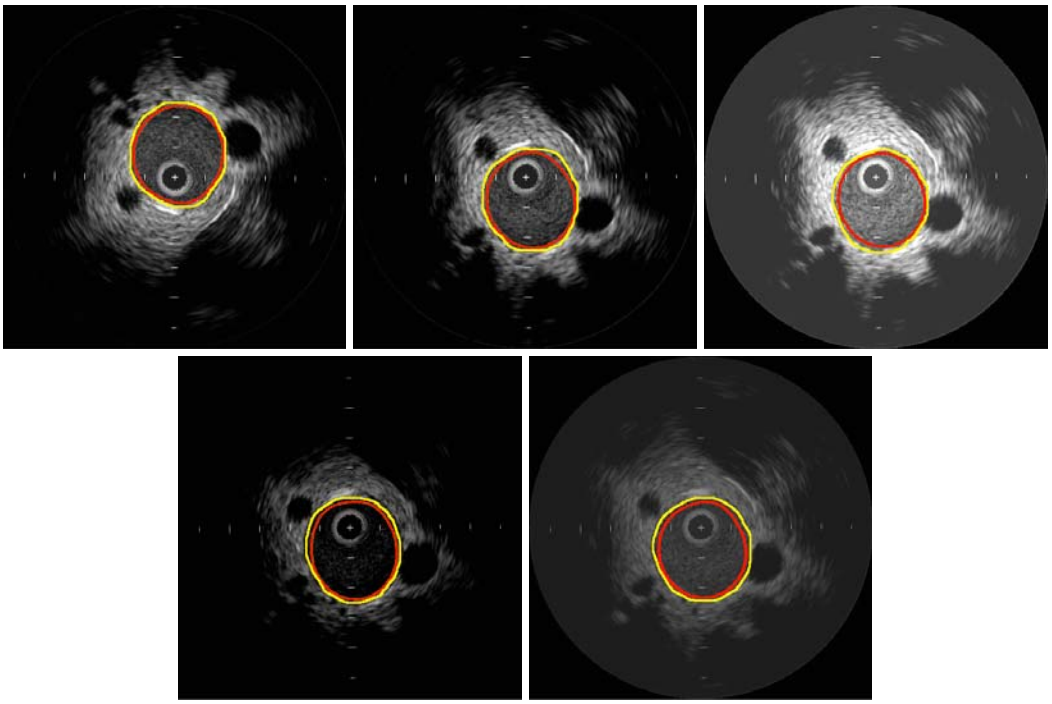

Figure 4.17: Segmentation results on the first frame of each modified subsequence.

4.3 RF-based approach results

The performance of the RFB method was evaluated using the RF data corresponding to 600 randomly selected frames from twelve 40 MHz pullback IVUS sequences obtained from rabbit aortas and different arteries of swine (Table 4.3) acquired with a Boston Scientific Galaxy II IVUS system with a 40 *MHz* catheter digitized with a sampling frequency of $f_s = 400$ *Mhz*.

We performed the segmentation of these data employing the B-mode reconstruction from the RF data with the IB method and with the raw RF data using the the RFB method, and we compared the results with the manual segmentations from an observer (O) on the selected frames. The evaluation consisted in comparing the areas of the lumen region

by computing, for each pair of segmentations, the Dice similarity coefficient (Fig. 4.18), the Jaccard index (Fig. 4.19), and by performing linear regression (Fig. 4.21), and Bland-Altman analysis (Fig. 4.22). Additionally, we computed the Hausdorff distance to measure the largest distance between the lumen contours (Fig. 4.20). The parameters employed for the segmentation of these frames are listed in Table 4.9.

Table 4.8: Information about IVUS-pullback sequences used for validation.

Sequence	Swine/Rabbit	IVUS system	Artery	Number of segmented frames
A	Swine	A	LAD	50
B	Swine	A	Carotid	50
C	Swine	A	RCA	50
D	Swine	A	Illiac	50
E	Swine	A	RCA	50
F	Rabbit	A	Aorta	50
G	Rabbit	A	Aorta	50
H	Rabbit	B	Aorta	50
I	Rabbit	B	Aorta	50
J	Rabbit	B	Aorta	50
K	Rabbit	B	Aorta	50
L	Rabbit	B	Aorta	50

Figure 4.23 depicts examples of the segmentation results. Note that the performance of our method is comparable with the performance of the expert observer.

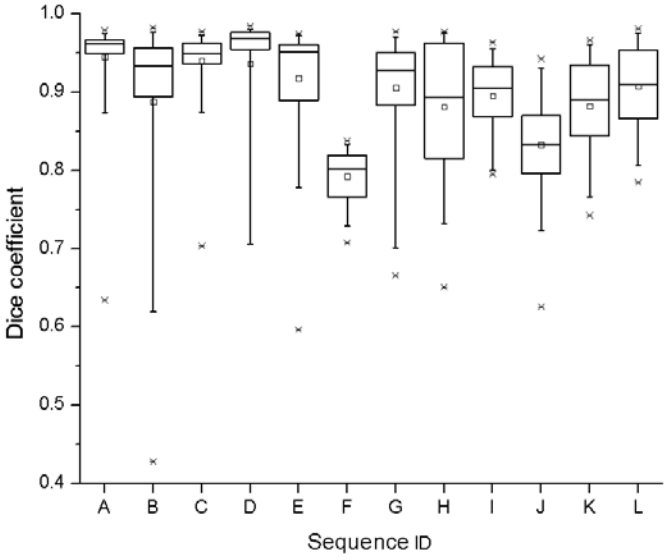

(a)

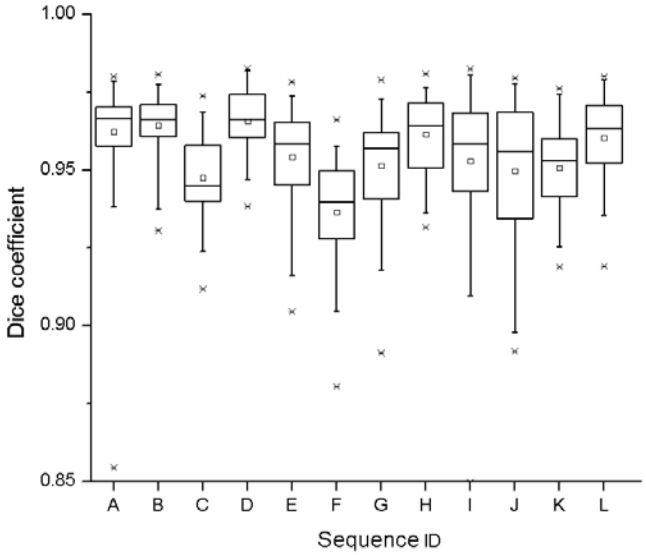

(b)

Figure 4.18: Dice coefficient results per each sequence for (a) the image-based and (b) the RF-based segmentation approaches.

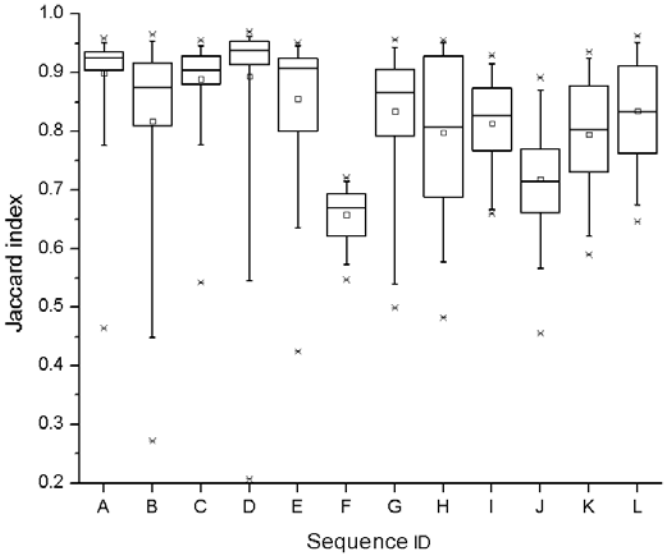

(a)

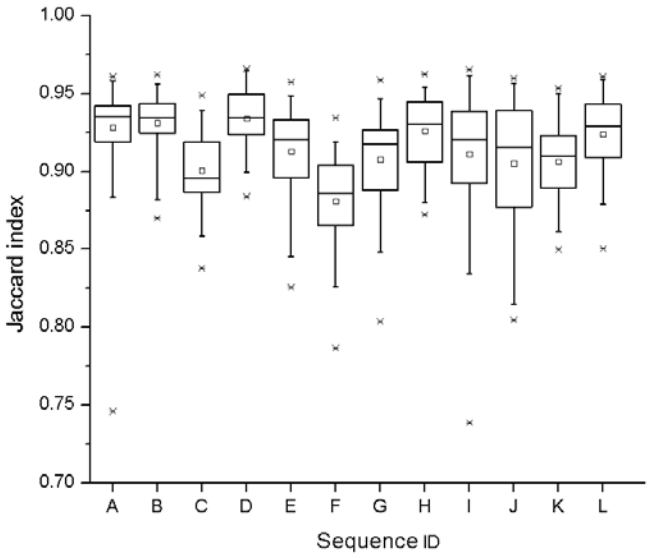

(b)

Figure 4.19: Jaccard index results per each sequence for (a) the B-mode-based and (b) the RF-based segmentation method .

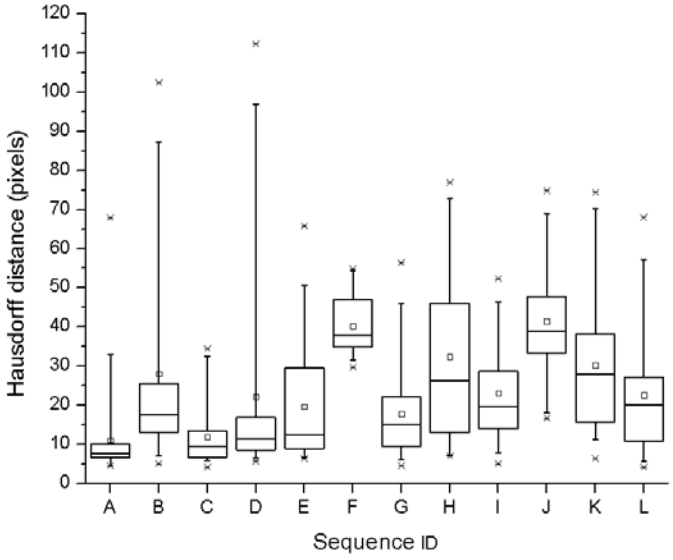

(a)

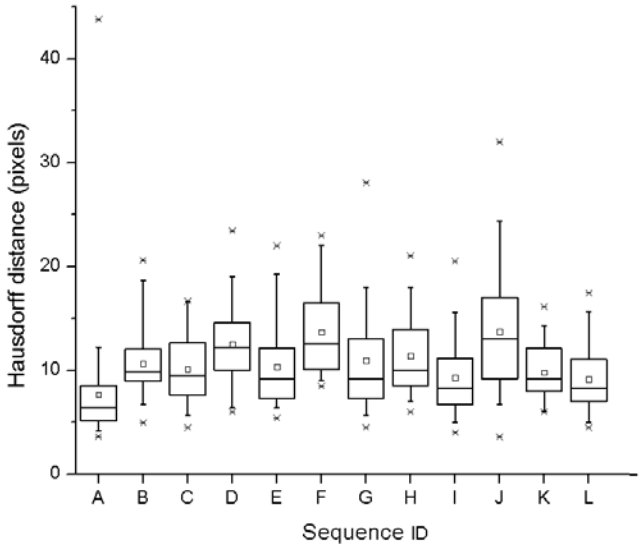

(b)

Figure 4.20: Hausdorff distance results per each sequence for (a) the image-based and (b) the RF-based segmentation method .

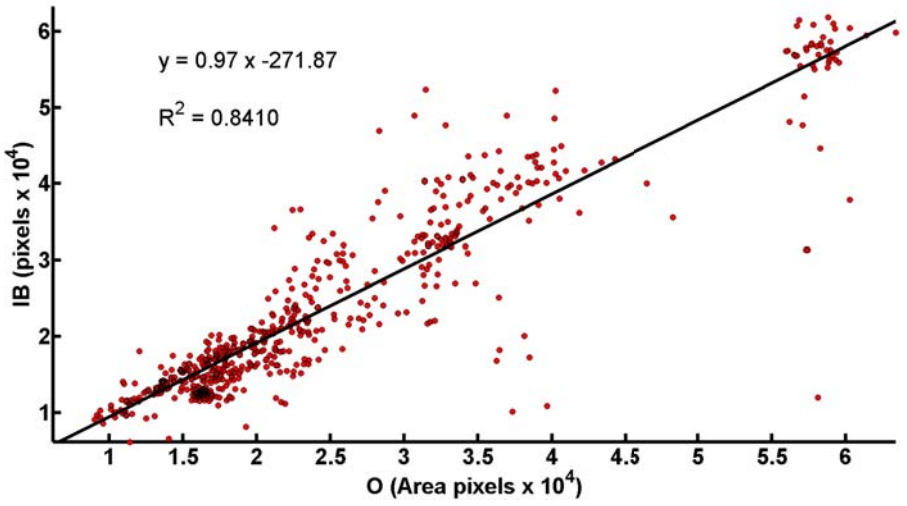

(a)

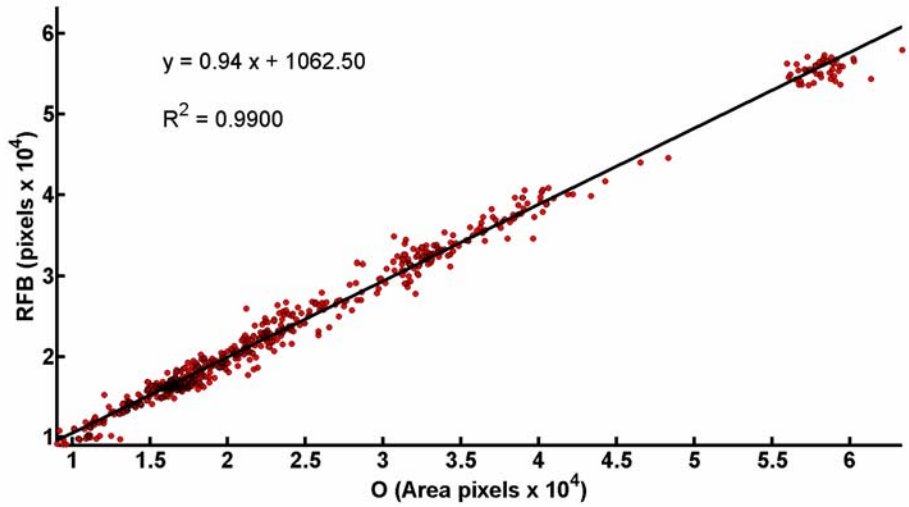

(b)

Figure 4.21: Linear regression for the comparison of lumen areas corresponding to the segmentation performed by the (a) the B-mode-based (IB) and (b) the RF-based (RFB) segmentation approaches, and the expert observer (O).

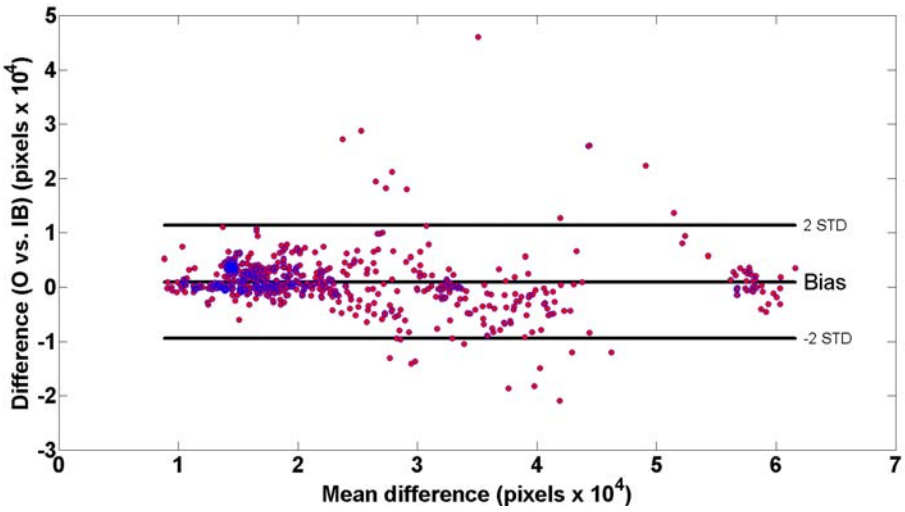

(a)

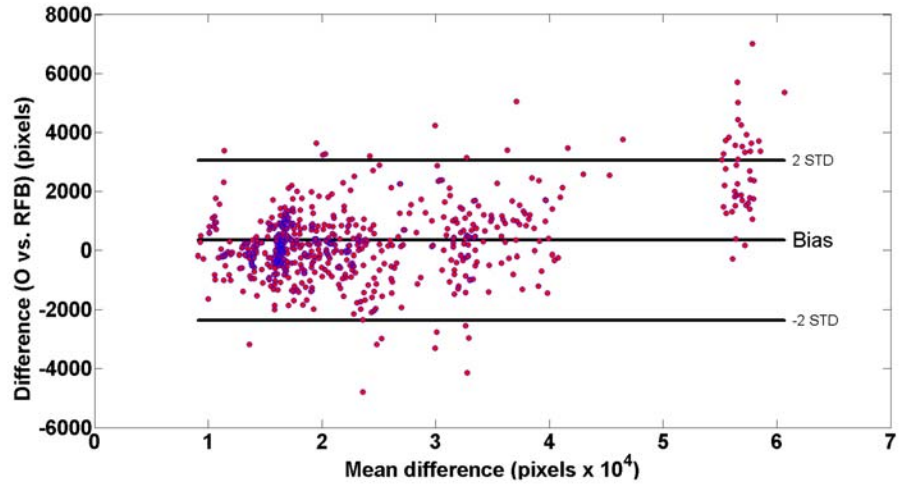

(b)

Figure 4.22: Bland-Altman plots for the comparison of lumen areas corresponding to the segmentation performed by the (a) the B-mode-based (IB) and (b) the RF-based (RFB) segmentation approaches, and the expert observer (O).

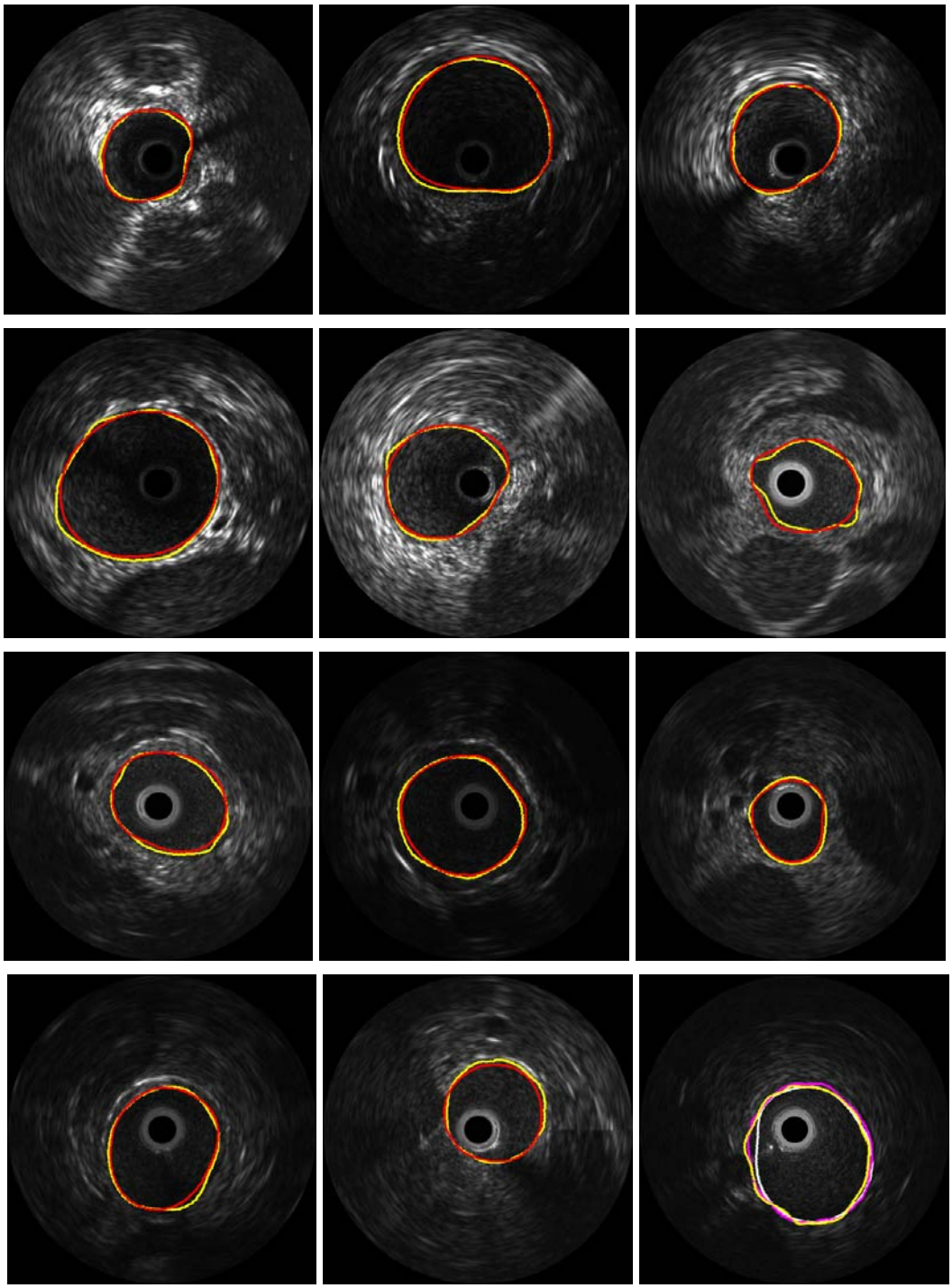

Figure 4.23: Examples of automatic segmentation results for the RF-based method. The yellow and red contours corresponds to the segmentations performed by the observer and the proposed method, respectively.

Table 4.9: Parameters used to generate the synthetic IVUS RF data.

Parameter	Value
c	1,540 *m/s*
μ	0.2 *dB/cm* at 1 *MHz*
V_v	3.37 $\times 10^{-3}$ mm^3
RBC volume	1.1945 $\times 10^{-7}$ *mm*
f	40 *MHz*
f_s	400 *MHz*
D	0.6 *mm*
ς	3.2468×10^{-8}
N_T	5
α	0.4
N_s	100
δ	2
p_s	0.05 *mm*

4.4 Results on IVUS images with artifacts

Shadows may appear on the IVUS images as dark regions representing of low acoustic impedance. In general these artifacts are generated by calcified plaque or a region of tissue with low acoustic impedance proximal to the vessel. Shadows represent a challenge for 20 *MHz* sequences because the low echogenicity of blood at this frequency generates gray level distributions on similar to those regions corresponding to shadows. However, since in our approach the lumen region is constrained by a curve it is not affected by these artifacts as long as there is a region with texture different from the lumen. Figures 4.24(a), 4.24(b) and 4.24(c) depicts a 20 *MHz* cases presenting shadows proximal to the vessel lumen. Note that, the IB method was able to provide an accurate segmentation because the existence of regions between the lumen and the shadow which constrain the evolution of the curve. Similarly, Fig. 4.24(d) depicts a 40 *MHz* case which presents a large shadow

proximal to the vessel lumen. Note that for this case, the IB method was able to provide an accurate segmentation because of the evident difference between the texture of the lumen and the shadow region. In general, shadow artifacts do not represent a challenge for 40 *MHz* sequences since the gray level intensities of the speckle present in blood are different from the homogeneously dark shadow regions.

Side branches are identified as the opening formed when the vessel being imaged bifurcates. This is visualized as an area with similar texture extending from the lumen in the near field towards the far field. Side branches represents a challenge for any segmentation method and in some cases even for observers because of the lack of an apparent change in the regions that indicates a change of interface. For these cases, the IB and RFB methods are not capable of providing a segmentation result similar with the segmentation of an observer. Figure 4.25 depicts an example of one case presenting a side branch with origin in the lumen. In this example, the curve that defines the lumen/wall interface of the proposed methods move through this region because the cost function is designed to keep inside the contour as much region corresponding to blood possible.

Similarly, for cases presenting regions of the vessel wall adjacent to the lumen contour with texture similar to the texture depicted in the lumen, the lack of an apparent change in the regions represents a challenge for automatic segmentation methods and observers. The IB method may produce inaccurate segmentation results in this cases. Figure 4.26 depicts an example of two 40 *MHz* frames in which the texture of the lumen is similar to the texture of a region of the wall. In these cases the IB method performed incorrectly.

Guidewire artifacts are produced by the reverberation of the guidewire when interacting with the ultrasound beam. Depending on the location of the guidewire with respect to

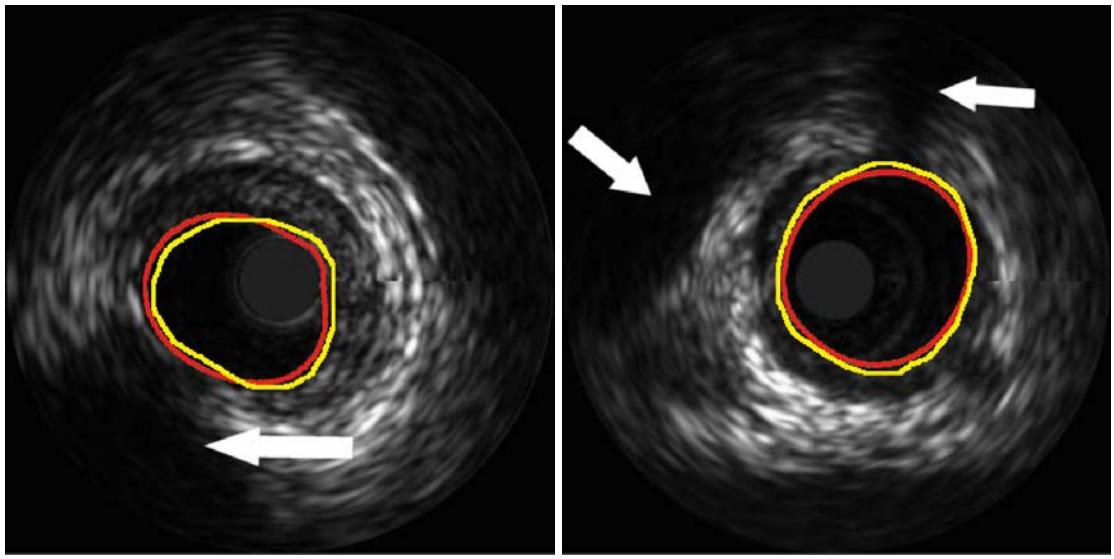

(a) (b)

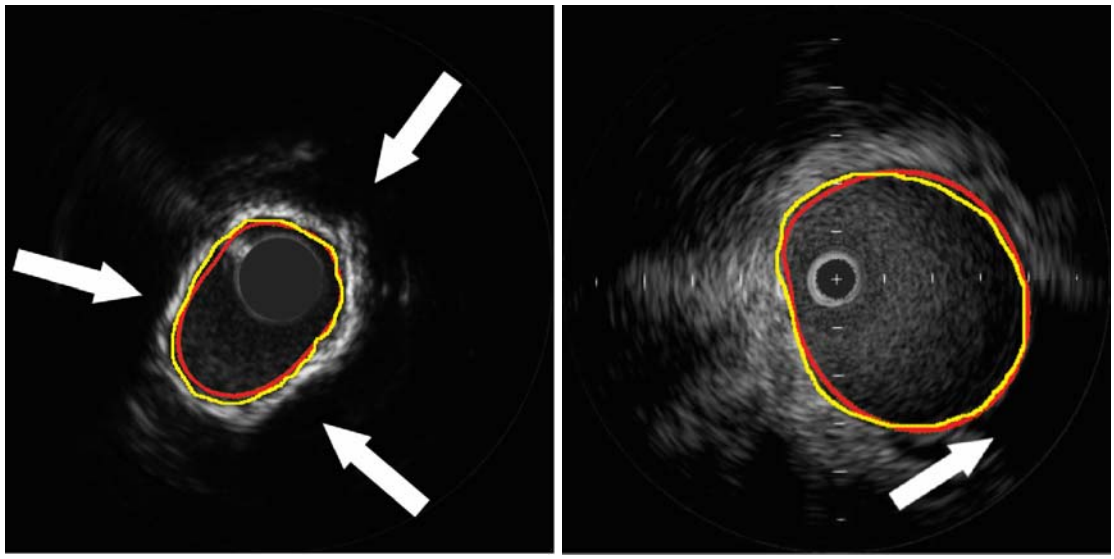

(c) (d)

Figure 4.24: Segmentation results examples of (a, b, c) 20 *MHz* and (c) 40 *MHz* IVUS images with shadow artifacts. The arrows indicate the regions corresponding to shadows. The Dice similarity score for each frame is: (a) 93.78%, (b) 94.72, (c) 94.32%, and (d) 95.64%.

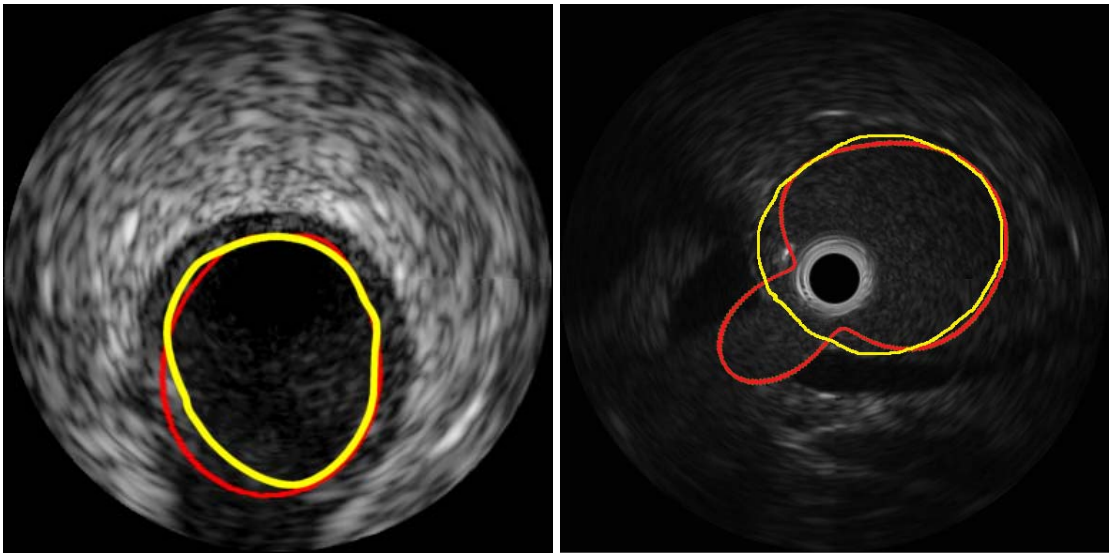

Figure 4.25: Segmentation results examples of (a) a 20 *MHz* and (b) a 40 *MHz* IVUS images depicting side branches. The Dice similarity score for each frame is: (a) 91.48% and (b) 86.66%.

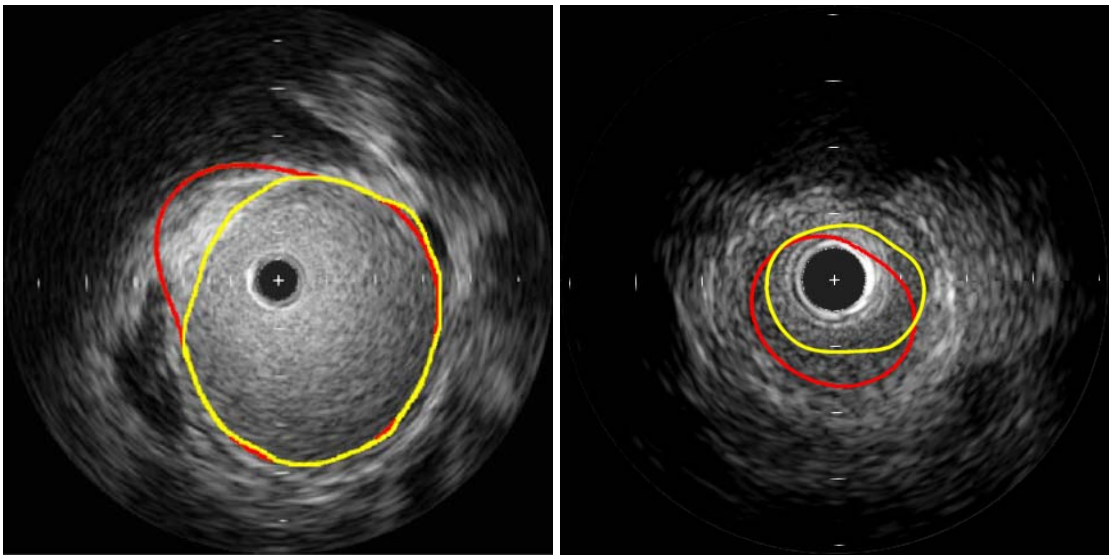

(a) (b)

Figure 4.26: Example of two frames of a 40 *MHz* sequence in which the texture of the lumen is similar to the texture of a region of the wall. The red line corresponds to the automatic segmentation, while the yellow line corresponds to the manual segmentation by the expert observer. The Dice similarity score for each frame is: (a) 88.72%, (b) 77.23%.

the ultrasound transducer, these artifacts appears in the IVUS images as bright thick spots or as series of partial rings followed by more distant shadowing behind the wire posing a challenge for the segmentation methods. Figure 4.27 depicts the segmentation results on images that present guidewire artifacts. Note that the IB method is capable to provide accurate segmentation results (Figs. 4.27(a), 4.27(b), and 4.27(c)). However, for some cases where there is a region of the lumen occupied by the artifact the proposed methods may perform incorrectly (Fig. 4.27(d)).

4.5 Discussion

The segmentation of IVUS images is an important yet difficult and time-consuming task necessary for the diagnosis and treatment of CAD. The proposed probabilistic segmentation method provides a semi-automatic tool to perform segmentation of the lumen/wall interface in IVUS data that can be used to help the physicians to reduce the time and effort required to analyze a sequence.

The IB method based on the analysis of the texture depicted in the region of the lumen and wall in the IVUS B-mode reconstructions. While the gray level intensity distribution of the IVUS images depends on the system and acquisition parameters, the proposed segmentation method implements an strategy for computing statistics of the gray level distributions of the sequence to segment allowing its use on IVUS sequences acquired with different IVUS systems and B-mode reconstruction parameters without the need of any parameter tuning. Note that the performance of the B-mode-based approach are closer and more consistent with the manual segmentation and represent a statistically significant improvement

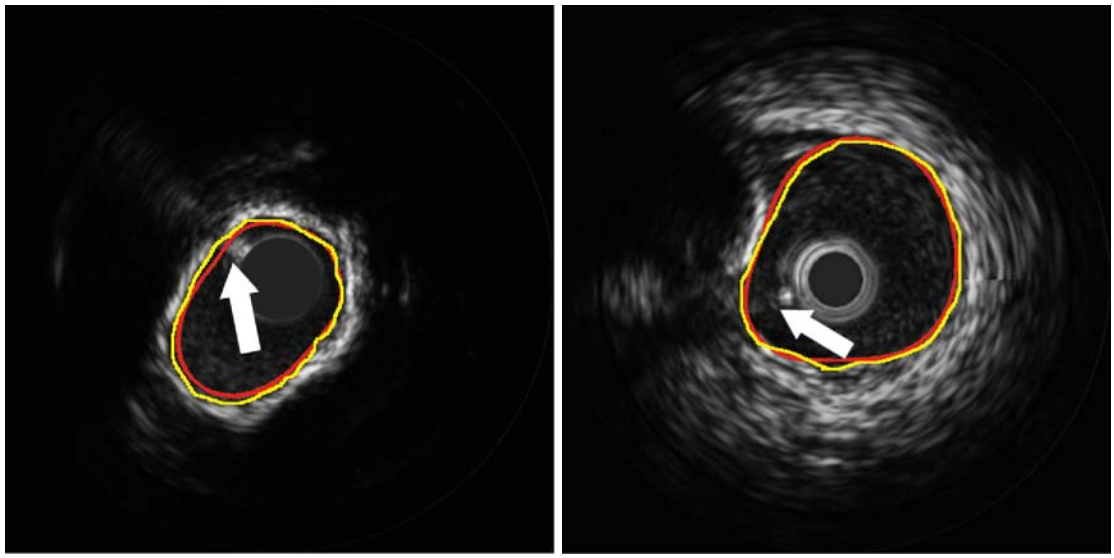

(a)

(b)

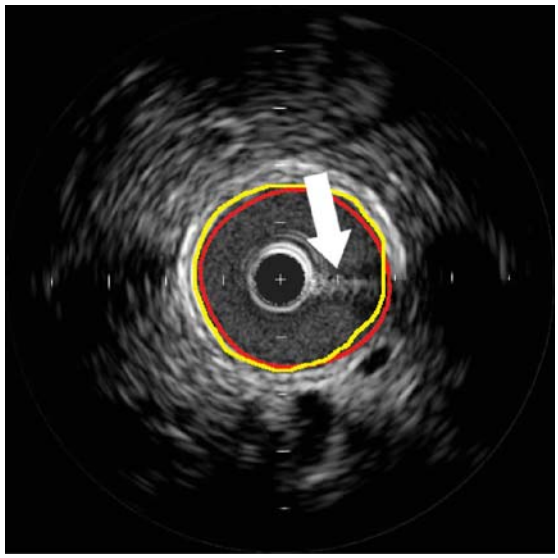

(c)

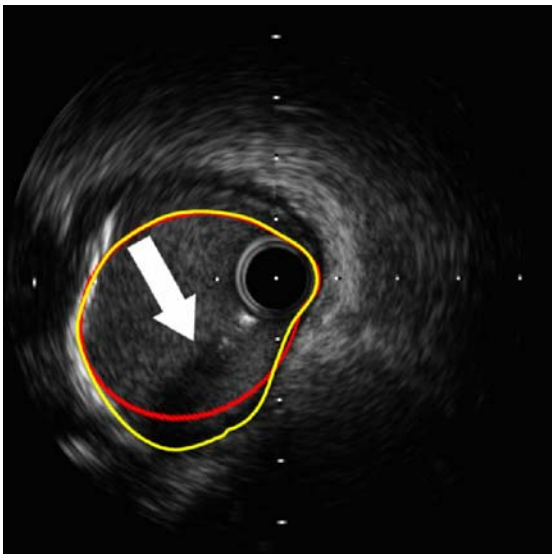

(d)

Figure 4.27: Segmentation results example of 40 *MHz* IVUS images with guidewire artifacts. The arrows indicate the guidewire artifact. The Dice similarity score for each frame is: (a) 94.32%, (b) 95.22%, (c) 93.38% and (c) 93.38% and (d) 89.21 %.

as compared with the other existing segmentation methods. The linear regression results indicate a better agreement between the luminal area detected by the proposed method with the luminal area defined by the observer when compared by the area detected by the other methods and higher coefficient of determination when compared with the other methods. From the Bland-Altman plots it can be observed that the proposed method performs with a low mean bias and less dispersion when compared with the other methods. While the average Dice similarity results of the proposed method and Unal's method are comparable, the proposed method presents a consistently smaller standard deviation which means that our method is more stable. In contrast to other methods, the proposed method does not require any supervised parameter tuning when changing between sequences with different IVUS frequencies or B-mode reconstruction parameters.

The RFB method is naturally robust with respect to the variability on the gray level intensity distribution of the IVUS images since it relies in the use of the un-processed RF signal. When comparing the segmentation results of the IB and RFB methods, it can be noted that the results of the RFB method exhibit less dispersion than the IB method. This is an indication that the DBC reconstruction provides a better way of characterizing the regions of interest in the IVUS data as compared with the B-mode reconstruction. Figure 4.28 depicts the comparison of the segmentation provided by an expert observer and the segmentation results employing both methods. Note that the RFB approach performs better since the likelihoods computed using the DBC reconstruction provide better estimates of the lumen and non-lumen regions.

The main novelty of the RFB method is the use of a physics-based approach for the lumen segmentation problem which represents a new paradigm for the analysis of the IVUS

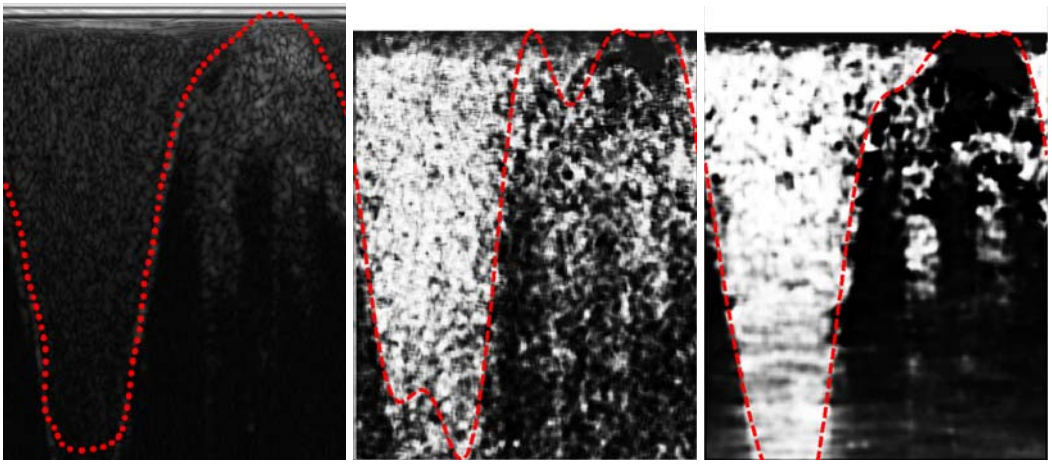

(a) (b) (c)

(d) (e) (f)

Figure 4.28: Examples of segmentation of lumen by an observer in (a) the polar and (d) Cartesian B-mode representations. Segmentation results using the IB method in (b) the luminal blood likelihood and (e) the Cartesian B-mode representation. Segmentation results using the RFB method in (c) the luminal blood likelihood and (f) the Cartesian B-mode representations. The red line indicates the lumen region.

data as compared with existing methods which makes use of arbitrary image or RF-based descriptors. The main advantage of our method when compared with B-mode-based segmentation methods is that the method based on this approach is not affected by the B-mode reconstruction parameters since it is based on the analysis of the RF signal instead of the gray level distributions of the B-mode reconstructions which are depending on the characteristics of the IVUS systems and the B-mode reconstruction parameters. Other possible application of the proposed DBC reconstruction method using the scattering model may include the characterization of plaques. While there may be a concern regarding the availability of the RF signal, note that recent IVUS systems available in the clinic are capable of providing the RF data.

The main two parameters required for the proposed segmentation methods are the number of Fourier coefficients for the lumen contour parameterization N_k, and the value λ of the sigmoid function that is used to determine the prior probabilities of each pixel to belong to lumen or non-lumen. The computation of the likelihoods for blood and non-blood in the B-mode approach does not require additional parameters to be defined. However the RF-based approach require the definition of the values for the size of partition p_s and the cardinality of the neighbor partitions δ used for the regularization of the DBC-reconstruction. The optimal values for these parameters were found experimentally and used to generate all the results presented in this dissertation. In practice, the user of the proposed segmentation method does not require to perform any modification of these parameters.

4.5.1 Limitations

The main limitation of the proposed segmentation method is the requirement of an expert user intervention in order to provide accurate annotations from the blood and non-blood regions in frames of the sequence to segment. Incorrect samples from blood and non-blood could result in an incorrect segmentation. Therefore, this initialization must be performed by an observer familiarized with the IVUS data. It is recommended to select at least 50% of the region corresponding to lumen and most of the region adjacent to the lumen corresponding to non-lumen.

Fully automatic approaches rely on the use of *a priori* information collected from training database consisting of high number of different IVUS cases. However, since the B-mode reconstruction relies in a highly subjective process, it is necessary that this training database is large enough to account for all the different appearances that an IVUS image can have. We could transform IB to fully automatic by performing the computation of the SVM models using blood and non-blood samples from a large training data set of different IVUS images. However, the main limitation of fully automatic methods is that they rely on the use of large training set databases for estimating the models of the gray intensity levels of the regions of interest. In order for these models to be robust, it would be necessary that this training database is large enough to account for all the different appearances that an IVUS image can have, including different visualization parameters. With respect to the RFB method, the initialization requirement is also necessary considering that the DBC reconstruction values for blood depends on factors such as the speed of blood flow that may be different depending on the size and location of the vessel that is analyzed, and the hematocrit concentration which may also vary from one subject to the other. For

this method to be fully automatic, it would also be necessary to employ a large data set of different IVUS cases.

The second limitation of the proposed methods relates with the inaccuracy of the segmentation result in the presence of artifacts in the IVUS images as discussed in Sec. 4.4. This limitation could be solved with the prior detection of the artifacts by the incorporation of further classes into the segmentation problem (e.g., ([71])).

4.5.2 Future work

An option to improve the results of the proposed segmentation method with respect to its limitations, is to adapt the computational methods in order to allow an interactive segmentation on which an automatically generated segmentation is provided to the user which is then allowed to perform modifications on the lumen curve. An extension of this solution is to implement an active learning approach on which the computational segmentation method is capable of learning the characteristics of the cases for which the segmentation was incorrect and then apply the correction performed by the user on the frames which presents the same characteristics.

The proposed probabilistic segmentation cost function of Eq. (3.5) is based on the use of the Kerridge's inaccuracy measure. However, the use of other similarity measurements (e.g., Euclidean distance and Q-dissimilarity) could also lead to correct segmentation results.

Future work includes improvements on the classification of the region of interest by the

exploration of additional features, adding robustness with respect to side branches and artifacts by the incorporation of additional classes (e.g., guidewire, shadows, plaque, and side branches), segmentation of the media/adventitia interface, the use of temporal information (i.e., 3D-approach), and the use of alternative models of the RF signal.

Chapter 5

Conclusion

This dissertation has presented a probabilistic framework for the segmentation of the lumen/wall interface from IVUS data consisting of two methods. The IB method incorporates texture information by using the prediction of an SVM classifier model. This step enable the segmentation of IVUS images from different frequencies (i.e., 20 and 40 MHz) without the need of adjusting any parameter, and it makes the proposed method robust to the problem of variability of IVUS image appearance. The RFB method represents a change of paradigm for the IVUS segmentation problem on which we consider the physics of the interaction of the ultrasound beam with the structures of the vessel as opposed to the traditional image-analysis based approach.

It is our hope that the proposed computational methods presented in this dissertation provide significant advancement towards the segmentation of IVUS data, and to the field of intravascular imaging in general.

Bibliography

[1] S. Balocco, C. Gatta, F. Ciompi, O. Pujol, X. Carrillo, J. Mauri, and P. Radeva. Combining growcut and temporal correlation for ivus lumen segmentation. In *Proc. 5^{th} Iberian Conference on Pattern Recognition and Image Analysis*, pages 556 – 563, Las Palmas de Gran Canaria, Spain, June 2011.

[2] J. Bland and D. Altman. Statistical methods for assessing agreement between two methods of clinical measurement. *Lancet*, 1(8476):307–310, Feb. 1986.

[3] E. Brusseau, C. L. de Korte, F. Mastik, J. Schaar, and A. F. W. van der Steen. Fully automatic luminal contour segmentation in intracoronary ultrasound imaging - a statistical approach. *IEEE Transactions on Medical Imaging*, 23(5):554–566, May 2004.

[4] C. J. C. Burges. A tutorial on support vector machines for pattern recognition. *Data Mining and Knowledge Discovery*, 2(2):121–167, 1998.

[5] A. P. Burke, A. Farb, G. T. Malcom, Y. H. Liang, J. Smialek, and R. Virmani. Coronary risk factors and plaque morphology in men with coronary disease who died suddenly. *The New England Journal of Medicine*, 336(18):1276–1282, 1997.

[6] M. Cardinal, J. Meunier, G. Soulez, R. L. Maurice, E. Therasse, and G. Cloutier. Intravascular ultrasound image segmentation: A three-dimensional fast-marching method based on gray level distributions. *IEEE Transactions on Medical Imaging*, 25(5):590–601, 2006.

[7] M. Cardinal, G. Soulez, J. C. Tardif, J. Meunier, and G. Cloutier. Fast-marching segmentation of three-dimensional intravascular ultrasound images: A pre-and post-intervention study. *Medical Physics*, 37(7):3633–3647, 2010.

[8] C.-C. Chang and C.-J. Lin. LIBSVM: A library for support vector machines. *ACM Transactions on Intelligent Systems and Technology*, 2(3):1–27, 2011.

[9] F. Ciompi, O. Pujol, E. Fernandez-Nofrerias, J. Mauri, and P. Radeva. ECOC random fields for lumen segmentation in radial artery IVUS sequences. In *Proc. 12^{th}*

International Conference on Medical Image Computing and Computer Assisted Intervention, pages 869–876, London, UK, Sep. 20 - 24 2009.

[10] P. Constantinides. Cause of thrombosis in human atherosclerotic arteries. *American Journal of Cardiology*, 66(16):37G–40G, 1990.

[11] M. Culjat, D. Goldenberg, P. Tewari, and R. Singh. A review of tissue substitutes for ultrasound imaging. *Ultrasound in Medicine and Biology*, 36(6):861–873, 2010.

[12] L. Dice. Measures of the amount of ecologic association between species. *Ecology*, 26(3):297–302, 1945.

[13] E. dos Santos Filho, M. Yoshizawa, A. Tanaka, and Y. Saijo. A study on intravascular ultrasound image processing. *Record of Electrical and Communication Engineering Conversazione, Tohoku University*, 74(2):30–33, 2006.

[14] R. Downe, A. Wahle, T. Kovarnik, H. Skalicka, J. Lopez, J. Horak, and M. Sonka. Segmentation of intravascular ultrasound images using graph search and a novel cost function. In *Proc. 2nd MICCAI Workshop on Computer Vision for Intravascular and Intracardiac Imaging*, pages 71–79, New York, NY, Sep. 10 2008.

[15] P. Elbischger, H. Bischof, G. Holzapfel, and P. Regitnig. Computer vision analysis of collagen fiber bundles in the adventitia of human blood vessels. *Studies in Health Technology and Informatics*, 113(1):97–129, 2005.

[16] M. R. Elliott and A. J. Thrush. Measurement of resolution in intravascular ultrasound images. *Physiol Meas*, 17(4):259–265, November 1996.

[17] M. E. Fabry, D. K. Kaul, C. Raventos, S. Baez, R. Rieder, and R. L. Nagel. Some aspects of the pathophysiology of homozygous Hb CC erythrocytes. *Journal of Clinical Investigation*, 67(5):1284 – 1291, 1981.

[18] I. Fontaine, M. Bertrand, and G. Cloutier. A system-based approach to modeling the ultrasound signal backscattered by red blood cells. *Biophysical Journal*, 77(5):2387–2399, 1999.

[19] C. K. Friedberg. *Diseases of the heart*, chapter Coronary arteriosclerosis, pages 336–352. WB Saunders, 1949.

[20] C. Haas, H. Ermert, S. Holt, P. Grewe, A. Machraoui, and J. Barmeyer. Segmentation of 3D intravascular ultrasonic images based on a random field model. *Ultrasound in Medicine and Biology*, 26(2):297–306, 2000.

[21] T. Hiro, C. Y. Leung, R. J. Russo, H. Karimi, A. R. Farvid, and J. M. Tobis. Variability of a three-layered appearance in intravascular ultrasound coronary images: A

comparison of morphometric measurements with four intravascular ultrasound systems. *American Journal of Cardiac Imaging*, 10(4):219–227, 1996.

[22] C. Hsu, C. Chang, and C. Lin. A practical guide to support vector classification. Technical report, National Taiwan University, July 2003.

[23] O. Jesorsky, K. J. Kirchberg, , and R. W. Frischholz. Robust face detection using the hausdorff distance. In *Proc. Third International Conference on Audio- and Video-based Biometric Person Authentication LNCS-2091*, pages 90–95, Halmstad, Sweden, 6-8 June 2001.

[24] A. Katouzian, E. D. Angelini, B. Sturm, and A. F. Laine. Brushlet-driven segmentation framework for automatic detection of lumen borders in ivus images with comparison study. In *Proc. International Symposium on Biomedical Imaging*, pages 242 –245, Barcelona, Spain., May 2012.

[25] A. Katouzian, B. Baseri, E. Konofagou, and A. Laine. Automatic detection of blood versus non-blood regions on intravascular ultrasound (IVUS) images using wavelet packet signatures. In *Proc. SPIE Medical Imaging: Ultrasonic Imaging and Signal Processing*, pages 1 – 8, San Diego, CA, February 2008.

[26] A. Katouzian, B. Baseri, E. E. Konofagou, and A. F. Laine. An alternative approach to spectrum-based atherosclerotic plaque characterization techniques using intravascular ultrasound (IVUS) backscattered signals. In *Proc. 2^{nd} MICCAI Workshop on Computer Vision for Intravascular and Intracardiac Imaging*, New York, NY, 2008.

[27] M. Kawasaki, H. Takatsu, T. Noda, Y. Ito, A. Kunishima, M. Arai, K. Nishigaki, G. Takemura, N. Morita, S. Minatoguchi, and H. Fujiwara. Noninvasive quantitative tissue characterization and two-dimensional color-coded map of human atherosclerotic lesions using ultrasound integrated backscatter: Comparison between histology and integrated backscatter images. *Journal of the American College of Cardiology*, 38(2):486–492, Aug. 2001.

[28] M. Kawasaki, H. Takatsu, T. Noda, K. Sano, Y. Ito, K. Hayakawa, K. Tsuchiya, M. Arai, K. Nishigaki, G. Takemura, S. Minatoguchi, T. Fujiwara, and H. Fujiwara. In vivo quantitative tissue characterization of human coronary arterial plaques by use of integrated backscatter intravascular ultrasound and comparison with angioscopic findings. *Circulation*, 105:2487–2492, 2002.

[29] D. F. Kerridge. Inaccuracy and inference. *Journal of the Royal Statistical Society*, 23(1):184 – 194, 1961.

[30] J. D. Klingensmith, R. Shekhar, and D. G. Vince. Evaluation of three-dimensional

segmentation algorithms for the identification of luminal and medial-adventitial borders in intravascular ultrasound images. *IEEE Transactions on Medical Imaging*, 19(10):996–1011, 2000.

[31] L. Koch and T. Roth. *Technical aspects of intravascular ultrasound*, chapter 3, pages 17–30. Martin Dunitz, United Kingdom, 1998.

[32] G. Kovalski, R. Beyar, R. Shofti, and H. Azhari. Three-dimensional automatic quantitative analysis of intravascular ultrasound images. *Ultrasound in Medicine and Biology*, 26(4):527–537, 2000.

[33] K. I. Laws. Rapid texture identification. In *Proc. SPIE Conference on Image Processing for Missile Guidance*, pages 376–380, San Diego, CA, July 1980.

[34] D. C. Lee and T. Schenk. Image segmentation from texture measurement. *ISPRS Journal of Photogrammetry and Remote Sensing*, XXIX, Part B3, Commission III:195–199, August 1992.

[35] B. Lim, P. Bascom, and R. Cobbold. Particle and voxel approaches for simulating ultrasound backscattering from tissue. *Ultrasound in Medicine and Biology*, 22(9):1237–1247, 1996.

[36] H. Lin, L. Zhang, C. Liu, X. Xu, M. Tang, H. Lv, C. Li, H. Sun, M. Zhang, J. Hong, and Y. Zhang. Haemin-enhanced expression of haem oxygenase-1 stabilizes erythrocyte-induced vulnerable atherosclerotic plaques. *British Journal of Pharmacology*, 160(6):1484–1495, 2010.

[37] Z. Luo, Y. Wang, and W. Wang. Estimating coronary artery lumen area with optimization-based contour detection. *IEEE Transactions on Medical Imaging*, 22(4):564 – 566, Apr. 2003.

[38] A. Maton. *Human biology and health*. Prentice Hall, 1993.

[39] D. S. Meier, R. M. Cothren, D. G. Vince, and J. F. Cornhill. Automated morphometry of coronary arteries with digital image analysis of intravascular ultrasound. *American Heart Journal*, 133(6):681–690, Jun. 1997.

[40] E. Mendizabal-Ruiz and I. A. Kakadiaris. One-class acoustic characterization applied to contrast agent detection in IVUS. In *Proc. International Workshop on Computer Vision for Intravascular and Intracardiac Imaging*, New York, NY, Sep. 10 2008.

[41] E. G. Mendizabal-Ruiz, M. Rivera, and I. A. Kakadiaris. A probabilistic segmentation method for the identification of luminal borders in intravascular ultrasound

images. In *Proc. IEEE Computer Society Conference on Computer Vision and Pattern Recognition*, pages 1–8, Anchorage, AK, Jun. 24-26 2008.

[42] G. Mintz, S. Nissen, W. Anderson, S. Bailey, R. Erbel, P. Fitzgerald, F. Pinto, K. Rosenfield, R. Siegel, E. Tuzcu, and P. Yock. American College of Cardiology clinical expert consensus document on standards for acquisition, measurement and reporting of intravascular ultrasound studies (IVUS). *Journal of the American College of Cardiology*, 37(5):1478–1492, 2001.

[43] G. S. Mintz, S. E. Nissen, W. D. Anderson, S. R. Bailey, R. Erbel, P. J. Fitzgerald, F. J. Pinto, K. Rosenfield, R. J. Siegel, E. M. Tuzcu, P. G. Yock, R. A. O'Rourke, J. Abrams, E. R. Bates, B. R. Brodie, P. S. Douglas, G. Gregoratos, M. A. Hlatky, J. S. Hochman, S. Kaul, C. M. Tracy, D. D. Waters, and J. Winters, William L. American college of cardiology clinical expert consensus document on standards for acquisition, measurement and reporting of intravascular ultrasound studies (ivus): A report of the american college of cardiology task force on clinical expert consensus do. *Journal of the American College of Cardiology*, 37(5):1478–1492, 2001.

[44] A. K. Mitra, A. S. Dhume, and D. K. Agrawal. "Vulnerable plaques" - ticking of the time bomb. *Canadian Journal of Physiology and Pharmacology*, 82(10):860–871, 2004.

[45] A. Mojsilovic, M. Popovic, N. Amodaj, R. Babic, and M. Ostojic. Automatic segmentation of intravascular ultrasound images: A texture-based approach. *Annals of Biomedical Engineering*, 25(6):1059–1071, Nov. 1997.

[46] M. Moraes and S. Furuie. Automatic coronary wall segmentation in intravascular ultrasound images using binary morphological reconstruction. *Ultrasound in Medicine and Biology*, 37(9):1486–1499, 2011.

[47] P. M. Morse and K. U. Ingard. *The scattering of sound*, pages 400 – 446. McGraw Hill, New York, 1968.

[48] M. Naghavi, E. Falk, H. Hecht, M. Jamieson, S. Kaul, D. Berman, Z. Fayad, M. Budoff, J. Rumberger, T. Naqvi, L. Shaw, O. Faergeman, J. Cohn, R. Bahr, W. Koenig, J. Demirovic, D. Arking, V. Herrera, J. Badimon, J. Goldstein, Y. Rudy, J. Airaksinen, R. Schwartz, W. Riley, R. Mendes, P. Douglas, and P. Shah. From vulnerable plaque to vulnerable patient-Part III: Executive summary of the Screening for Heart Attack Prevention and Education (SHAPE) Task Force report. *American Journal of Cardiology*, 98(2A):2H–15H, 2006.

[49] M. Naghavi, P. Libby, E. Falk, S. Casscells, S. Litovsky, J. Rumberger, J. Badimon, C. Stefanadis, P. Moreno, G. Pasterkamp, Z. Fayad, P. Stone, S. Waxman, P. Raggi, M. Madjid, A. Zarrabi, A. Burke, C. Yuan, P. Fitzgerald, D. Siscovick, C. de Korte,

M. Aikawa, K. Airaksinen, G. Assmann, C. Becker, J. Chesebro, A. Farb, Z. Galis, C. Jackson, I. Jang, W. Koenig, R. Lodder, K. March, J. Demirovic, M. Navab, S. Priori, M. Rekhter, R. Bahr, S. Grundy, R. Mehran, A. Colombo, E. Boerwinkle, C. Ballantyne, J. Insull, W., R. Schwartz, R. Vogel, P. Serruys, G. Hansson, D. Faxon, S. Kaul, H. Drexler, P. Greenland, J. Muller, R. Virmani, P. Ridker, D. Zipes, P. Shah, and J. Willerson. From vulnerable plaque to vulnerable patient: A call for new definitions and risk assessment strategies: Part I. *Circulation*, 108(14):1664–1672, 2003.

[50] M. Naghavi, P. Libby, E. Falk, S. Casscells, S. Litovsky, J. Rumberger, J. Badimon, C. Stefanadis, P. Moreno, G. Pasterkamp, Z. Fayad, P. Stone, S. Waxman, P. Raggi, M. Madjid, A. Zarrabi, A. Burke, C. Yuan, P. Fitzgerald, D. Siscovick, C. de Korte, M. Aikawa, K. Airaksinen, G. Assmann, C. Becker, J. Chesebro, A. Farb, Z. Galis, C. Jackson, I. Jang, W. Koenig, R. Lodder, K. March, J. Demirovic, M. Navab, S. Priori, M. Rekhter, R. Bahr, S. Grundy, R. Mehran, A. Colombo, E. Boerwinkle, C. Ballantyne, W. Insull, R. Schwartz, R. Vogel, P. Serruys, G. Hansson, D. Faxon, S. Kaul, H. Drexler, P. Greenland, J. Muller, R. Virmani, P. Ridker, D. Zipes, P. Shah, and J. Willerson. From vulnerable plaque to vulnerable patient: A call for new definitions and risk assessment strategies: Part II. *Circulation*, 108(15):1772–1778, 2003.

[51] A. Nair, B. Kuban, E. Tuzcu, P. Schoenhagen, S. Nissen, and D. Vince. Coronary plaque classification with intravascular ultrasound radiofrequency data analysis. *Circulation*, 106(17):2200–2206, 2002.

[52] A. Nair, M. Margolis, B. Kuban, and D. Vince. Automated coronary plaque characterisation with intravascular ultrasound backscatter: Ex vivo validation. *Eurointervention*, 3(1):113–120, 2007.

[53] S. E. Nissen and P. Yock. Intravascular ultrasound: Novel pathophysiological insights and current clinical applications. *Circulation*, 103(4):604–616, January 2001.

[54] J. Nocedal and S. J. Wright. *Numerical Optimization*. Springer, 1999.

[55] S. M. O'Malley, M. Naghavi, and I. A. Kakadiaris. One-class acoustic characterization applied to blood detection in IVUS. In *Proc. 10^{th} International Conference on Medical Image Computing and Computer Assisted Intervention*, pages 202–209, Brisbane, Australia, Oct. 29 - Nov. 2 2007.

[56] M. Papadogiorgaki, V. Mezaris, Y. S. Chatzizisis, G. D. Giannoglou, and I. Kompatsiaris. Image analysis techniques for automated IVUS contour detection. *Ultrasound in Medicine and Biology*, 34(9):1482–1498, Sep. 2008.

[57] M. E. Plissiti, D. I. Fotiadis, L. K. Michalis, and G. E. Bozios. An automated method for lumen and media-adventitia border detection in a sequence of IVUS frames. *IEEE Transactions on Information Technology in Biomedicine*, 8(2):131–141, Jun. 2004.

[58] M. Ramirez, P. Radeva, J. Mauri, and O. Pujol. Simulation model of intravascular ultrasound images. In *Proc. 7^{th} International Conference on Medical Image Computing and Computer-Assisted Intervention*, pages 200–207, Saint-Malo, France, Sep. 26 - 30 2004.

[59] J. W. S. Rayleigh. *Vibrations of solid bodies*, page 415431. Dover Publications, New York, 1945.

[60] M. Rivera and O. Dalmau. Variational viewpoint of the quadratic markov measure field models: theory and algorithms. *IEEE Transactions on Image Processing*, 21(3):1246 – 1257, 2012.

[61] V. L. Roger, A. S. Go, D. M. Lloyd-Jones, E. J.Benjamin, J. D. Berry, W. B. Borden, D. M. Bravata, S. Dai, E. S. Ford, C. S. Fox, H. J. Fullerton, C. Gillespie, S. M. Hailpern, J. A. Heit, V. J. Howard, B. M. Kissela, S. J. Kittner, D. T. Lackland, J. H. Lichtman, L. D. Lisabeth, D. M. Makuc, G. M. Marcus, A. Marelli, D. B. Matchar, C. S. Moy, D. Mozaffarian, M. E. Mussolino, G. Nichol, N. P. Paynter, E. Z. Soliman, P. D. Sorlie, N. Sotoodehnia, T. N. Turan, S. S. Virani, N. D. Wong, D. Woo, and M. B. Turner. Heart disease and stroke statistics–2012 update : A report from the american heart association. *Circulation*, 125:e2–e220, December 2012.

[62] A. Roodaki, A. Taki, S. K. Setarehdan, and N. Navab. Modified wavelet transform features for characterizing different plaque types in IVUS images; a feasibility study. In *Proc. 9^{th} International Conference on Signal Processing*, pages 789–792, Beijing, China, Oct. 26 - 29 2008.

[63] R. Ross. The pathogenesis of atherosclerosis: A perspective for the 1990s. *Nature*, 362:801–809, 1993.

[64] E. Sanidas, M. Vavuranakis, T. Papaioannou, I. Kakadiaris, S. Carlier, G. Syros, G. Dangas, and C. Stefanadis. Study of atheromatous plaque using intravascular ultrasound. *Hellenic Journal of Cardiology*, 49(6):415–421, 2008.

[65] K. Shung and G. Thieme. *Ultrasonic scattering in biological tissues*. CRC Press, 1993.

[66] K. K. Shung, M. B. Smith, and B. Tsui. *Principles of medical imaging*. Academic Press, 1992.

[67] M. Sonka, X. Zhang, M. Siebes, M. S. Bissing, S. C. DeJong, S. M. Collins, and R. C. McKay. Segmentation of intravascular ultrasound images: A knowledge-based approach. *IEEE Transactions on Medical Imaging*, 14(4):719–732, Dec. 1995.

[68] A. Taki, Z. Najafi, A. Roodaki, S. K. Setarehdan, R. A. Zoroofi, A. Konig, and N. Navab. Automatic segmentation of calcified plaques and vessel borders in IVUS

images. *International Journal of Computer Assisted Radiology and Surgery*, 3(3-4):347 – 354, 2008.

[69] J. Thijssen and B. Oosterveld. Perfomance of echographic equipment and potentials for tissue characterization. *Mathematics and Computer Science in Medical Imaging*, F39:455–468, 1998.

[70] N. M. Tole. *Image characteristics in clinical ultrasound*, chapter 8, pages 69–85. World Health Organization, 2005.

[71] G. Unal, S. Bucher, S. Carlier, G. Slabaugh, T. Fang, and K. Tanaka. Shape-driven segmentation of the arterial wall in intravascular ultrasound images. *IEEE Transactions on Information Technology in Biomedicine*, 12(3):335–347, May 2008.

[72] W. Verhoef, M. Cloostermans, and J. Thijssen. The impulse response of a focused source with an arbitrary axisymmetric surface velocity distribution. *Journal of the Acoustical Society of America*, 75:1716 – 1721, 1984.

[73] R. Virmani, A. P. Burke, A. Farb, and F. D. Kolodgie. Pathology of the vulnerable plaque. *Journal of the American College of Cardiology*, 47(8C):13–18, 2006.

[74] R. Virmani, F. D. Kolodgie, A. P. Burke, A. V. Finn, H. K. Gold, T. N. Tulenko, S. P. Wrenn, and J. Narula. Atherosclerotic plaque progression and vulnerability to rupture: Angiogenesis as a source of intraplaque hemorrhage. *Arteriosclerosis, Thrombosis, and Vascular Biology*, 25(10):2054–2061, 2005.

[75] C. von Birgelen, C. D. Mario, W. Li, J. C. H. Schuurbiers, C. J. Slager, P. J. de Feyter, J. R. T. C. Roelandt, and P. W. Serruys. Morphometric analysis in three-dimensional intracoronary ultrasound: An in vitro and in vivo study using a novel system for the contour detection of lumen and plaque. *American Heart Journal*, 132(3):516–527, 1996.

[76] M. Wennogle and W. Hoff. Three dimensional segmentation of intravascular ultrasound data. In *Proc. 6^{th} International Conference on Image Analysis and Recognitio*, volume 5627, pages 772–781, Toronto, Canada, July 2009.

[77] T. Wu, C. Lin, and R. Weng. Probability estimates for multi-class classification by pairwise coupling. *Journal of Machine Learning Research*, 5:975–1005, 2004.

[78] X. Zhang, C. R. McKay, and M. Sonka. Tissue characterization in intravascular ultrasound images. *IEEE Transactions on Medical Imaging*, 17(6):889–899, Dec. 1998.

[79] X. Zhu, P. Zhangc, J. Shaoa, Y. Chenga, Y. Zhangc, and J. Bai. A snake-based

method for segmentation of intravascular ultrasound images and its in vivo validation. *Ultrasonics*, 51(2):181–189, 2011.